The Study on Mechanical Behaviors and Metallurgical Characteristics of Welded Part in the Lightweight alloy by Friction Stir Welding

Heung-Ju Kim

February 2006

Ph.D. Thesis

Department of Producing and Processing Engineering
Graduate School of Chosun University

The Study on Mechanical Behaviors and Metallurgical Characteristics of Welded Part in the Lightweight alloy by Friction Stir Welding

경량합금의 마찰교반접합(FSW)에 의한 접합부의 역학적 거동 및 금속학적 특성 에 관한 연구

Heung-Ju Kim

February 2006

Ph.D. Thesis

Department of Producing and Processing Engineering
Graduate School of Chosun University

The Study on Mechanical Behaviors and Metallurgical Characteristics of Welded Part in the Lightweight alloy by Friction Stir Welding

Heung-Ju Kim

February 2006

Ph.D. Thesis

Department of Producing and Processing Engineering
Graduate School of Chosun University

Thesis, was written by Heung-Ju Kim, is approved by faculties.

RIST Facility & Automation Research Center
San 32 Hyoja-dong, Nam-gu, Pohang
Republic of Korea

Dr. Young-Gak Kweon _____

Department of Naval Architecture at Chosun University
375 Seosuk-dong, Dong-gu, Gwang-ju
Republic of Korea

Ph.D. Han-Sur Bang _____

RIST Welding Research Center
San 32 Hyoja-dong, Nam-gu, Pohang
Republic of Korea

Dr. Woong-Seong Chang _____

KITECH Advanced Welding & Joining Technology Team
994-32 Dongchun-dong, Yeonsoo-gu, Inchon
Republic of Korea

Dr. Jeong-Han Kim _____

Department of Naval Architecture at Chosun University
375 Seosuk-dong, Dong-gu, Gwang-ju
Republic of Korea

Ph.D. Duck-Young Yoon _____

CONTENTS

ABSTRACT……4

List of Figure…… 7

List of Table……..10

Chapter 1 Introduction……...13

1.1 Background to the Research.....……. ……...13
1.2 Scopes and Objective……..……..17
1.3 Literature Review.....…...19
1.4 Thesis Organization ……..……...…23

Chapter 2 Heat Conduction Theory for Friction Stir Welding.....…...24

2.1 Introduction ……..……24
2.2 Theoretical basic for Analysis……..……25
2.2.1 2-D Heat Conduction Theory of Friction Stir Welding ……..……..25
2.2.2 3-D Heat Conduction Theory of Friction Stir Welding ……..……..28

Chapter 3 Thermal Elasto-plastic Theory of Friction Stir Welding……....29

3.1 Heat Conduction Analysis……..…..…….29
3.2 Thermal Elasto-plastic Analysis……..……33
3.2.1 Basic Theory for Thermal stress Analysis…..…….……..33
3.2.2 Elasto-plastic Material Behaviour……..……35

Chapter 4 Numerical Analysis on Friction Stir Welding…….……38

4.1 Introduction…….……38

4.2 Materials and Modeling …….……39

4.2.1 Temperature dependency of Material properties……...40

4.2.2 Modeling details and Assumption……..41

4.3 Analysis of Heat Conduction…….……..48

4.3.1 Heat Conduction of Al6061-T6 alloy …….……...48

4.3.1.1 Temperature Distributions of Cylindrical pin……...…51
4.3.1.2 Temperature Distributions of Frustum pin…….……...53
4.3.1.3 Temperature Distributions of Threaded pin……..55

4.3.2 Heat Conduction of AZ31B-H24 Mg alloy …….……..56

4.3.2.1 Temperature Distributions of Cylindrical pin…..……..58
4.3.2.2 Temperature Distributions of Frustum pin……..60
4.3.2.3 Temperature Distributions of Threaded pin…….….62

4.4 Analysis of Welding Residual stress…….…….....64

4.4.1 Welding Residual stress of Al6061-T6 alloy…….……64

4.4.1.1 Residual Stresses of Cylindrical pin……..65

4.4.1.2 Residual Stresses of Frustum pin…….……..66

4.4.1.3 Residual Stresses of Threaded pin…….67

4.4.1.4. Compared Residual stress, σ_x, distribution along the weld line according to the tool pin shape……..68

4.4.2 Welding Residual stress of AZ31B-H24 Mg alloy ……...69

4.4.2.1 Residual Stresses of Cylindrical pin……..69

4.4.2.2 Residual Stresses of Frustum pin……...70

4.4.2.3 Residual Stresses of Threaded pin…….....71

4.4.2.4 Compared Residual stress, σ_x, distribution in weld line according to the tool pin shape……...……72

4.5 Discussion on Numerical Analysis results…….……..74

Chapter 5 Measurement of Temperature distributions and Residual stresses.....75

5.1 Measurement of Temperature history……75
5.2 Measurement of Residual stress ……78

Chapter 6 Experiment of Mechanical and Metallurgical Characteristics……..80

6.1 Friction Stir Welding of Al6061-T6, AZ31B-H24 and Al6061/AZ31B alloy....80
6.1.1 Experiment of Al6061-T6 by FSW……...……80
6.1.2 Experiment of AZ31B-H24 by FSW……83
6.1.3 Experiment of Dissimilar Al6061/AZ31B by FSW……..84
6.2 Hardness Profiles of Friction Stir Welding Joints…….86
6.3 Tensile test of Friction Stir Welding Joints…….…...88
6.4 Metallurgical Characteristics in Friction Stir Welding Joints…..…….….89
6.5 Discussion on Mechanical and Metallurgical Characteristics…….…...94

Chapter 7 Conclusion…….…95

References……..…98

ABSTRACT

The Study on Mechanical Behaviors and Metallurgical Characteristics of Welded Part in the Lightweight alloy by Friction Stir Welding

Heung-Ju, Kim
Advisor: Prof. Han-Sur Bang Ph.D
Department of Producing and Processing
Graduate School of Chosun University

Magnesium and aluminium alloy are becoming the materials of choice for many lightweight transports component applications. In the alloyed form, both magnesium and aluminium are structural metal, thereby providing considerable opportunity to improve fuel economy and reduce harmful emissions produced in powering transport when substituted for steel design.

As the density of Mg alloy is one-fifth of iron alloy, it is the lowest among the developed alloy till now. The Mg alloys also have a modulus of non-intensity or non-elasticity enough to stand comparison with other lightweight materials. It is not only excellent in absorptiveness for wave such as vibration, shock and electronic, but also distinguished in quality such as electricity conduction, thermal conduction and processing, or exhaustion and shock on high temperature. It is used for material miniaturization in the industries such as automobile, aerospace and defense machinery. The welding of magnesium alloy turned out to be difficult due to certain factors such as the low melting point, the low evaporation point, the high chemical attraction with oxygen and the generation of metal compound.
Even though Aluminium alloys are light in weight some of them have strength exceeding the mild steel. Al alloys have good ductility at subzero temperatures and have high resistance to corrosion, non-toxic and have an approximate melting range from 482 to 660℃. Due to its high thermal conductivity high rate of heat input in need for the fusion welding of Aluminium alloys. It requires new welding method to be developed for productivity and high quality of products because of the difficulty in applying the conventional welding processes (resistance and arc welding, etc) to aluminium alloy. In short the similar and dissimilar welding of these alloys using the fusion welding is not feasible.

According to the trend, the uses of Magnesium and aluminum alloy are increasing in auto mobile and aerospace industries. As the use of these alloys increase, the research concerns about the similar and dissimilar welding of these alloys are also increase. Friction stir welding (FSW) offer great promise as a means of joining similar and dissimilar alloys and producing welds with superior metallurgical properties and strengths. Significant cost reductions and novel combinations of

materials and designs may be achieved by FSW. Although FSW is performed at temperatures well below the melting point of the alloys, complex thermal and plastic strain gradients are developed during the stirring process. So the mechanical and metallurgical characteristics of FSW welds are to be analyzing in order to supply the fundamental information for the criteria of welding design and construction.

This study is based on dissimilar joining of Mg AZ31B and Al6061-T6 alloy by FSW based on the manufacturing process and examine the systematic or mechanical characteristic that can be generated while welding of these dissimilar alloys. The sheets of Al alloy and Mg alloy were friction stir welded under various combinations of rotating speed and traveling speed and the temperature distributions at the resulting fsw joint was measured using the thermocouples. Also the resulting microstructures were analyzed, using optical microscope (OM) and scanning electron microscope (SEM). The dissimilar FS welded specimen we subjected to tensile testing and after the tensile test SEM test along the tensile fracture surface showed that the crack originated in the intermetallic compound layer with β-$Mg_{17}Al_{12}$ phase and then grown to the base metals with α-Mg and Al phase. In the x-ray diffraction test, diffraction profiles of the fractured area of the dissimilar welded joint $Mg_{17}Al_{12}$ intermetallic compound were identified. Shortly it is indicated that the welded joint was fractured at the $Mg_{17}Al_{12}$ intermetallic compound layer. The identified results of the intermetallic compound were agreed to the results determined by EPMA. Due the presence of this intermetallic compound layer the tensile strength of the dissimilar welded Mg AZ31B and Al6061-T6 alloy is less compared to the similar welded Al-Al and Mg-Mg alloy specimens.

The choice of process parameter especially the rotational speed and traveling speed have a significant effect on the control and optimization of the process. So various FS Welding was carried out in various combinations of travel speed and rotation speed for similar and dissimilar welding of this alloys. The results indicate, Al6061-T6 alloy, rotating speed 1000rpm, travel speed 200mm/min. AZ31B-H24 rotating speed 2000rpm, travel speed 100mm/min. and Al6061/AZ31B dissimilar FS welding rotating speed 450rpm, travel speed 15mm/min shows good bead and optimization conditions.

In order to numerically calculate temperature and residual stress distribution in welds, finite element heat source model is developed on the basis of experiment results and characteristics of temperature and residual stress distribution in dissimilar welds are understood from the result of simulation. For the finite element stimulation of the heat transfer and residual stress analysis in the FSW, three models with different tool pin shape such as Cylindrical shaped pin, Frustum shaped pin and Threaded pin were used. The thermal and residual stress distributions for the three types of pin configuration were simulated and results were compared. Al6061 FSW Calculated Max. Temperature distribution follows; Frustum pin (448.47) > Cylindrical pin (442.76) > Threaded pin (441.02). And, AZ31B-H24 FSW Calculated Max. Temperature distribution follows; Frustum pin (474.27) > Cylindrical pin (469.21) > Threaded pin (463.56) (Unit : ℃). The maximum temperature measured using the thermo couple at Stir zone (AS) of Al6061 alloy is about 470℃, in Stir zone (RS) is about 380℃, which is lower than Mg alloy. And, Al6061/AZ31B dissimilar FSW temperature distribution for Cylindrical pin was about 509℃, Frustum pin 467℃, Threaded pin 464℃.

Al6061-T6 FSW Calculated Max. Residual stress distribution follows; Frustum pin (50.15) > Cylindrical pin (49.48) > Threaded pin (49.25). And, AZ31B-H24 FSW Calculated Max. Residual stress distribution follows; Frustum pin (49.48) > Cylindrical pin (45.09) > Threaded pin (34.51).

(Unit:Mpa).

So from the simulation and experimental results, the Threaded pin case is advantages from the point of view of weld efficiency and process stability. Also maximum temperature and residual values are less compare to other pins.

The aluminum has large thermal expansion coefficient and the mechanical melting point is lower than mg alloy. Numerical (finite element) thermal models are used to predict the thermal histories in trial welds. The main contribution of this thesis is as follows: (a) two-dimensional optimization of thermo-elasto-plastic process, (b) evaluation of material property sensitivity to welding residual stress, (c) FE analysis for elastic rate-independent plastic material with equilibrium equation.

List of Figure

Fig. 1.1 Aluminum major applications……...……13

Fig. 1.2 Basic Principle of Friction Sir Welding……14

Fig. 1.3 Typical FSW Optimum Joint Type……...……16

Fig 2.1 Heat generation model of FSWelding……25

Fig. 2.2 Heat generation Estimates of tool pin……...……26

Fig. 3.1 Elasto-plastic strain hardening behavior for the uniaxial case……...……35

Fig. 3.2 Forces and displacement for a two-node element……..……36

Fig. 4.1 The geometry model and the boundary conditions of FSW……..……38

Fig. 4.2 physical properties of Al606-T6 Alloy……..……40

Fig. 4.3 Physical properties of AZ31B Mg alloy……...……40

Fig. 4.4 Mechanical properties of Al606-T6 Alloy for thermal elasto-plastic analysis……..……41

Fig. 4.5 Mechanical properties of AZ31B Mg alloy for thermal elasto-plastic analysis…...……41

Fig. 4.6 Two-dimensional model for Finite element analysis……..……43

Fig. 4.7 Boundary conditions for heat conduction and thermal elasto-plastic analysis……..……43

Fig. 4.8 Simulation objects and coordinates system for Cylindrical pin……45

Fig. 4.9 Simulation objects and coordinates system for Frustum pin……46

Fig. 4.10 Simulation objects and coordinates system for Threaded pin……47

Fig. 4.11 Calculated temperature distribution according to the Cylindrical pin using isothermal contour in FSWelded……51

Fig. 4.12 Calculated temperature distribution according to the Cylindrical pin using isothermal contour in FSWelded……...…52

Fig. 4.13 Calculated temperature distribution according to the time variation according to the Cylindrical pin (Al6061-T6 alloy) …...……...…52

Fig. 4.14 Calculated temperature distribution according to the Frustum pin using isothermal contour in FSWelded……..……53

Fig. 4.15 Calculated temperature distribution according to the Frustum pin using isothermal contour in FSWelded……..……54

Fig. 4.16 Calculated temperature distribution according to the time variation according to the Frustum pin (Al6061-T6 alloy)…...……54

Fig. 4.17 Calculated temperature distribution according to the Threaded pin using isothermal contour in FSWelded……..……55

Fig. 4.18 Calculated temperature distribution according to the time variation according to the Threaded pin (Al6061-T6 alloy)……..……55

Fig. 4.19 Calculated temperature distribution according to the Cylindrical pin using isothermal contour in FSWelded……58

Fig. 4.20 Calculated temperature distribution according to the Cylindrical pin using isothermal contour in FSWelded……58

Fig. 4.21 Calculated temperature distribution according to the time variation according to the cylindrical pin (AZ31B-H24 alloy) ……59

Fig. 4.22 Calculated temperature distribution according to the Frustum pin using isothermal contour in FSWelded……59

Fig. 4.23 Calculated temperature distribution according to the Frustum pin using isothermal contour in FSWelded……..……61

Fig. 4.24 Calculated temperature distribution according to the time variation according to the Frustum pin (AZ31B-H24 alloy) ……61

Fig. 4.25 Calculated temperature distribution according to the Threaded pin using isothermal contour in FSWelded……..……62

Fig. 4.26 Calculated temperature distribution according to the Threaded pin using isothermal contour in FSWelded……..…63

Fig. 4.27 Calculated temperature distribution according to the time variation according to the Threaded pin (AZ31B-H24 alloy) ……..…63

Fig. 4.28 Residual stress distribution of Cylindrical pin and magnified…….....…65

Fig. 4.29 Residual stress distributions of Frustum pin and magnified……...…66

Fig. 4.30 Residual stress distributions of Threaded pin and magnified…….....…67

Fig. 4.31 Residual stress, σ_x, distribution in weld line according to the tool pin shape from the crown 1mm and magnified (Al6061-T6 alloy) ……..……68

Fig. 4.32 Residual stress distribution of Cylindrical pin and magnified……69

Fig. 4.33 Residual stress distributions of Frustum pin and magnified……...……70

Fig. 4.34 Residual stress distributions of Thread pin and magnified……..……71

Fig. 4.35 Residual stress, σ_x, distribution in weld line according to the tool pin shape from the crown 1mm and magnified (AZ31B-H24 alloy) ……....……72

Fig. 5.1 Workpiece dimensions and location of Thermocouples……...……75

Fig. 5.2 Measured temperature distribution of FSWelded joints Al6061 -T6 alloy……...……76

Fig. 5.3 Measurement of temperature of FSWelded joints dissimilar Al6061/AZ31B alloy…….77

Fig. 5.4 Temperature distribution of FSWelded dissimilar joint of AZ31B/A6061 alloy……...…77

Fig. 5.5 Dimension details of specimen used in the experiment……78

Fig. 5.6 Comparison the residual stress distributions from simulation and experimental results in Al 6061-T6 alloy FSW joint……...79

Fig. 6.1 Top and bottom surface of Al6061-T6 alloy FSW butt joint. ……81

Fig. 6.2 Weldability of Al6061-T6 alloy FSWelded……..82

Fig. 6.3 Top and bottom surface of AZ31B-H24 alloy FSW butt joint…….....83

Fig. 6.4 Appearance of dissimilar Al6061/AZ31B alloy FSWelded…….....84

Fig. 6.5 Weldability of A6061, AZ31B and A6061/AZ31B alloy FSWelded……85

Fig. 6.6 Hardness profiles near weld zone Al6061-T6 FSWelded with various welding speed……86

Fig. 6.7 Hardness profiles near weld zone AZ31B-H24 alloy FSWelded with various welding conditions……...87

Fig. 6.8 Hardness profiles near weld zone of dissimilar Al6061/AZ31 alloy FSWelded……...…87

Fig. 6.9 Tensile properties of FSW joints……...……88

Fig. 6.10 Microstructures of Al6061-T6 alloy FSWelded. ……89

Fig. 6.11 Microstructures of AZ31B-H24 Mg alloy FSWelded. ……...…….90

Fig. 6.12 Macro and microstructure feature of dissimilar Al6061/AZ31 alloy FSWeled……...…91

Fig. 6.13 Concentration profiles of Mg and Al atoms across dissimilar Al6061/AZ31B alloy FSWelded…….. 91

Fig. 6.14 X-ray diffraction pattern of stir zone……...……92

Fig. 6.15 Tensile fracture surface of dissimilar Al6061/AZ31 alloy FSWeled by SEM……93

List of Table

Table 1.1 Typical Applications for FSW……15

Table 4.1 Physical properties of Al6061-T6 alloy for heat conduction analysis……39

Table 4.2 Physical properties of AZ31B Mg alloy for heat conduction analysis……...……39

Table 4.3 Experiment conditions of friction stir welding for butt joint……42

Table 4.4 Dimensions of tool pin shape……..…44

Table 4.5 Simulation condition for Cylindrical pin……45

Table 4.6 Simulation condition for Frustum pin……46

Table 4.7 Simulation condition for Threaded pin……..…47

Table 4.8 Chemical composition and Mechanical properties of Al6061-T6 alloy……48

Table 4.9 Friction stir welding Conditions of Al6061-T6 alloy……..…49

Table 4.10 Input data for the calculation of Al6061-T6 alloy……49

Table 4.11 Simulation conditions for FSW according to the tool pin shape…….....…49

Table 4.12 Heat input of Al 6061-T6 alloy FSWelding (1000rpm, 200mm/min) ……...49

Table 4.13 Chemical compositions and Mechanical properties of AZ31B- Mg Alloy……56

Table 4.14 Friction stir welding Conditions of AZ31B- Mg Alloy……56

Table 4.15 Input data for the calculation of AZ31B- Mg Alloy…….……56

Table 4.16 Simulation conditions for FSW according to the tool pin shape……..57

Table 4.17 Heat input of AZ31B-H24 alloy according to the tool pin shape……57

Table 4.18 Mechanical properties of Al6061-T6 alloy……64

Table 4.19 Calculated maximum Residual stress for different pin shapes in Al6061-T6……..…68

Table 4.20 Calculated maximum Residual stress for different pin shapes in AZ31B-H24 alloy….73

Table 4.21 Calculated maximum temperature values for different pin shapes……74

Table 4.22 Calculated maximum Residual stress for different pin shapes……74

Table 6.1 Experiment conditions of Al6061-T6 alloy FSW butt joint……...81

Table 6.2 Experiment conditions of AZ31B-H24 alloy FSW butt joint……83

Table 6.3 Experiment conditions of dissimilar Al6061/AZ31B alloy FSWeled……84

Chapter 1

INTRODUCTION

1.1 Backgrounds to the research

Aluminium is a young and modern metal. They are used widely for application where their low specific gravity, high conductivity, good resistance to corrosion, relatively good mechanical properties, and high recycle potential and other characteristics are required. The Al metal makes a key contribution in the manufacturing of fuel-efficient engines in cars and trucks, as well as to high-speed rail and sea travel. By reducing the vehicle's weight, it cuts down on fuel consumption and emissions without compromising size or safety. Fig. 1.1 shows the aluminum major applications.

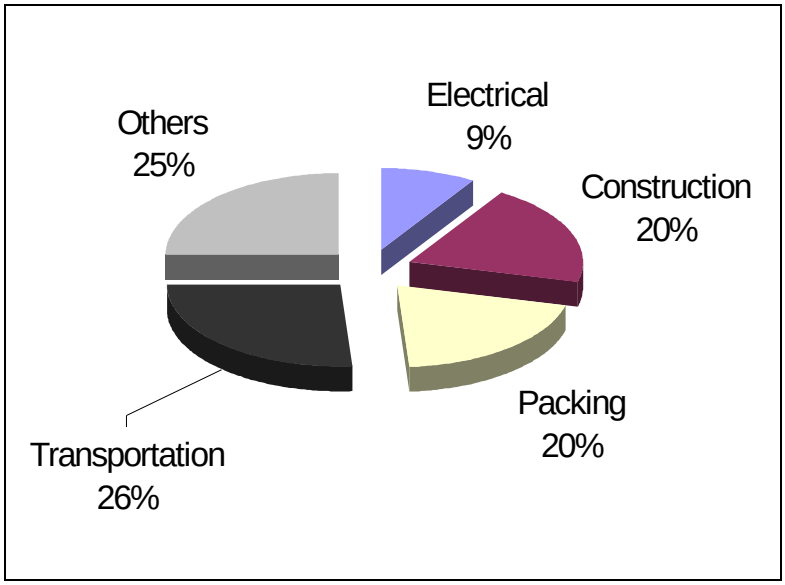

Fig. 1.1 Aluminum major applications

Magnesium is now becoming the material of choice for many lightweight transport component applications, demonstrated by continued, steady market growth., magnesium is the lightest structural metal, thereby providing considerable opportunity to improve fuel economy and reduce harmful emissions produced in powering transport when substituted for a heavier aluminum or steel design. Magnesium alloys are strong, lightweight structural materials with strengths comparable to strong aluminum alloys. With densities 36% less than aluminum and 78% less than steel, magnesium alloys have excellent strength-to-weight ratios. However, magnesium is used as a structural metal in an alloyed form and most magnesium alloys have a slightly higher density.
Magnesium and its alloys exhibit low densities and high specific strengths, these advantages are the driving force for the use of magnesium based materials in transportation industries, where significant weight savings can still be made and hence, fuel consumption and emission reduced. In

automobiles the most interesting area for magnesium usage is the front section where the engine is located. Any reduction in weight in this area will help to improve the performance and weight balance of a car. The uses of magnesium largely center on 3 properties of the metal: 1) Its ability to form intermetallic compounds with other metals. 2) Its high chemical reactivity. 3) Its low density.

Friction Stir Welding (FSW) was invented in 1991 and patented by The Welding Institute (TWI) [1, 2]. It was apparent that the FSW process was flexible and simple, with many potential advantages, from quality improvements, to cost savings. This was especially evident for materials, such as aluminum, that are difficult to join with traditional processes. It is a solid state welding process in which a spinning non-consumable tool is forced along the joint line, heating the abutting components by friction, and producing a weld joint by extrusion, forging and large scale plastic flow stirring of the material from the two components, in the vicinity of the tool.

The FSW process is inherently simple, with few variables. The basics of the process are illustrated in Fig. 1.2. During the FSW process, a rotating FSW tool is plunged into the material at the joint interface. The tool comprises a shoulder and a pin. As the FSW tool travels along the joint, the friction generated by the shoulder and the pin heats the surrounding material and rapidly produces a plasticized zone around the pin. Pressure provided by the pin forces plasticized material to the rear of the pin where it consolidates and cools to form a bond. Pressure provided by the pin forces plastic-like material to the rear of the pin where it consolidates and cools to form a bond. The only variables in the process are the rotation speed, travel speed, FSW tool design, and tool orientation and position. Once the proper tool design, rotation speed, travel speed, etc. are selected, this simple process ensures high quality, repeatable welds. The bond is not actually made of plastic, but it shows many plastic-like properties, making the bond incredibly strong without damaging the original material. And it provides twice the fatigue resistance of fusion welds with no gaps in the weld minimizes material distortion and allows safe operation by not creating hazards such as welding fumes, radiation, high voltage, liquid metals, or arcing.

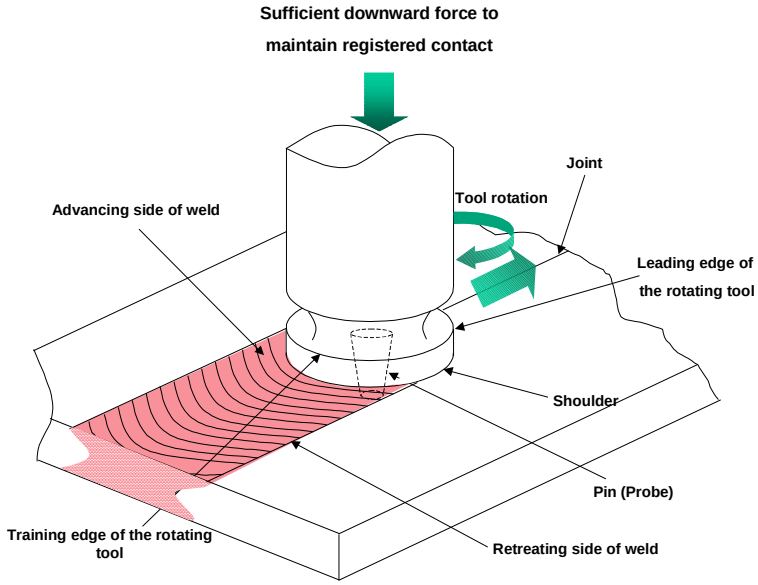

Fig. 1.2 Basic Principle of Friction sir welding

And, today a variety of materials can be welded such as aluminum and its alloys, magnesium alloys, copper and its alloys, lead, titanium and its alloys, zinc, plastics, and recently, joining high melting point metal like steel using FSW has been reported [3]. The process uses a nonconsumable tool with no filler material and with no need of shielding gas when welding aluminum. The thickness can vary from 1 mm to 50 mm depending on material or welding conditions. FSW can produce welds that are high in quality, strong, and inexpensive to make with absence of oxidation and porosity. FSW delivers many advantages over conventional fusion welding processes such as no fumes, no welding arc, low heat input, and almost no weld finishing costs.

FSW opens up the possibility of joining operations that are difficult or even impossible using fusion welding techniques. Successful development of such technique will enable efficient and rapid incorporation of high-performance materials into a wide variety of industrial products. A short list of possible applications in various industries is shown in Table 1. Most of the listed applications concentrate on the joining of aluminum, as the FSW process is most advanced in this area and with other lower melting point materials. Other materials that can be joined include magnesium, copper, lead, titanium, and steel. The applications can range from 0.5 mm in thickness to over 50 mm in thickness.

Table 1.1 Typical Applications for FSW

Industry	Specific application	Present Process	Advantage of FSW
Electrical	Heat sinks-welded laminations	GMAW	Higher density of fins-better conductivity
Electrical	Cabinets, enclosures	GMAW, RSW	Reduced cost, weld through corrosion coatings
Batteries	Leads	Solder	High quality
Military	Shipping pallets	GMAW	Reduced cost
Extrusions	Customized extrusions	Not done today	Can customize, reduces need for large press
Boats	Keel, tanks	Rivet, GMAW	Stronger, less distortion
Golf cars, Snowmobiles	Chassis, suspension	GMAW	Less distortion, better fatigue life
Tanks, cylinders	Fittings, long & circum seam	GMAW	Higher quality-less leaks, higher uptime
Aerospace	Floors, wing spars	Rivets	Higher quality, cheaper (no rivet & holes)

Cost advantages result because no consumables such as gas, wire, or fasteners) are required, less repair and rework occurs, little to no material preparation is needed, and there is a reduced need for environmental protection because there is no noise, fumes, UV light, spatter, etc. The quality related advantages of FSW include weld geometry and penetration consistency, improved yield and tensile strength, as well as improved fatigue life. Furthermore, the process avoids many of the problems with traditional processes. Typical fusion welding problems include poor weld penetration, low weld and HAZ zone mechanical properties, poor welding uptime, propensity for weld cracking and porosity, excessive distortion, etc. The quality improvements versus the traditional processes are more pronounced in harder to join materials, such as 2XXX and 7XXX series aluminum.

The applications of FSW have been reported and commercialized in many industrial sectors especially in transportation, e.g. ship [4], railway car [5], automotive, airplane and rocket fuel tank [4], in which aluminum usage is increasing for the sake of weight reduction. FSW has also applied to copper alloys such as copper containment canister for nuclear waste [6, 7] or copper backing plate for the spattering equipment [8]. In this case, electron beam welding (EBW) has also been developed and compared with FSW in terms of weld quality and cost reduction. On this moment, the industrial applications are limited to aluminum alloys and copper alloys as mentioned above which provides the obvious advantages for relatively low melting temperature materials.
As a result of the early stage of development of this exciting joining technology, the required knowledge base is fragmentary for joints between like materials and it is nearly non-existent for joints between dissimilar materials.

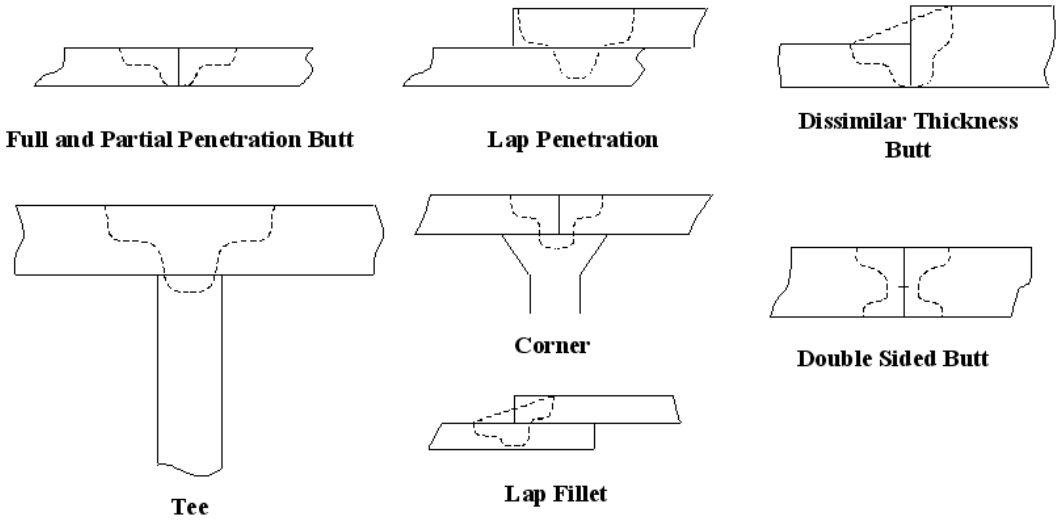

Fig. 1.3 Typical FSW Optimum Joint Type

Reliability assessment and verification of the welding design and construction criteria for welds formed by FS welding are conducted through the experiment and numerical simulation. In the simulation, heat source modeling is included for FS welding and temperature dependency of material properties is considered especially.

1.2 Scopes and Objective

In the automotive industries, one of the main issues is to reduce the weight of structures for saving fuel consumption, prevention of air pollution and improvement of performance. For this purpose, many efforts have been tried to substitute standard material of car body by using light metal alloys.

Therefore, technical and economical needs for joining of light-weight metals by joining process satisfying productivity and quality will be increased in future automotive industry. Especially, use of Al and Mg alloys is considered for their superior material characteristics such as high strength to weight ratio, good recycle-ability and noise & vibration resistance.

Al-alloy has the good property of hot and cold working and corrosion-resistant. However the Al-alloy welding with the existing fusion weld needs a skillful welding to prevent defect. In Friction Stir Welding (FSW) defect are comparatively less than that of fusion welding and so being applied in various industry fields. In this study, to analyze accurately the mechanical properties of joining area of FSW of Al 6061 alloy, thermal-elastic-plastic finite analysis program with finite element method has been used. The size of HAZ and the thermal distributions are simulated and the mechanical property around the FSW joining area to the Al 6061-T6 alloy is examined. Successful application of the FSW for joining Al6061 alloy would increase its applications to various structure components, particularly in the aerospace industry due to its lightweight and high strength.

In the present study, effectiveness of butt joint Al6061/Al6061, AZ31B/AZ31B and Al6061/AZ31B alloy were carried out by friction stir welding process in order to investigate relationship among process parameters, formation of intermetallic compounds and final strength in welds. As a result, many aspects such as defects and intermetallic compounds could be controlled to achieve the high strength in the joint. For this purpose, the present paper conducts two-dimensional nonlinear thermal and thermo-mechanical simulations for the FSW of Al alloy and Mg alloy using the finite element analysis.

The results are then discussed relative to the process, the tool and the heat transfer and temperature distribution in both the tool and the workpiece. And, 3 type tool pin shapes, termed; cylindrical pin, frustum pin and threaded pin, are simulated to compare the variation in heat flux generation from different tool pin shapes in FSW process. Also Al6061-T6 alloy and AZ31B-H24 alloy were FSW butt jointed varying the process parameters (rotating speed, traveling speed, etc) and investigated the characteristics based on metallurgical aspects of welds (BM, HAZ, TMAZ, SZ microstructures etc.) Al 6061-T6 alloys of FSWelding case with tool rotational speeds of 1000rpm and travel speed 200 and 300mm/min were respectively considered. AZ31B-H24 Mg alloys of FSWelding case with tool rotational speeds of 1000, 2000rpm and travel speed 100mm/min are considered. And for dissimilar FSWelding case tool rotational speeds of 450rpm and travel speed 15mm/min is considered.

The temperature and residual stress experimentally obtained were compared to simulation values. Based on the experimental data of transient temperature history at specific locations during FSW, an inverse analysis method for the thermal numerical simulation has been developed. Also the transient temperature and residual stresses on the workpiece is subsequently determined numerically. The results for both transient temperature and residual stresses are compared with the

available experimental data to validate the present simulations.

For this purpose, the characteristics of tool pin shape are simulated for friction stir welding butt joint. Reliability assessment and verification of the welding design and construction criteria for welds formed by FSWelding are conducted through the experiment and numerical simulation. In the simulation, heat source modeling is included for FSWelding and temperature dependency of material properties has been considered.

1.3 Literature Review

FSW is a complex phenomenon. Although the FSW method looks as a simple welding method, without consuming material, the physics behind the process is complex. The method includes heat generation, heat and mass transport. One of the problems in understanding the method is in observing the details of the process in action. Modeling the process would require fever experiments.

Moreover, understanding of why and when voids are present in the weld zone could be established. Models may be validated in a number of ways but the most convincing one is by comparison with high quality experimental data. Many authors, both by analytical and numerical models, have attempted modeling of the FSW process. These models have been both two and three-dimensional and could be based on solid mechanical or fluid dynamic models. Some have included the material flow whereas others have neglected it, which is also the case with the effect of the threaded tool.

In the last decade, a number of researchers have been working on the model and simulate the process experimental methods, analytical or numerical and finite element methods are being employed of heat transfer during FSW.

FSW results in intense plastic deformation around rotating tool and friction between tool and workpieces. Both these factors contribute to the temperature increase within and around the stirred zone. Since the temperature distribution within and around the stirred zone directly influences the microstructure of the welds, such as grain size, grain boundary character, coarsening and dissolution of precipitates, and resultant mechanical properties of the welds, it is important to obtain information about temperature distribution during FSW.

The temperature distribution in workpiece is very important as it affects the thermal stresses development in FSW process. The stress and strain field includes thermal stresses induced to the joint during the welding process and is responsible for the residual stress distribution, and the displacement field resulting in the final distortion of the weld joint.

The maximum temperature created by FSW process ranges from 80% to 90% of the melting temperature of the welding material, as measured by Tang et al. [10] and Colegrove et al. [10] and McClure et al. [11], so that welding defects and large distortion commonly associated with fusion welding are minimized or avoided.

Mahoney et al. [12] conducted friction stir welding of 6.35 mm thick 7075Al-T651 plate and measured the temperature distribution around the stirred zone both as a function of distance from the stirred zone and through the thickness of the sheet. It reveals a maximum temperature of 475℃ was recorded near the corner between the edge of the stirred zone and the top surface. And, the maximum temperature within the stirred zone should be lower than the melting point of 7075Al because no evidence of material melting was observed in the weld.

An attempt was made by Tang et al. [10] to measure the heat input and temperature distribution within friction stir weld by embedding thermocouples in the region to be welded. 6061Al- T6 aluminum plates with a thickness of 6.4 mm were used. They reported that the thermocouple at the weld center was not destroyed by the pin during welding but did change position slightly due to

plastic flow of material ahead of the pin .At a tool rotation rate of 400 rpm and a traverse speed of 122 mm/min, a peak temperature of 450℃ was observed at the weld center one quarter from top surface. Second, there is a nearly isothermal region 4 mm from the weld centerline.

Colegrove et al. [13] performed simulation of FSW for both thermo and material flow including the pin.

Russel and Shercliff [14] postulated a heat input dependent upon the shear strength of the material.

Using an assumed friction coefficient, Frigaard et al. [15] arrived at a formula for heat generation in their modeling.

Gould and Feng [16] proposed a simple model for temperature distribution in workpiece.
Chao and Qi [17, 18, 19] developed a moving heat source model in a finite element analysis for studying the temperature, residual stress and distortion of the FSW process. The model is based on the assumption that the heat generation comes from sliding friction between the tool and material. This is done using Coulomb's law to estimate the friction force. Moreover, the pressure at the tool surface is set constant and thereby enabling a radially dependent surface heat flux distribution generated by the tool shoulder. In this model the heat from the pin is neglected.

Xu [20] have used finite element models to describe the material flow around the pin. This is done using a solid mechanical two-dimensional finite element model. It includes heat transfer, material flow, and continuum mechanics. The heat input from the tool shoulder is assumed to be linearly proportional to the distance from the center of the tool. To model the workpiece the code WELDSIM was used. It is a transient, nonlinear, 3- dimensional finite element code. In this model only half the workpiece is modeled due to symmetry. This means that no adjustment has been made between the advancing and the retreating side of the weld. The conclusions from this work indicate that 95 % of the heat generated goes into the workpiece and it is only 5% that goes to the tool. This gives very high heat efficiency.

In Chao[21] presents another three-dimensional heat transfer finite element model for model assuming a constant heat flux from the tool shoulder and a trial-and-error procedure to adjust the heat input until all the calculated temperatures matched with the measured ones of FSW. Their model includes a decoupled heat transfer and subsequent thermo-mechanical analysis. The temperature fields during the welding, residual stress distribution and distortion of the work piece after the FSW process were studied. The modeling effort includes a coupled heat transfer and a subsequent thermo-mechanical analysis. The temperature fields during the welding, residual stress distribution and distortion of the workpiece after the FSW process are studied. The effects of the fixture used to clamp the workpiece to the backing plate and the reduction of yield strength near the weld nugget area are incorporated in the modeling.

Gould and Feng [22] used the Rosenthal equation for developing an analytical model for the heat transfer of the workpiece during FSW.

Xu [23] has tried to optimize the welding tool design and the selection of the FSW process parameters. Variations in process conditions are made, such as tool shoulder diameter, tool advancing speed and thermal insulation conditions. The finite element simulation included heat generation due to the tool-workpiece interaction, the heat loss through the tool and the backing

plate.

Zhu et al [24] use a three-dimensional nonlinear thermal and thermo-mechanical numerical model. The finite element analysis code was WELDSIM. The objective was to study the variation of transient temperature and residual stress in a friction stir welded plate of 304L stainless steel. Based on the experimental records of transient temperature, an inverse analysis method for thermal numerical simulation was developed. After the transient temperature field was determined, the residual stresses in the welded plate were then calculated using a three-dimensional elastic-plastic thermo-mechanical simulation. In this model the plastic deformation of the material is assumed to follow the von Mises yield criterion and the associated flow rule.

Frigaard, Chao, Y. J., [25, 26] developed a 2D numerical heat input flow model from the shoulder and the pin as fluxes on squared surfaces at the top and sectional planes on the finite difference method with a moving heat source. The results showed that the temperature in the front of the tool is most critical; hence the parent material needs to be pre-heated to a certain temperature in order for it to sustain the severe plastic deformation cause by friction stirring.

Chen and Kovacevic [27] have studied the thermal history and thermo-mechanical process in the butt-welding of Al alloy 6061-T6. Its use a 3D model based on a finite element method to study the thermal history and stress distribution in the weld and compute mechanical forces in the longitudinal, lateral and vertical directions. The heat source incorporated in the model involves the friction between the material and the probe and the shoulder. From the thermal history of the FE model, the stresses in the friction stirred weld are numerically simulated. As the temperature increases the friction coefficient decreases. Also Russell and Shercliff [14] used this method.

Song and Kovacevic [28, 29] used a melting temperature at the interface as a moving heat source to model the thermal fields in a FSW. It presented detailed 3D heat transfer model. They introduced a moving coordinate to reduce the difficulty of modeling a moving tool. Heat input from the tool shoulder and the pin were considered in the model. The heat input from the tool pin is modeled as a moving heat source, and the heat transfer process of the tool and workpiece is indirectly coupled at the interface. This model can be applied to both tool and the work piece. The important conclusion of their work is that preheating the work-piece was proven to be beneficial to FSW.

Lawrjaniec et al [30] have developed a three-dimensional numerical model to investigate residual stresses generated by FSW. The modeling is carried out using two commercial finite element codes SYSWELD and MARC. A thermal-mechanical transient state is used for the calculations. The thermal stage of the process is simulated using two different numerical heat sources. Those numerical heat inputs are calibrated with the help of experimental results obtained by thermocouples and infrared cameras.

Khandkar et al [31] use a finite element method based on a 3-dimensional with a moving heat source to study the temperature distributions during for FSW lap welding. The moving heat source generated by the rotation and linear traverse of the pin-tool has been correlated to input torque data obtained from experimental investigation of butt-welding. Temperature dependent properties of the weld-material have been used for the numerical modeling.

Fourment [32] tries to simulate the transient phases of FSW with FEM in the form of an Arbitrary Lagrangian Eulerian (ALE) formulation, to develop a 3-D coupled thermomechanical model taking

large deformation into account. This method permits both transient and steady state phases.
Schmidt et al [33] have developed an analytical equation for heat generation. The heat generation from the tool is governed by the contact condition, i.e. whether there is sliding, sticking or partial sliding/sticking. The heat is generated both by friction and plastic dissipation. Finite element software is chosen and a 3-D dynamic solid-mechanical model including material flow and heat generation can be performed.

Desrayaud [34] uses a tree dimensional analytical thermo-mechanical model to predict the temperature and microstructure. Strain, strain rate and temperatures are used as input data for microstructural model including both dynamic and static recrystallisation.

Colligan [35] documented the movement of the material during FSW of AA7075 as a means of developing a conceptual model of the deformation process. From the results he concluded that the material movement is either by simple extrusion or chaotic mixing, depending on where the weld zone material originates. He had used two new techniques to document the movement of the material during FSW, namely steel shot tracer technique and stop action test. Based on his study of welds in 6061 and 7075 it is evident that much of the material movement takes place by simple extrusion.

Tang et al. [9] further investigated the effect of weld pressure and tool rotation rate on the temperature field of the weld zone. It was reported that increasing both tool rotation rate and weld pressure resulted in an increase in the weld temperature.

Similarly, 3-dimensional thermal model based on finite element analysis developed by Chao and Qi [36] and Khandkar and Khan [37] also showed reasonably good match between the simulated temperature profiles and experimental data for both butt and overlap FSW processes. Arbegast and Hartley further examined the effect of parameters of FSW on temperature [38]. It was noted that there was a slightly higher temperature on the advancing side of the joint where the tangential velocity vector direction was same as the forward velocity vector.

1.4 Thesis Organization

This thesis is introducing first the typical Application for FSW for the similar and dissimilar welding of lightweight Al 6061-T6 alloy and MgAZ31-B alloy.

After this introductive chapter, two chapters are dedicated to these topics.

In Chapter 2, thermal behavior and equations for 2-D Finite Element Model for FSW are presented. It includes a first section describing the Theoretical basic for Analysis. Then the 2-D heat conduction theory of Friction Stir Welding has been described followed by the 3-D Heat Conduction Theory of Friction Stir Welding.

In Chapter 3, dedicated to Thermal elastic-plastic Theory of Friction Stir Welding: Basic theory for Thermal stress analysis, and finally, this Chapter ends with the description of the Elastic-plastic material behavior.

The Chapter 4 is dedicated to the Numerical Analysis on Friction Stir Welding. Temperature dependency of Material properties, modeling details and assumption, and heat conduction and residual stress analysis for the 3 different tool pin types (Cylindrical, Frustum, and Threaded) are described. After having developed all these theoretical topics, the two Experimental measurement details chapters are included.

In the Chapter 5, measurement of temperature distributions and residual stress is included.

In the Chapter 6, Experiment for determination of Mechanical and Metallurgical Characteristics has been included.

To conclude, the Chapter 7 summarizes what can be said at the present time about the work done up till now and it gives some perspectives for future developments.

The thesis as a whole demonstrates a new approach to the modeling of friction stir welding. The developed finite element method for FSW produced for this model is shown to be flexible enough to model the temperature distribution and mechanical bebavior present in friction stir welding.

Chapter 2

Heat conduction Theory for Friction Stir Welding

2.1 Introduction

The rapid development of computers has made the use of numerical techniques more appealing and feasible. A number of studies have been carried out on the metallurgical characteristics of friction stir welding and processing in aluminum alloys and magnesium alloy. Some simplified analytical models have also been used to analyze the heat flow and distribution during friction stirring which could be related with microstructure evolved in order to optimize and make the process commercially viable. Finite element method is one of the methods which have proven to be the best for predicting and understanding a process especially when it is complex and new.

In this work an attempt is made to understand the phenomena associated with FSW and compare it with the experimental data. The presented results are preliminary and have to be improvised further. The present study mainly focuses on analyzing the temperature distribution and residual stresses during FSW using the finite element method (In-House Solver).

2.2 Theoretical Basis for Analysis

2.2.1 2-D Heat conduction Theory of Friction Stir Welding

This heat produced by the friction contact between the pin tool and the plates is concentrated locally, and propagates rapidly into remote regions of the plates by conduction according to Eq. (1) as well as convection and radiation through the boundary. It is assumed that the heat flux, $q(r)$, is linearly distributed in the radial direction of the pin tool shoulder, and has the following form [4]:

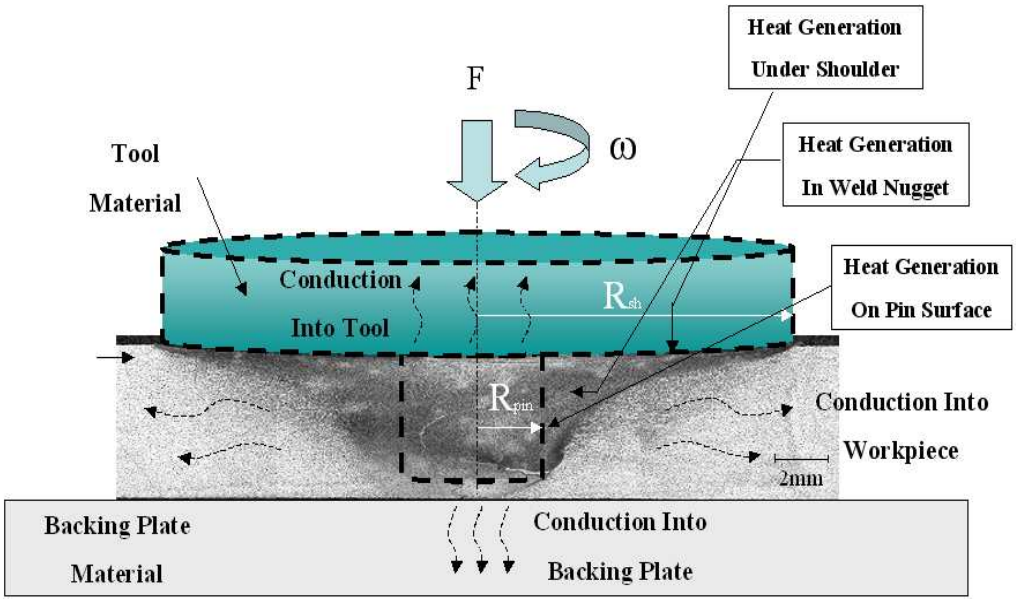

Fig. 2.1 Heat generation model of FSWelding

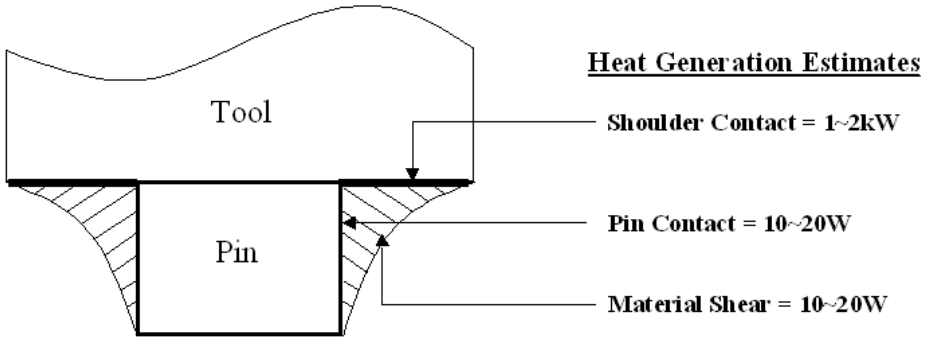

Fig. 2.2 Heat generation Estimates of tool pin

Heat generations during FSW

$$M = \int_0^{M_r R} dM = \int_0^R \mu P(r) 2\pi r^2 dr = \frac{2}{3}\mu\pi P R^3 \qquad \text{Equation (2.1)}$$

Where M is the interfacial torque, μ is the friction coefficient, R is the surface radius, and $P(r)$ is the pressure distribution across the interface (here assumed constant and equal to P). If all the shearing work at the interface is converted into frictional heat, the average heat input per unit area and time becomes

$$q_0 = \int_0^{M_r} \varpi 2dM = \int_0^R \varpi 2\pi\mu \Pr^2 dr \qquad \text{Equation (2.2)}$$

where q_0 is the net power (in Watts) and v is the angular velocity (in rad/s). The next step is to express the angular velocity in terms of the rotational speed N (in rot/s). By substituting ω= 2pN into equation (2.3), we get [39]

$$q_0 = \int_0^R 4\pi^2 \mu P N r^2 dr = \frac{4}{3}\pi^2 \mu P N R^3 \qquad \text{Equation (2.3)}$$

From equation (2.3), it is obvious that the heat input depends both on the applied rotational speed and the shoulder radius, leading to a non-uniform heat generation during welding. These parameters

are the main process variables in FSW, since the pressure *P*, in practice, cannot exceed the actual flow stress of the material at the operating temperature if a sound weld without depressions is to be obtained.

In order to describe the heat source in the numerical model, it is more convenient to express the heat generation as a sum of individual contributions

$$q_0 = \frac{4}{3}\pi^2 \mu P N \sum_{i=1}^{n} (R_i^3 - R_{i-1}^3) \qquad \text{Equation (2.4)}$$

Based on equation (2.4) the heat generation in different position beneath the tool shoulder can be calculated.

2.2.2 3-D Heat Conduction Theory of Friction Stir Welding

The main heat source in FSW is generally considered to be the friction between the rotating tool and the welded plates The heat generation from the plastic deformation of the material is considered to some extent in the model with the use of variable friction coefficient and not explicitly accounted for as a heat source. The heat generated at the surface of the tool is transferred into the tool following the Fourier's law of heat conduction. The heat transfer equation for the tool in a static coordinate system is:

$$\rho c \frac{\partial (T)}{\partial t} = \frac{\partial}{\partial x}\left(k_x \frac{\partial T}{\partial x} \right) + \frac{\partial}{\partial y}\left(k_y \frac{\partial T}{\partial y} \right) + \frac{\partial}{\partial z}\left(k_z \frac{\partial T}{\partial z} \right) \qquad \text{Equation (2.4)}$$

where T is the temperature, c is heat capacity, r is the density and kx, ky, kz are heat conductivities that vary with temperature in the calculations. The aluminum workpiece is considered to have isotropic material property and same value of thermal conductivity is used for all three directions. The coordinate system moves over the workpiece in the positive x-axis at a velocity vx. The heat transfer equation for the workpiece is:

$$\rho c\left(\frac{\partial T}{\partial t} + v_x \frac{\partial T}{\partial x} \right) = \frac{\partial}{\partial x}\left(k_x \frac{\partial T}{\partial x} \right) + \frac{\partial}{\partial y}\left(k_y \frac{\partial T}{\partial y} \right) + \frac{\partial}{\partial z}\left(k_z \frac{\partial T}{\partial z} \right) \qquad \text{Equation (2.5)}$$

where T is the temperature, c is heat capacity, r is the density, kx, ky, kz are heat conductivities, and vx is the welding speed. The conduction and convection coefficients on various surfaces play an important role in the determination of the thermal history of the workpiece in friction stir welding. The initial and boundary conditions considered in our model are based on the actual conditions exhibited in experiments with the FSW.

Chapter 3

Thermal elasto-plastic Theory of Friction Stir Welding

3.1 Heat Conduction Analysis

The spatial and temporal temperature distribution satisfies the following governing equation of un-stationary heat conduction:

$$\rho c \frac{\partial T}{\partial t} = \lambda\left(\frac{\partial^2 T}{\partial x^2} + \frac{\partial^2 T}{\partial y^2} + \frac{\partial^2 T}{\partial z^2}\right) + \dot{Q} \qquad \text{Equation (3.1)}$$

where T is temperature (℃), ρ is density (g/cm^3), $\dot{Q}$ is rate of temperature change due to heat generation per volume (cal/cm^3·sec), t is time (sec), λ is thermal conductivity of isotropic material (cal/cm·sec·℃) and c is specific heat (cal/g·℃).

Heat conduction problem for the object of analysis is formulated as the finite element method using Galerkin method. Internal temperature of the element, T , is given by

$$T(x, y, z, t) = [N(x, y, z)]\{\phi(t)\} \qquad \text{Equation (3.2)}$$

where $[N]$ is a shape function matrix shown the relation between nodal temperature and internal temperature of the element. $\{\phi\}$ is the vector of the nodal temperature of the element at time t.

If Galerkin method is applied in Equation (3.1) using $[N]$ as a weighting function at this time, following equation is obtained.

$$\int_{V^e} [N]^T \left\{ \lambda\left(\frac{\partial^2 T}{\partial x^2} + \frac{\partial^2 T}{\partial y^2} + \frac{\partial^2 T}{\partial z^2}\right) + \dot{Q} - \rho c \frac{\partial T}{\partial t} \right\} dV = 0 \qquad \text{Equation (3.3)}$$

where superscript, T, shows transformation of matrix and subscript, V^e, shows the domain of element.

Un-stationary heat conduction problem can be expressed as following finite element expression for an element.

$$[k]\{\phi\}+[c]\left\{\frac{\partial \phi}{\partial t}\right\}=\{f\} \qquad \text{Equation (3.4)}$$

where $[k]$, $[c]$ and $\{f\}$ show the heat conductivity matrix of an element, the heat capacity matrix of an element and the heat flow vector of an element, respectively. They are expressed as follows: [40],[41]

$$[k]=\int_{V^e}\lambda\left(\frac{\partial[N]^T}{\partial x}\frac{\partial[N]}{\partial x}+\frac{\partial[N]^T}{\partial y}\frac{\partial[N]}{\partial y}+\frac{\partial[N]^T}{\partial z}\frac{\partial[N]}{\partial z}\right)dV \qquad \text{Equation (3.5)}$$

$$[c]=\int_{V^e}\rho c[N]^T[N]dV \qquad \text{Equation (3.6)}$$

$$\{f\}=\int_{V^e}\dot{Q}[N]^T dV-\int_{S^e}q[N]^T dS \qquad \text{Equation (3.7)}$$

Boundary conditions on the boundary S_2 to S_4 can be given to substitute q in second term of equation (3.7).

● When the heat flux, q_o, flows from the boundary S_2:

$$\int_{S_2^e}q[N]^T dS=\int_{S_2^e}q_o[N]^T dS \qquad \text{Equation (3.8)}$$

In the case of adiabatic boundary condition, q_o becomes zero (0).

● When heat transfer is on the boundary S_3 for convection:

$$\int_{S_3^e} q[N]^T dS = \int_{S_3^e} \alpha_c (T - T_c)[N]^T dS \qquad \text{Equation (3.9)}$$

If T in the equation (3. 9) is substituted, the equation (3. 9) becomes as bellows:

$$\int_{S_3^e} q[N]^T dS = \int_{S_3^e} \alpha_c [N]^T [N] dS \cdot \{\phi(t)\} - \int_{S_3^e} \alpha_c T_c [N]^T dS \qquad \text{Equation (3.10)}$$

● When heat radiation is on the boundary S_4:

$$\int_{S_4^e} q[N]^T dS = \int_{S_4^e} \alpha_r (T - T_r)[N]^T dS \qquad \text{Equation (3.11)}$$

If T in the equation (3.11) is substituted by the equation (3.2), The equation (3.11) becomes as bellows:

$$\int_{S_4^e} q[N]^T dS = \int_{S_4^e} \alpha_r [N]^T [N] dS \cdot \{\phi(t)\} - \int_{S_4^e} \alpha_r T_r [N]^T dS \qquad \text{Equation (3.12)}$$

$$[k] = \int_{V^e} \lambda \left(\frac{\partial [N]^T}{\partial x} \frac{\partial [N]}{\partial x} + \frac{\partial [N]^T}{\partial y} \frac{\partial [N]}{\partial y} + \frac{\partial [N]^T}{\partial z} \frac{\partial [N]}{\partial z} \right) dV + \int_{S_3^e} \alpha_c [N]^T [N] dS + \int_{S_4^e} \alpha_r [N]^T [N] dS \qquad \text{Equation (3.13)}$$

$$\{f\} = \int_{V^e} \dot{Q} [N]^T dV - \int_{S_2^e} q_0 [N]^T dS + \int_{S_3^e} \alpha_c T_c [N]^T dS + \int_{S_4^e} \alpha_r T_r [N]^T dS \qquad \text{Equation (3.14)}$$

Therefore, finite element formula of an element can be derived as a form of matrix equation including boundary conditions by using equation (3.6), (3.13) and (3.14).

Finite element formula for the whole object analysed is constructed with assembled each matrix of elements and it can be expressed as follows:

$$[K]\{\Phi\}+[C]\left\{\frac{\partial \Phi}{\partial t}\right\}=\{F\} \qquad \text{Equation (3.15)}$$

where $[\Phi]$, $[K]$, $[C]$ and $\{F\}$ show the vector of the nodal temperature in the whole object, the heat conductivity matrix in the whole object, the heat capacity matrix in the whole object and the heat flow vector in the whole object, respectively. They are given as bellows.[42],[43]

$$[\Phi]=\sum_e \phi\,, \quad [K]=\sum_e k\,, \quad [C]=\sum_e c\,, \quad \{F\}=\sum_e f \qquad \text{Equation (3.16)}$$

3.2 Thermal Elasto-plastic Analysis

3.2.1 Basic theory for thermal stress analysis

In the thermal elastic problem, basic equations such as 1) Equilibrium equation, 2) Equation of strain-displacement relation and 3) Equation of stress-strain relation are needed to solve the problem. 1) Equilibrium equation can be replaced by principle of virtual work. These equations, 1) Principle of virtual work, 2) Equation of strain-displacement relation and 3) Equation of stress-strain relation are used in finite element method as the basic equations. Each equation is given in matrix form as follows:

1) Principle of virtual work

$$\int_V \delta\{\varepsilon\}^T\{\sigma\}dV - \int_V \delta\{U\}^T\{\overline{F}\}dV - \int_{S_\sigma} \delta\{U\}^T\{\overline{T}\}dS = 0 \qquad \text{Equation (3.17)}$$

where $\{\sigma\}$: stress vector, $\{\varepsilon\}$: strain vector, $\{U\}$: displacement vector, $\{\overline{F}\}$: body force vector per unit volume, $\{\overline{T}\}$: surface force vector per unit area, V : volume of an object, and S_σ : area given mechanical boundary condition.

2) Equation of strain-displacement relation

$$\{\varepsilon\} = [A]\{U\} \qquad \text{Equation (3.18)}$$

where matrix $[A]$ includes the differential operator.

3) Equation of stress-strain relation

$$\{\varepsilon\} = \{\varepsilon^e\} + \{\varepsilon^T\} \qquad \text{Equation (3.19)}$$

where $\{\varepsilon\}$: total strain vector, $\{\varepsilon^e\}$: elastic strain vector and $\{\varepsilon^T\}$: thermal strain vector.

The relation between $\{\sigma\}$ and $\{\varepsilon^e\}$ follows the Hook's law and is expresses as bellows.

$$\{\sigma\} = [D^e]\{\varepsilon^e\} \quad \text{Equation (3.20)}$$

where $[D^e]$ is elastic stress-strain matrix. From the equation (3.20) and (3.21), an equation of stress-strain relation is obtained as follows.[44]

$$\{\sigma\} = [D^e](\{\varepsilon^e\} - \{\varepsilon^T\}) \quad \text{Equation (3.21)}$$

Equilibrium equation of element can be expressed as follows.

$$[k]\{d\} = \{f_s\} + \{f_v\} + \{f_T\} \quad \text{Equation (3.22)}$$

where $[k]$: stiffness matrix of element, $\{f_s\}$: nodal force vector due to surface force, $\{f_v\}$: nodal force vector due to body force and $\{f_T\}$: pseudo nodal force vector due to thermal strain. These are consisted as bellows.

$$[k] = \int_{V^e} [B]^T [D^e][B] dV \{d\} \quad \text{Equation (3.23)}$$

$$\{f_s\} = \int_{S_\sigma^e} [N]^T \{\overline{T}\} dS \quad \text{Equation (3.24)}$$

$$\{f_v\} = \int_{V^e} [N]^T \{\overline{F}\} dV \quad \text{Equation (3.25)}$$

$$\{f_T\} = \int_{V^e} [B]^T [D^e]\{\varepsilon^T\} dV \quad \text{Equation (3.26)}$$

Equilibrium equation for the whole object, the total elements, is obtained to assemble the equation (3.22) for each element.

3.2.2 Elasto-plastic material behaviour

Elasto-plastic behaviour in the uniaxial testing is characterised by an initial elastic material response on to which a plastic deformation is superimposed after a certain level of stress has been reached as shown in Fig. 3.1. The material initially deforms according to the elastic modulus, E, until the stress level reaches a value σ_Y designated the uniaxial yield stress. On increasing the load further, the material is assumed to exhibit linear strain-hardening characterised by the tangential modulus, E_T.

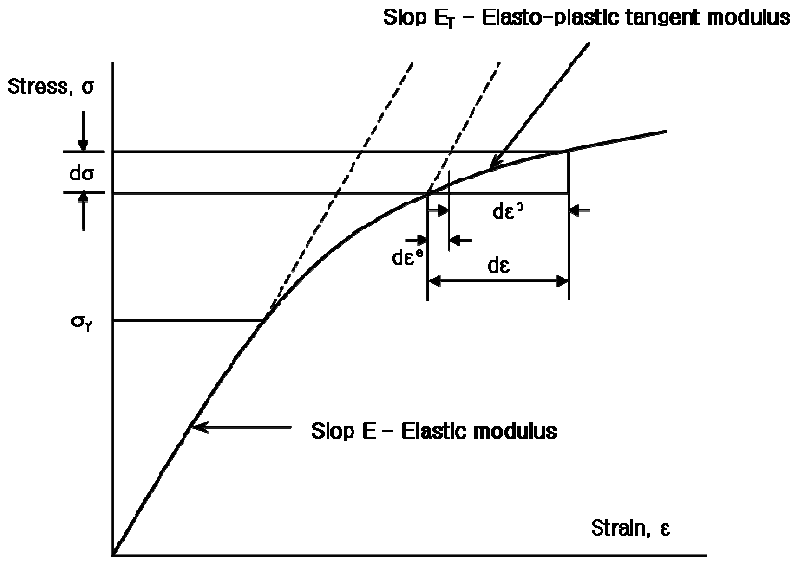

Fig 3.1 Elasto-plastic strain hardening behaviour for the uniaxial case

At some stage after initial yielding, consider a further load application resulting in an incremental increase of stress, $d\sigma$, accompanied by a change of strain, $d\varepsilon$. Assuming that the strain can be separated into elastic and plastic components, their relation are expressed as follows:

$$d\varepsilon = d\varepsilon^e + d\varepsilon^p \qquad \text{Equation (3.27)}$$

A strain-hardening parameter, H', is defined as

$$H' = \frac{d\sigma}{d\varepsilon^p}$$ Equation (3.28)

This can be interpreted as the slop of the strain-hardening portion of the stress-strain curve after removal of the elastic strain component. Thus

$$H' = \frac{d\sigma}{d\varepsilon - d\varepsilon^e} = \frac{E_T}{1 - E_T/E}$$ Equation (3.29)

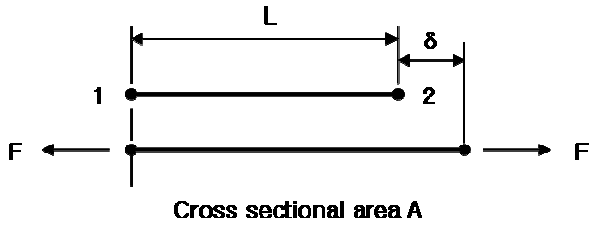

Fig. 3.2 Forces and displacement for a two-node element

With reference to Fig. 3.2, consider the behaviour of a linear displacement element, which has a cross sectional area *A*, when it is subjected to a gradually increasing axial force, *F*, which results in an extension, δ. Stiffness of material for the elastic material behaviour is expressed as follows:

$$K^e = \frac{F}{\delta} = \frac{EA}{L}$$ Equation (3.30)

Then the element stiffness matrix is simply

$$K^e(e) = \frac{EA}{L}\begin{bmatrix} 1 & -1 \\ -1 & 1 \end{bmatrix}$$ Equation (3.31)

Suppose *F* is increased until the material has yielded. Consider a further incremental increase in load *dF* which causes an additional element extension, $d\delta$. Then

$$d\delta = (d\varepsilon^e + d\varepsilon^p)L$$ Equation (3.32)

On use of equation (C.42)

$$dF = d\sigma A = AH'd\varepsilon^p$$ Equation (3.33)

The tangential stiffness for the material is given by

$$K^{ep} = \frac{dF}{d\delta} = \frac{AH'd\varepsilon^p}{L(d\sigma / E + d\varepsilon^p)}$$ Equation (3.34)

Or, using equation (3.34) and rearranging

$$K^{ep} = \frac{EA}{L}(1 - \frac{E}{E + H'})$$ Equation (3.35)

Finally, the element stiffness matrix for elasto-plastic material behaviour is expressed as follows:

$$K^{ep}(e) = \frac{EA}{L}(1 - \frac{E}{E + H'})\begin{bmatrix} 1 & -1 \\ -1 & 1 \end{bmatrix}$$ Equation (3.36)

In equation (3.36), the first term represents the elastic stiffness. The second term accounts for the reduction in stiffness from the elastic value due to yielding.

Chapter 4

Numerical Analysis on Friction Stir Welding

4.1 Introduction

Although FSW is a new welding technology, it has been extensively studied in both the academic and industrial communities experimentally and numerically for most aluminum alloys including difficult-to-weld alloys. This chapter includes the numerical simulation of the temperature and residual stress distribution in similar and dissimilar welded Al6061and AZ31B-H24 Alloys. In order to numerically calculate temperature and residual stress distribution in welds, finite element heat source model is developed on the basis of experiment results and characteristics of temperature and residual stress distribution in dissimilar welds are understood from the result of simulation. For the finite element stimulation of the heat transfer and residual stress analysis, to obtain a more general conclusion, cases with different process parameters are modeled, in the FSW, and also three models with different tool pin shape such as cylindrical shaped pin, frustum shaped pin and threaded pin were used. The thermal and residual stress distributions for the three types of pin configuration were simulated and results were compared. The geometric model dimension used for the numerical simulation is as shown in Fig 4.1.

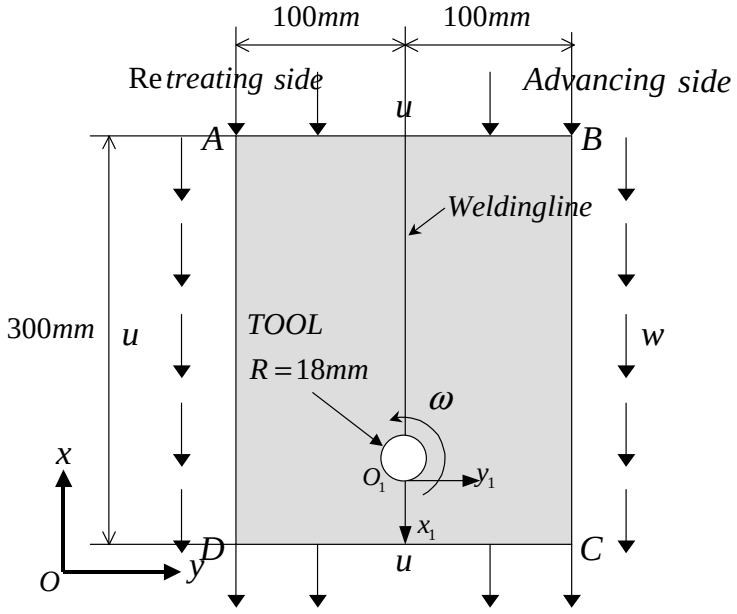

Fig.4.1 The geometry model and the boundary conditions of FSW

4.2 Materials and Modeling

4.2.1 Temperature dependency of Material properties

In this study, temperature dependent material properties has been considered in the numerical simulation for the analysis of heat conduction and thermal elasto-plasticity for Al6061-T6 and AZ31B-H24 alloy as shown in Table 4.1, 4.2 and Fig. 4.2, 4.3. Material is assumed as an isotropic.

Table 4.1 Physical properties of Al6061-T6 alloy for heat conduction analysis

Temperature (T), ˚C	Heat conductivity (λ), $\times 10^2$ W/m·K	Specific heat (c), $\times 4.19 \times 10^2$ J/kg·K	Density (ρ), $\times 10^3$ kg/m3
20	6.564	24.874	14.309
50	6.770	25.733	14.280
100	7.083	26.832	14.229
150	7.338	27.632	14.176
200	7.536	28.250	14.120
250	7.676	28.777	14.062
300	7.760	29.286	14.002
350	7.786	29.822	13.940
400	7.754	30.410	13.875
450	7.666	31.052	13.875
500	7.520	31.727	13.875

Table4.2 Physical properties of AZ31B Mg alloy for heat conduction analysis

Temperature (T), ˚C	Heat conductivity (λ), $\times 10^2$ W/m·K	Specific heat (c), $\times 4.19 \times 10^2$ J/kg·K	Density (ρ), $\times 10^3$ kg/m3
20	0.085	0.251	0.002
50	0.098	0.253	0.002
100	0.119	0.255	0.002
150	0.138	0.257	0.002
200	0.156	0.259	0.002
250	0.173	0.261	0.002
300	0.174	0.263	0.002
350	0.174	0.265	0.002
400	0.174	0.267	0.002
450	0.174	0.270	0.002
500	0.174	0.279	0.002
550	0.174	0.289	0.002
600	0.174	0.298	0.002

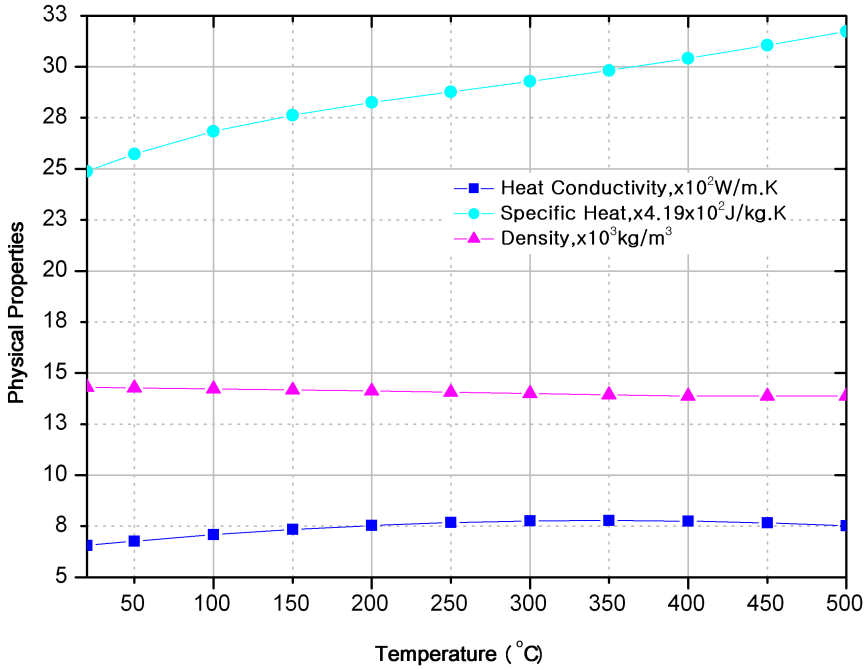

Fig.4.2 physical properties of Al606-T6 Alloy

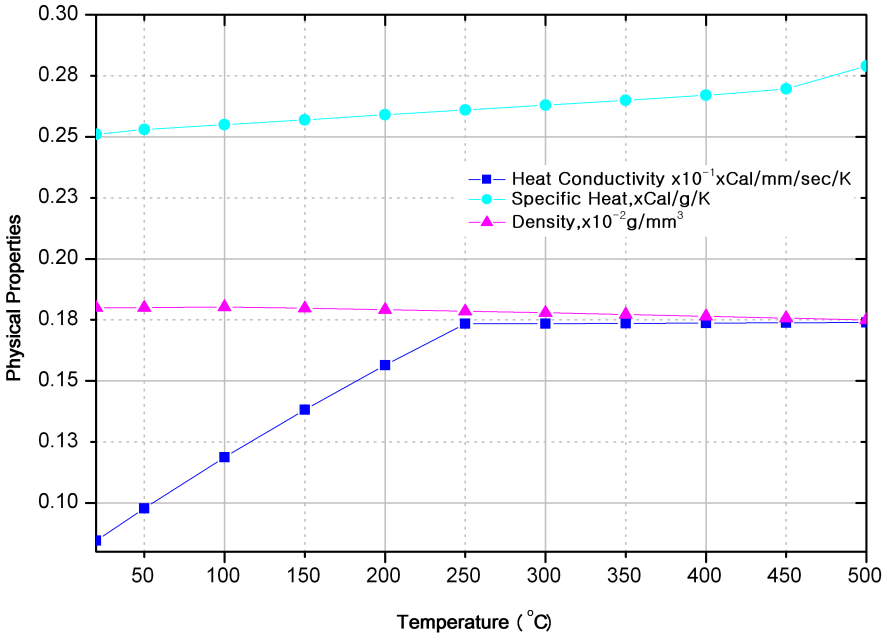

Fig.4.3 Physical properties of AZ31B Mg alloy

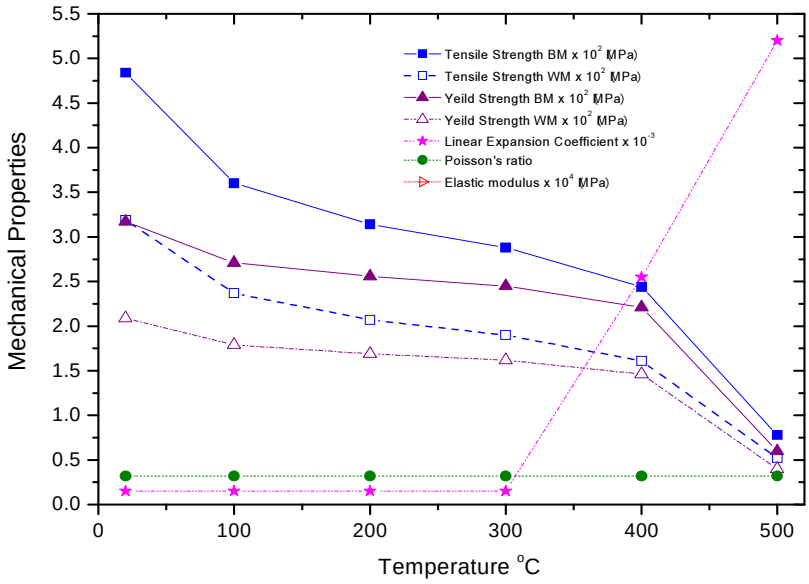

Fig. 4.4 Mechanical properties of Al606-T6 Alloy for thermal elasto-plastic analysis

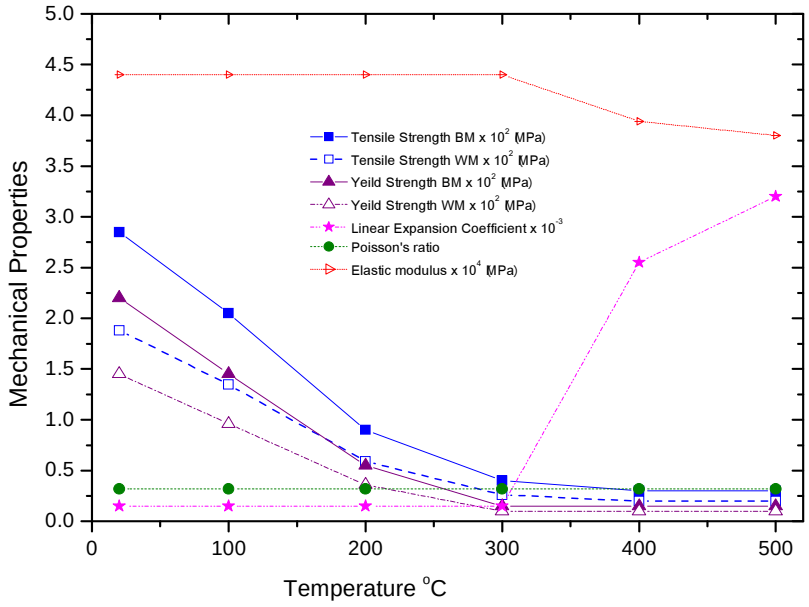

Fig. 4.5 Mechanical properties of AZ31B Mg alloy for thermal elasto-plastic analysis

4.2.2 Modeling details and Assumption

The heat-treatable alloy Al 6061-T6 with Al-Mg-Si grade and AZ31B-H24 Mg alloy are used as the test specimen in this study. Al 6061-T6 with Al-Mg-Si has a good tear resistance, tolerance and weldability are not a difficult matter regarding to the recent fusion welding technology. Magnesium and its alloys have been widely used in various fields as they are the lightest structural metals, and they possess excellent properties such as high specific strength, low density, good and economical process ability with cast technology, and high recycling potential. AZ31B alloy is an all-purpose wrought alloy with good strength and ductility. H24 condition refers to strain hardening and partial annealing (recrystallization with no grain growth).

The model for a thermal distribution and residual stress of numerical analysis have a Cartesian coordination system X-axis along welding line, Y-axis transverse to welding line and Z-axis along thickness direction, and this model has a dimension of length (L): 300mm, breath (B): 200mm and thickness (T): 4mm, and welding condition shown in Table 4.3.

Table 4.3 Experiment condition of friction stir welding for butt joint

	Rotation Speed (rpm)	Welding speed (mm/min)	Shoulder size (mm)	Pin size (mm)
Al 6061-T6	1000,1500,2000	200	18	6
AZ31B-H24	1000,2000	100	18	6
Al 6061-T6/ AZ31B-H24	450	15	18	6

The two-dimensional unstationary heat conduction theory considering the thermal dependence according to a thermal change of material has been adapted for the analysis of heat distribution characteristics around the weld-bond of FSW, which is idealized as 4-node isoperimetric F.E.M model. The material properties of the BM, HAZ, TMAZ, SZ were temperature and temperature-history dependent. The temperature-dependent mechanical material properties considered for Al 6061-T6 with Al-Mg-Si grade and AZ31B-H24 Mg alloy are shown in Fig.4.4 and Fig.4.5, respectively. Except for the values of the convection heat transfer coefficient, which were taken ASM handbook.. The amount of heat input was found as the product of rotating speed, traveling speed, friction coefficient In the numerical simulation of the FSW for Al6061-T6 and AZ31B alloys, it is assumed that the two plates are welded non-symmetrically during welding and after welding. The FEA mesh is shown in Fig.4.7 has 4 noded quadrilateral elements with 8200 elements and 8631 nodes, which is used for both the heat transfer analysis and the residual stress analysis.

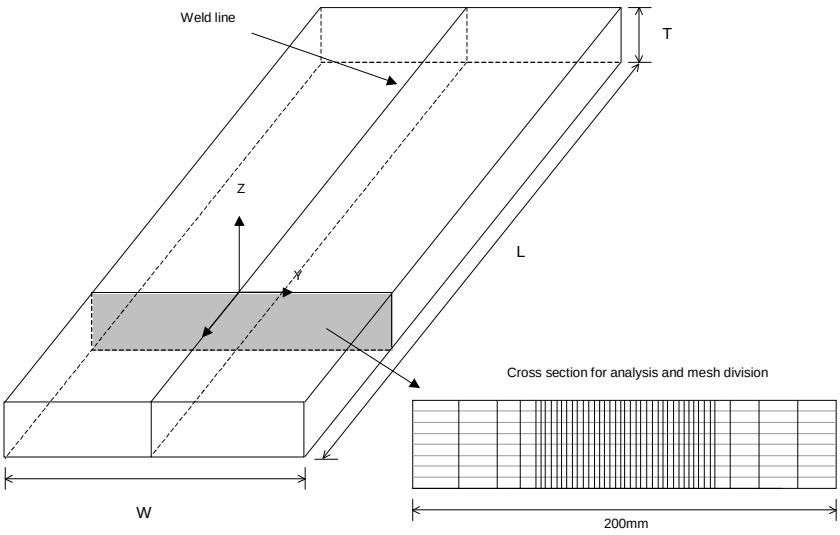

Fig. 4.6 Two-dimensional model for finite element analysis

The smallest element used in the FEA model is in the weld region and has the dimension of 0.2mm × 0.2mm because the elements along the probe/matrix interface are the principle element of heat generation during simulation, and The welding area regarded having the largest effects is meshed as shown the Fig 4.6 with considering tool shoulder and diameter of pin. Since the fixture of clamped steel strips is released after the weld cools down to the room temperature, the residual stress in the weld will be redistributed after the fixture release.

In this study, two-dimensional FE analysis is conducted to the quasi-state condition to avoid the cost of a full three-dimensional FE analysis because it is verified from the established research result that heat flow in the longitudinal direction is negligible [45]. Hence, heat flow is restricted to a y-z plane as shown in Fig. 4.8. This has been shown to cause little error except for low speed high heat input welds.

Finite element analysis program developed in the Joining and Manufacturing Laboratory, Chosun Univ. has been used to solve the heat conduction and thermal elasto-plastic problem. Heat flux for heat input element is calculated as explained in Chapter 2 in Equation (2.3). And in the thermal-elastic-plastic analysis of FSW welded zone thermal history obtained from the heat transfer analysis has been used as input data. The boundary condition of thermal elasticity is considered at the time of shrinkage, expansion and the developing of manufacturing. The boundary condition for heat conduction and thermal elasto-plastic analysis is shown in Fig. 4.7.

In order to verify the validity of heat source model and calculate the temperature distribution in welds, heat conduction analysis was conducted for butt joint condition in cylindrical pin, Frustum

pin and Threaded pin of FSW process respectively.
The following assumptions are made in the model:

- The heat generated at the tool shoulder/workpiece interface, frictional heat
- No heat flows into the workpiece if the local temperature reaches the material melting temperature.
- No tilting
- Heat transfer to the support table is ignored

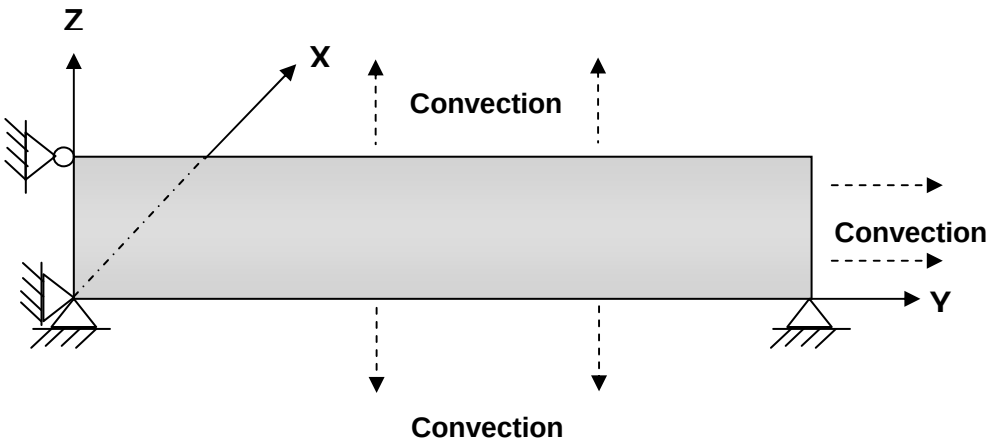

Fig. 4.7 Boundary conditions for heat conduction and thermal elasto-plastic analysis

The thermal and residual stress distributions for the three types of pin configuration were simulated and results were compared. The pin shapes considered are cylindrical pin (1), Threaded pin (2), Frustum pin (3) and the details of the pin are given in the Table 4.4.

Table 4.4 Dimensions of tool pin

Pin shape	Shoulder dia. (mm)	Pin dia. (mm)	Pitch length (mm)
Cylindrical pin	18	6	0
Threaded pin	18	6	1
Frustum pin	18	6	0

4.2.2.1 Cylindrical pin

The welding parameters used for the simulation of the cylindrical pin are as given in the Table 4.5

Table 4.5 Simulation condition for Cylindrical pin

	Rotating speed (rpm)	Welding speed (mm/min)	Heat transfer efficiency (η fsw)
Al6061-T6	1000	200	85 %
AZ31B-H24	2000	100	90 %

The welding schematics and the 2D-mesh details for the cylindrical pin are shown in the Fig 4.8. The mesh size near the pin is made fine and courser away from the pin. The mesh width varies from 0.2mm near the pin boundary to 2mm away from the pin. The diameter of the cylindrical pin is about 6mm and shoulder diameter of 18mm and pin height of 3.6 mm.

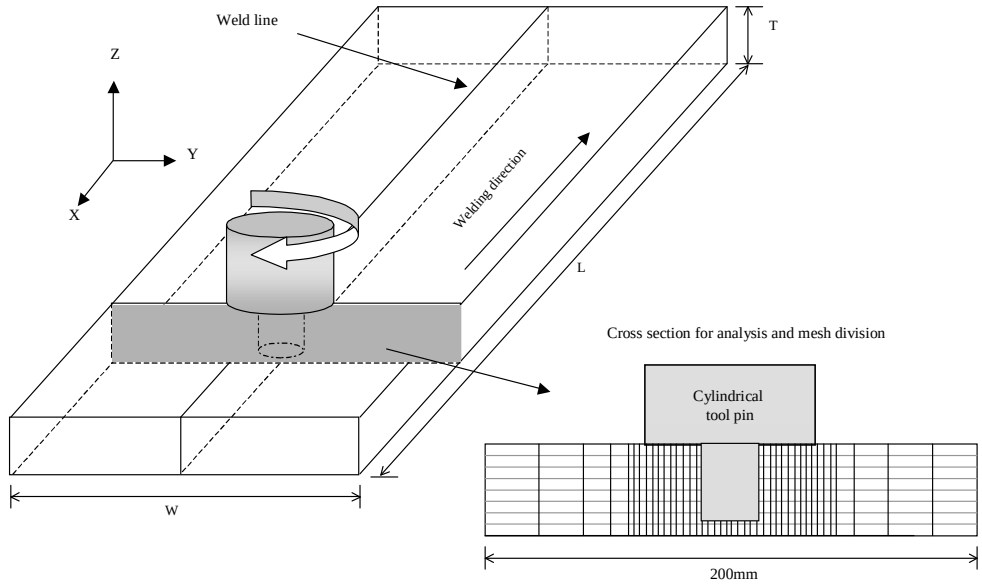

Fig. 4.8 Simulation objects and coordinates system for cylindrical pin

4.2.2.2 Frustum pin

The welding parameters used for the simulation of the frustum pin are as given in the Table 4.6

Table 4.6 Simulation condition for frustum pin

	Rotating speed (rpm)	Welding speed (mm/min)	Heat transfer efficiency (η_{fsw})
Al6061-T6	1000	200	90 %
AZ31B-H24	2000	100	90 %

The welding schematics and the 2D-mesh details for the frustum pin are shown in the Fig 4.9. The mesh size near the pin is made fine and courser away from the pin. The mesh width varies from 0.2mm near the pin boundary to 2mm away from the pin. The diameter of the threaded pin is about 6mm, tread width 1mm, thread pitch 1mm and shoulder diameter of 18mm and pin height of 3.6mm.

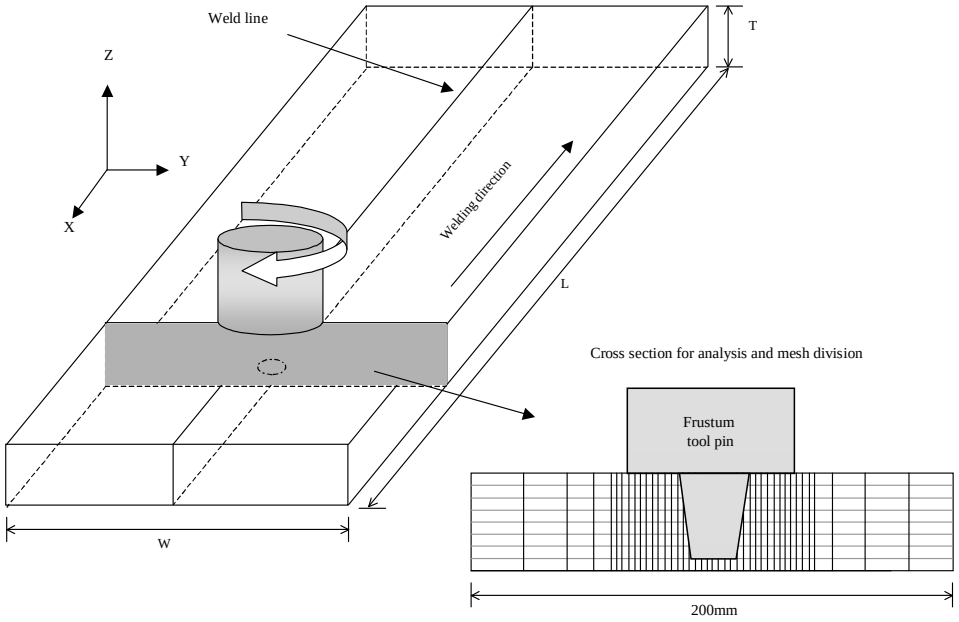

Fig. 4.9 Simulation objects and coordinates system for Frustum pin

4.2.2.3 Threaded pin

The welding parameters used for the simulation of the Threaded pin are as given in the Table 4.7.

Table 4.7 Simulation condition for Threaded pin

	Rotating speed (rpm)	Welding speed (mm/min)	Heat transfer efficiency (η_{fsw})
Al6061-T6	1000	200	95 %
AZ31B-H24	2000	100	90 %

The welding schematics and the 2D-mesh details for the Threaded pin are shown in the Fig 4.10. The mesh size near the pin is made fine and courser away from the pin. The mesh width varies from 0.2mm near the pin boundary to 2mm away from the pin. The diameter of the threaded pin is about 6mm, thread width 1mm, thread pitch 1mm and shoulder diameter of 18mm and pin height of 3.6mm.

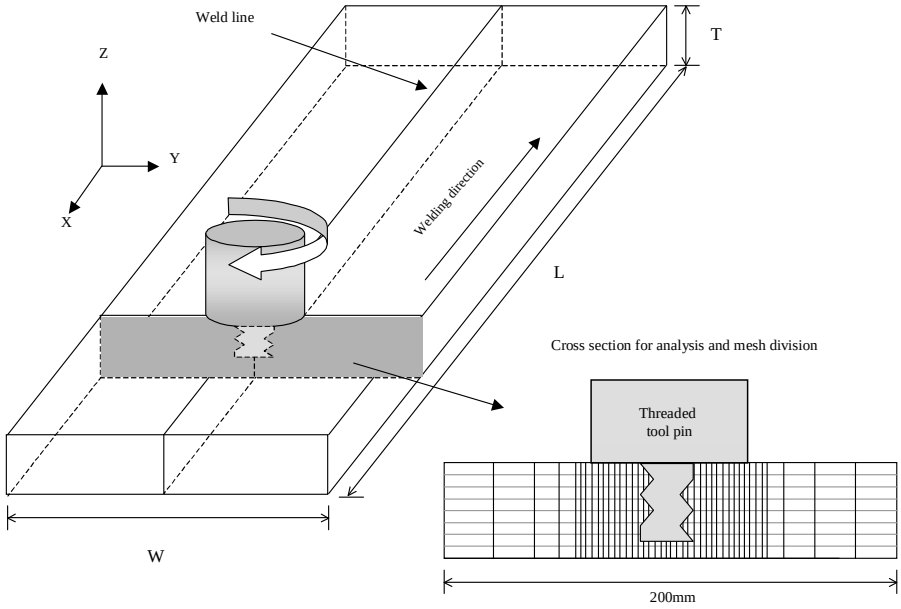

Fig. 4.10 Simulation objects and coordinates system for threaded pin

4.3 Heat Conduction Analysis

4.3.1 Heat Conduction of A6061-T6 alloy

Principal dimension of the model for the analysis are given in Fig.4.1, (L=300mm, B=200mm, T=4mm) respectively. X, Y and Z indicate the weld line direction, width direction and thickness direction respectively in the analysis model. Friction stir welds was executed, beginning with a low travel speed, to establish the sound welds, and welds were made in the square groove butt joints. These welds judged the surface appearance of friction stir welds. The material for analysis is Al 6061-T6 alloy and its Chemical composition and Mechanical properties are given in Table 4.8

Table 4.8 Chemical compositions and Mechanical properties of Al6061-T6 alloy

Chemical compositions (wt %)			
Al	Fe	Si	Cr
98	0.7	0.4-0.8	0.04-0.35
Mg	Cu	Mn	Zn
0.8-1.2	0.15-0.4	0.15	0.25
Mechanical properties			
Yield strength	Elongation (%)	Tensile stress	
55(MPa)	25	240(MPa)	
Density (g/cc)	Heat conduction coeff.	Elastic modulus	
2.7	0.40	70.70(MPa)	

In this study, an integrated thermal elasto- plastic model was used to study the formation of temperature distributions and the residual stress distributions of Al6061-T6 friction stir welds. The joining of specimen is implemented under the condition that is the rotational speed (1000rpm), travel speed (200mm/min).

The simulations were conducted using a 2-dimensional model, accounting for the frictional heating. Temperature-dependent material properties were also considered in the finite element model. In addition, the residual stress fields of friction stir welds made under different welding speeds were measured using electrical-resistance strain gauges.

The limitation of the PC computing power makes a thermo-mechanical finite element analysis of FSW impractical. To compensate the lack of a predicted temperature field, actual temperature values from practical FSW test [18] were used to construct an approximate temperature field for the FSW process simulation. In this test, first Al6061-T6 is considered, the rotational speed of the pin is 1000 rpm and the travel speed of 100 mm/min. The maximum temperature created by FSW ranges from 80 to 90% of the melting temperature of the welding material [2]. Table 4.9 shows friction stir-welding conditions of Al6061-T6 alloy and Table 4.10 shows input data for the calculation of Al6061-T6 alloy.

Table 4.9 Friction stir welding Conditions of Al6061-T6 alloy

Parameter	Conditions
Rotation speed	1000 (rpm)
Welding speed	200 (mm/min)
Shoulder (D)	18 mm
Pin (D)	6 mm
Friction Coeff.	0.42
Welding method	Butt

Table 4.10 Input data for the calculation of Al6061-T6 alloy

Parameter	Conditions
Density	2700 g/m^3
Heat conductivity	167 W/m K
Coefficient of friction	0.45
Rotation speed	1000 rpm
Welding speed	200 mm/min

In order to verify the validity of heat source model and calculate the temperature distribution in welds, heat conduction analysis was conducted for butt joint condition in Cylindrical pin, Threaded pin and Frustum pin of FSW process respectively. Table 4.11 shows Simulation conditions for FSW and Table 4.12 shows heat input of Al 6061-T6 (1000rpm, 200mm/min) according to the pin shape.

Table 4.11 Simulation conditions for FSW according to the tool pin shape

Materials	Tool pin shape	Rotating speed (rpm)	Traveling speed (mm/min)	Heat transfer Efficiency (η fsw)
Al6061-T6	Cylindrical pin	1000	200	85%
	Frustum pin	1000	200	90%
	Threaded pin	1000	200	95%

Table 4.12 Heat input of Al 6061-T6 alloy FSWelding(1000rpm, 200mm/min)

Tool pin shape	$q_{shoulder}$ (cal/mm)		q_{pin} (cal/mm)		Heat transfer Efficiency (η fsw)	Friction coefficient
	q_{as}	q_{ap}	q_{rs}	q_{rp}		
Cylindrical pin	5.56	1.55	5.00	1.40	85%	0.45
Frustum pin	5.37	1.50	4.83	1.35	90%	0.45
Threaded pin	5.56	2.48	5.01	2.23	95%	0.45

$q_{shoulder}$: Heat input of tool shoulder

q_{pin} : Heat input of tool pin

q_{as} : Heat input of tool shoulder on advancing side

q_{ap} : Heat input of tool pin on advancing side

q_{rs} : Heat input of tool shoulder on retreating side

q_{rp} : Heat input of tool pin on retreating side

η fsw: Heat transfer efficiency

For the thermal analysis the calculated heat input has been used as input data to model the heat source. The heat source is modeled as a prescribed surface flux under the shoulder of the tool, and as a volumetric heat source in the pin. The heat losses in the plate are due to conduction into the backing plate, and convection to the air at the free surfaces. The reference room temperature has been taken, as 20 °C and contact conductibility as temperature dependent. The mechanical model simulates the material behavior due to the combination of the thermal strains and the tool pressure.

The aluminum plate is modeled with an elastic plastic material model. This material model uses the Von-Mises yield criterion and does not incorporate hardening. The Young's modulus and yield stress are temperature dependent.

4.3.1.1 Temperature Distributions of Cylindrical pin

The numerical simulation has been considered using two-dimension unstationary heat conduction program. Simulation conditions for Al6061-T6 for the tool pin shape are given in Fig. 4.9 and Table 4.5. Temperature distribution in WM, HAZ, TMAZ and SZ was calculated as shown in Fig. 4.11.

The numerical simulation has been conducted using two-dimensional unstationary heat conduction program. The maximum temperature was formed at the base metal surface contacting with tool shoulder of advancing side as shown in Fig 4.12(b), which indicates the frictional heat generated between tool shoulder and base metal surface was the most significant heat source in the process. The welding formed at about 440℃ with the aid of plastic flow, that is lower than melting temperature (660℃) of aluminum. The maximum temperature in the retreating side was about 410℃ as shown in Fig 4.12(a).

The Fig.4.13 shows the temperature history of Stir Zone (SZ), Base Metal (BM), Heat Affected Zone (HAZ) and Thermo-Mechanically Affected Zone (TMAZ) along the line 1mm below the crown in advancing side and retreating side. The heights temperature (below the melting temperature) appears after 2sec., and it rapidly cooled out. It has been noticed that the temperature gradient is equalized after 12sec. and the weld part is rapidly cooled through the heat conduction analysis. The elements are sampled similar to that of test specimen such that, measure points were taken at 4.0mm (SZ), 6.6mm (TMAZ), 9.2mm (HAZ) and 11.4mm (BM) from the weld line.

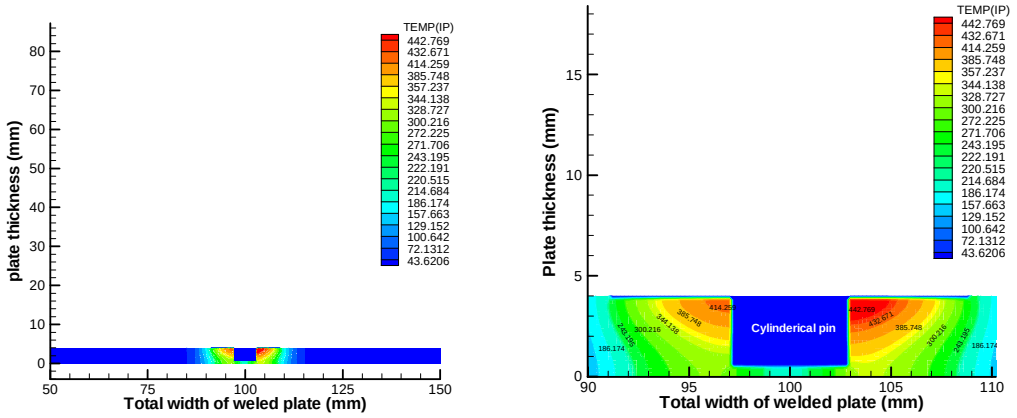

(a) Full scaled contour (b) Magnified contour

Fig. 4.11 Calculated temperatures distribution according to the Cylindrical pin using isothermal contour in FSWelded

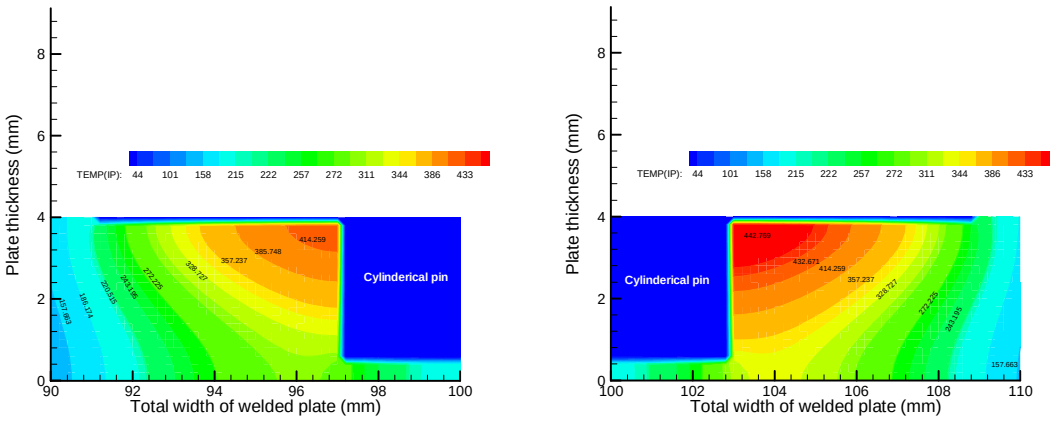

(a) Retreating side (b) Advancing side

Fig. 4.12 Calculated temperature distributions according to the Cylindrical pin using isothermal contour in FSWelded

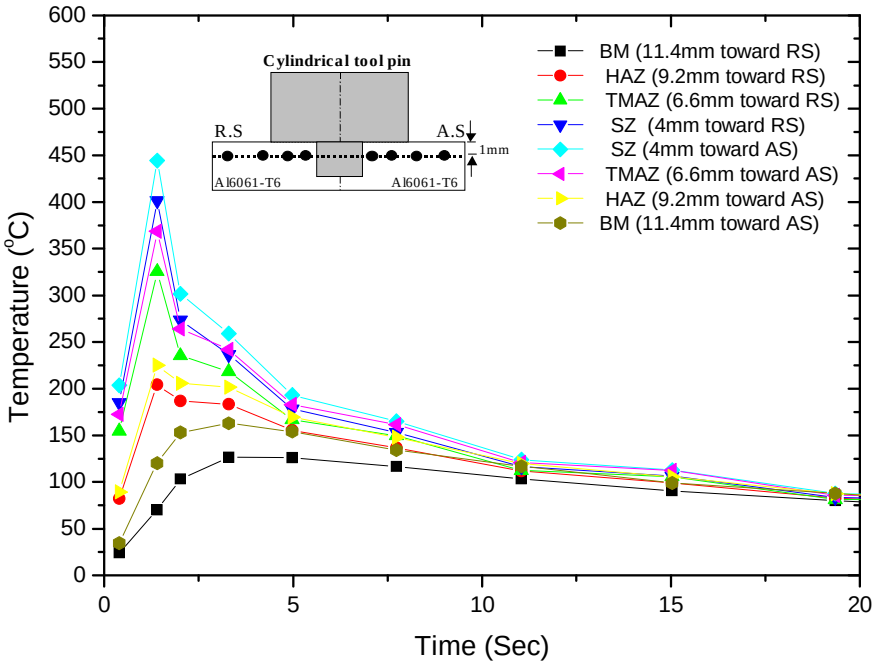

Fig. 4.13 Calculated temperature distributions according to the time variation according to the Cylindrical pin (Al6061-T6)

4.3.1.2 Temperature Distributions for Frustum pin

Temperature distribution in WM, HAZ, TMAZ and SZ was calculated as shown in Fig. 4.14. The maximum temperature of advancing side as shown in Fig 4.15(b), is about 448℃. The maximum temperature in the retreating side was about 396℃ as shown in Fig 4.15(a). The Fig.4.16 shows the temperature history of Stir Zone (SZ), Base Metal (BM), Heat Affected Zone (HAZ) and Thermo-Mechanically Affected Zone (TMAZ) along the line 1mm below the crown in advancing side and retreating side. The heights temperature (below the melting temperature) appears after 2.25sec., and it rapidly cooled out. It has been noticed that the temperature gradient is equalized after 15sec. and the weld part is rapidly cooled through the heat conduction analysis.

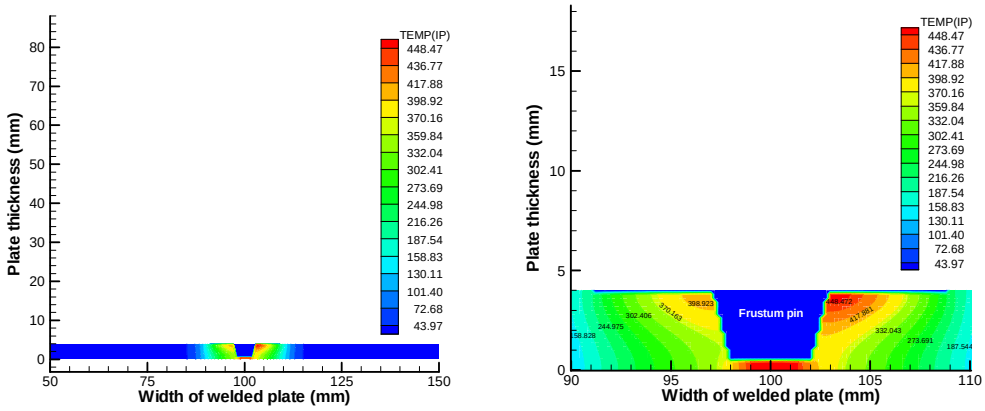

(a) Full scaled contour (b) Magnified contour

Fig. 4.14 Calculated temperature distributions according to the Frustum pin using isothermal contour in FSWelded

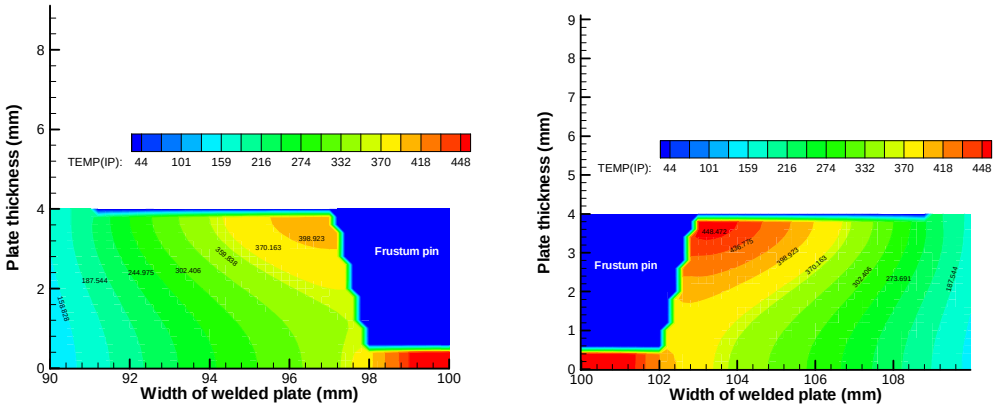

(a) Retreating side (b) Advancing side

Fig. 4.15 Calculated temperature distributions according to the Frustum pin using isothermal contour in FSWelded

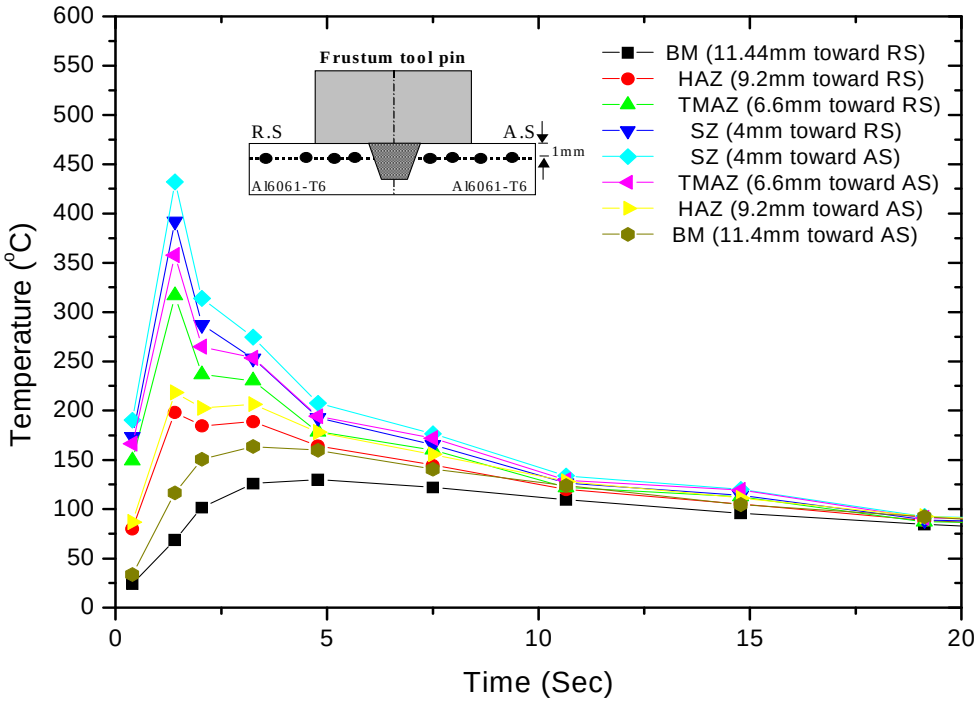

Fig. 4.16 Calculated temperature distributions according to the time variation according to the Frustum pin (Al6061-T6)

4.3.1.3 Temperature Distributions of Threaded pin

The maximum temperature of advancing side as shown in Fig 4.17(b), is about 441℃. The maximum temperature in the retreating side was about 417℃ as shown in Fig 4.17(a). The Fig.4.18 shows the temperature history of Stir Zone (SZ), Base Metal (BM), Heat Affected Zone (HAZ) and Thermo-Mechanically Affected Zone (TMAZ) along the line 1mm below the crown in advancing side and retreating side. The heights temperature (below the melting temperature) appears after 2.35sec., and it rapidly cooled out. It has been noticed that the temperature gradient is equalized after 20sec. and the weld part is rapidly cooled through the heat conduction analysis.

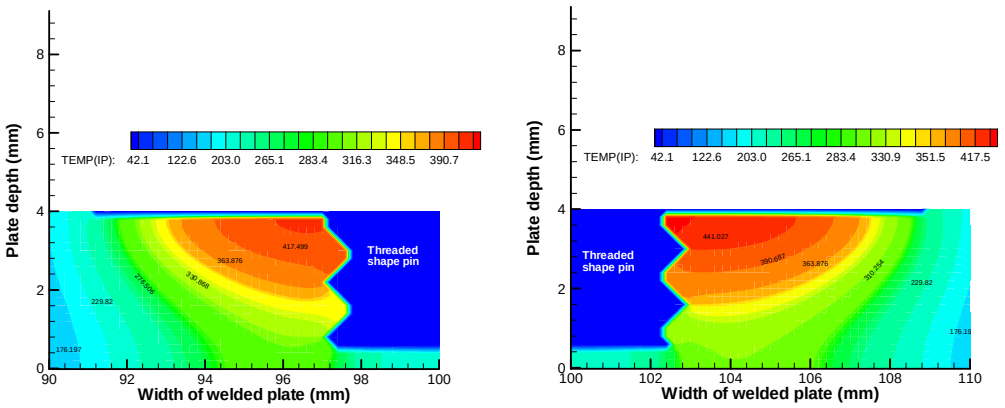

(a) Retreating side (b) Advancing side

Fig. 4.17 Calculated temperature distributions according to the Threaded pin using isothermal contour in FSWelded

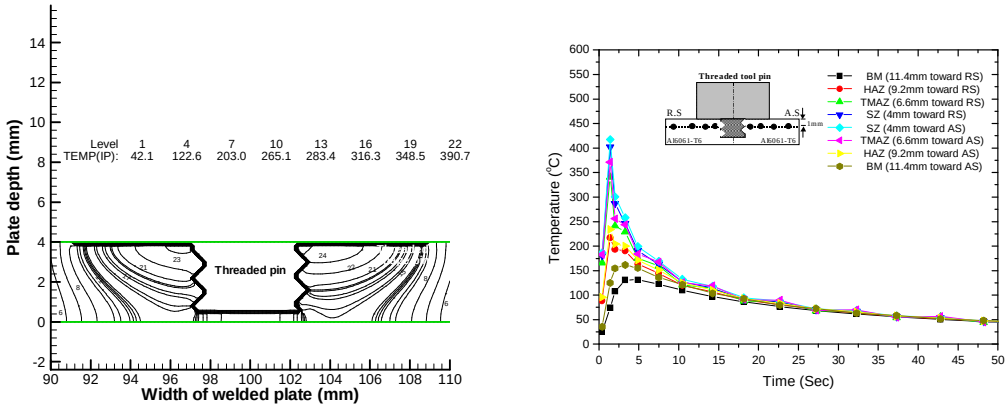

Fig. 4.18 Calculated temperature distributions according to the time variation according to the Threaded pin (Al6061-T6)

4.3.2 Heat Conduction of AZ31B-H24 Mg alloy

Principal dimension of the model for the analysis are given in Fig.4.1, (L=300mm, B=200mm, T=4mm) respectively. X, Y and Z indicate the weld line direction, width direction and thickness direction respectively of the analysis model. Friction stir welds was executed, beginning with a low travel speed, to establish the sound welds, and welds were made in the square groove butt joints. These welds judged the surface appearance of friction stir welds. The material for this analysis was AZ31B- Mg Alloy, and its Chemical composition and Mechanical properties are given in Table 4.13. Table 4.14 and Table 4.15 show welding conditions and heat input of AZ31B-H24 (2000rpm, 100mm/min) according to the pin shape.

Table 4.13 Chemical compositions and Mechanical properties of AZ31B- Mg Alloy

Chemical compositions (wt%)			
Al	Zn	Mn	Si
3.00	1.0	0.20	0.05
Cu	Ni	Fe	Mg
0.05	0.005	0.005	Bal.
Mechanical properties			
Elastic modulus	Mechanical strength	Yield strength	
45(MPa)	290(MPa)	220(MPa)	
Elongation (%)	Hardness (HR(c))		
15	73		

Table 4.14 Friction stir welding Conditions of AZ31B- Mg Alloy

Parameter	Conditions
Rotation speed	2000 (rpm)
Welding speed	100 (mm/min)
Shoulder (D)	18 mm
Pin (D)	6 mm
Friction Coeff.	0.42
Welding method	Butt

Table 4.15 Input data for the calculation of AZ31B- Mg Alloy

Parameter	Conditions
Density	2700 g/m^3
Heat conductivity	167 W/m K
Coefficient of friction	0.20
Rotation speed	2000 rpm
Welding speed	100 mm/min

In order to verify the validity of heat source model and calculate the temperature distribution in welds, heat conduction analysis was conducted for butt joint condition in Cylindrical pin, Threaded pin and Frustum pin of FSW process respectively. Table 4.16 shows Simulation conditions for FSW and Table 4.17 shows heat input of AZ31B- Mg Alloy (2000rpm, 100mm/min) according to the pin shape.

Table 4.16 Simulation conditions for FSW according to the tool pin shape

Materials	Tool pin shape	Rotating speed (rpm)	Traveling speed (mm/min)	Heat transfer Efficiency (η fsw)
AZ31B- Mg Alloy	Cylindrical pin	2000	100	90%
	Frustum pin	2000	100	90%
	Threaded pin	2000	100	90%

Table 4.17 Heat input of AZ31B-H24 alloy according to the tool pin shape (2000rpm, 100mm/min)

	$q_{shoulder}$ (cal/mm)		q_{pin} (cal/mm)		Heat transfer efficiency (η fsw)	Friction coefficient
	q_{as}	q_{ap}	q_{rs}	q_{rp}		
Cylindrical pin	4.94	1.38	4.45	1.24	90%	0.20
Frustum pin	4.78	1.33	4.30	1.20	90%	0.20
Threaded pin	4.94	2.21	4.45	1.99	90%	0.20

$q_{shoulder}$: Heat input of tool shoulder

q_{pin} : Heat input of tool pin

q_{as} : Heat input of tool shoulder on advancing side

q_{ap} : Heat input of tool pin on advancing side

q_{rs} : Heat input of tool shoulder on retreating side

q_{rp} : Heat input of tool pin on retreating side

η fsw: Heat transfer efficiency

4.3.2.1 Temperature Distributions of Cylindrical pin

In the case of the AZ31B-H24 for rotation speed of 2000rpm and travel speed of 100mm/min the temperature distribution is obtained as shown in the Fig 4.19. The maximum temperature of advancing side obtained as shown in Fig 4.20(b) is about 478℃. The maximum temperature in the retreating side was about 440℃ as shown in Fig 4.20(a). The Fig.4.21 shows the temperature history of Stir Zone (SZ), Base Metal (BM), Heat Affected Zone (HAZ) and Thermo-Mechanically Affected Zone (TMAZ) along the line 1mm below the crown in advancing side and retreating side. The heights temperature (below the melting temperature) appears after 2.25sec., and it rapidly cooled out. It has been noticed that the temperature gradient is fluctuating after 20sec. and the weld part is rapidly cooled through the heat conduction analysis.

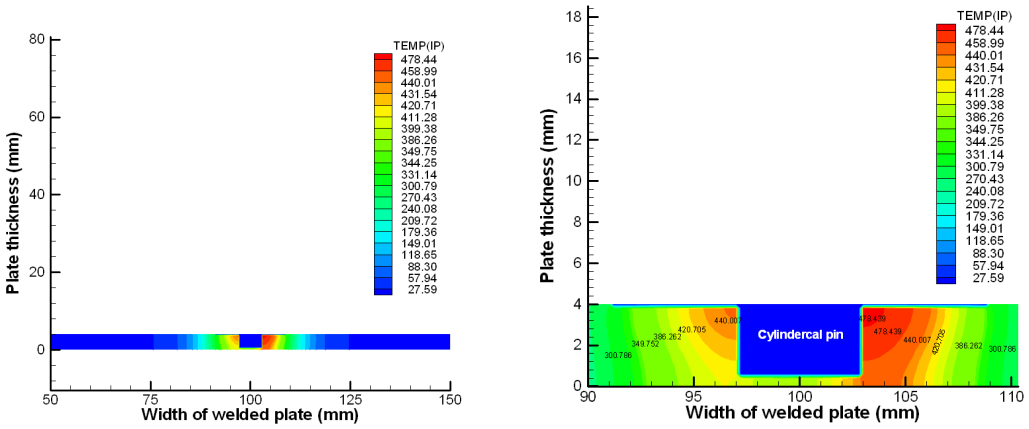

(a) Full scaled contour (b) Magnified contour

Fig. 4.19 Calculated temperature distributions according to the Cylindrical pin using isothermal contour in FSWelded

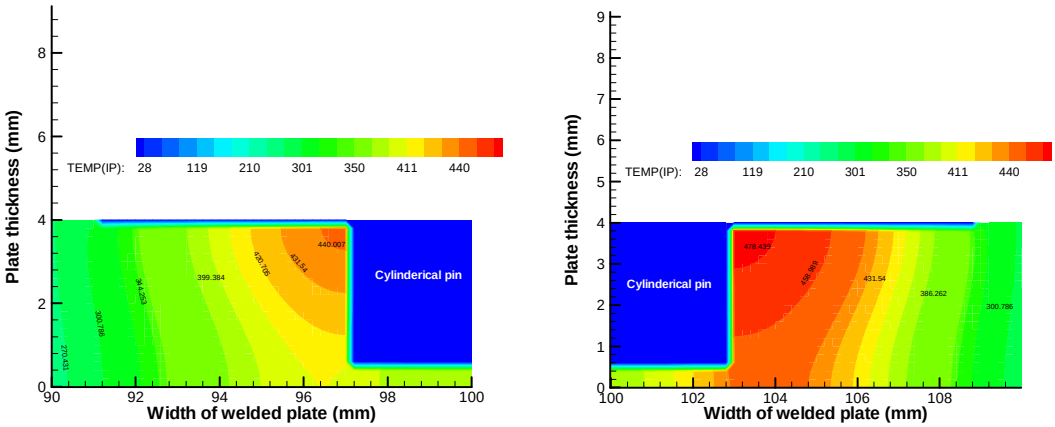

(a) Retreating side (b) Advancing side

Fig. 4.20 Calculated temperature distribution according to the Cylindrical pin using isothermal contour in FSWelded

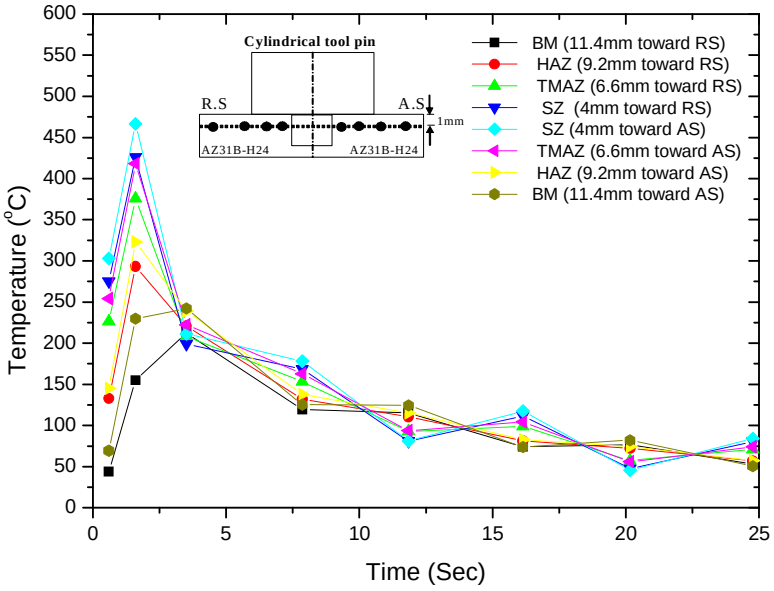

Fig. 4.21 Calculated temperature distributions according to the time variation according to the Cylindrical pin (AZ31B-H24)

4.3.2.2 Temperature Distributions of Frustum pin

In the case of the frustum pin the maximum temperature of advancing side obtained as shown in Fig 4.22(b) is about 474℃. The maximum temperature in the retreating side was about 442℃ as shown in Fig 4.23(a). The Fig.4.24 shows the temperature history of Stir Zone (SZ), Base Metal (BM), Heat Affected Zone (HAZ) and Thermo-Mechanically Affected Zone (TMAZ) along the line 1mm below the crown in advancing side and retreating side. The heights temperature (below the melting temperature) appears after 2.35sec., and it rapidly cooled out. It has been noticed that the temperature gradient is fluctuating after 10sec. and the weld part is rapidly cooled through the heat conduction analysis.

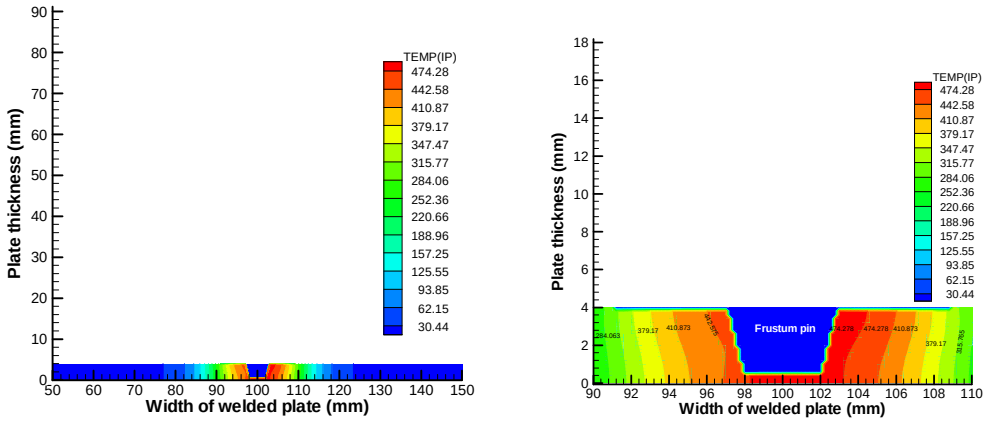

(a) Full scaled contour (b) Magnified contour

Fig. 4.22 Calculated temperature distributions according to the Frustum pin using isothermal contour in FSWelded

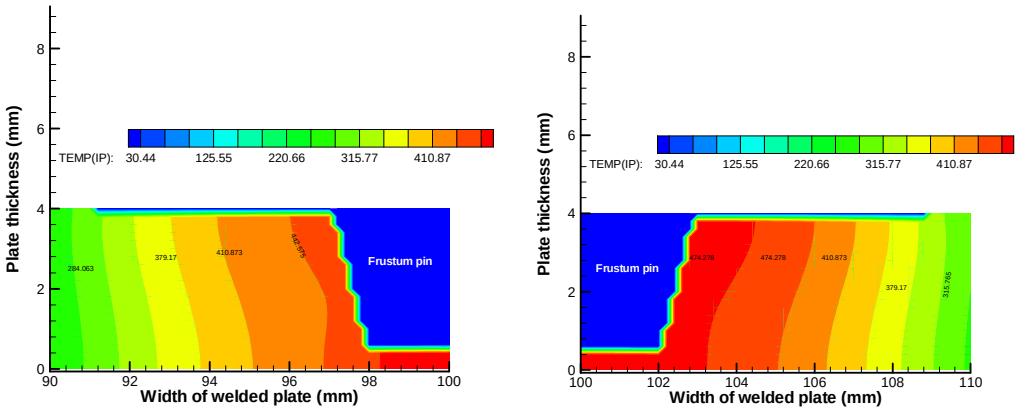

(a) Retreating side (b) Advancing side

Fig. 4.23 Calculated temperature distributions according to the Frustum pin using isothermal contour in FSWelded

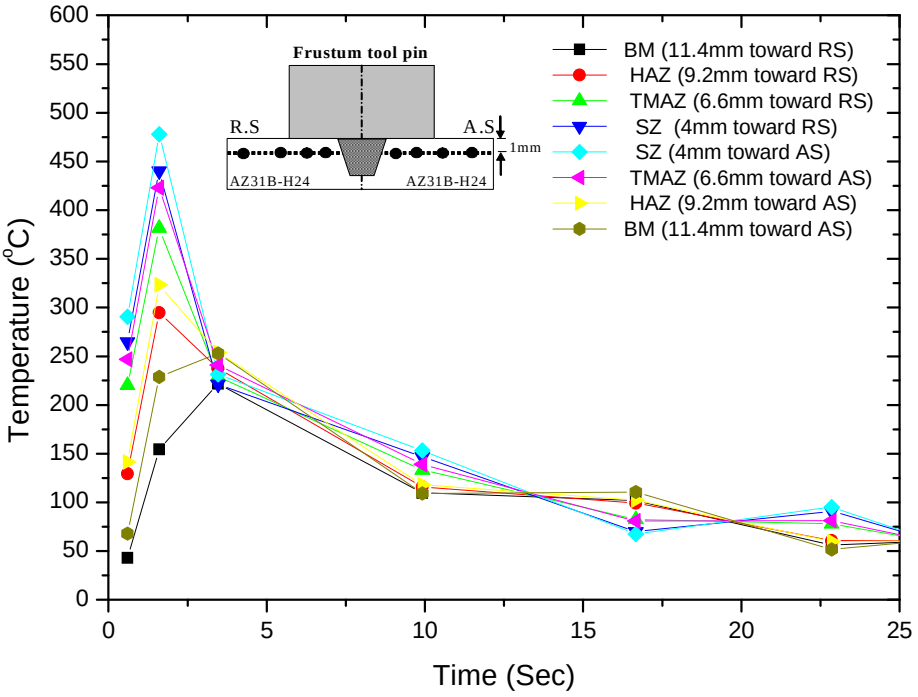

Fig. 4.24 Calculated temperature distributions according to the time variation according to the Frustum pin (AZ31B-H24)

4.3.2.3 Temperature Distributions of Threaded pin

In the case of the Threaded pin the maximum temperature of advancing side obtained as shown in Fig 4.26(b) is about 465℃. The maximum temperature in the retreating side was about 440℃ as shown in Fig 4.26(a). The Fig.4.27 shows the temperature history of Stir Zone (SZ), Base Metal (BM), Heat Affected Zone (HAZ) and Thermo-Mechanically Affected Zone (TMAZ) along the line 1mm below the crown in advancing side and retreating side. The heights temperature (below the melting temperature) appears after 2.45sec., and it rapidly cooled out. It has been noticed that the temperature gradient is fluctuating after 15sec. and the weld part is rapidly cooled through the heat conduction analysis.

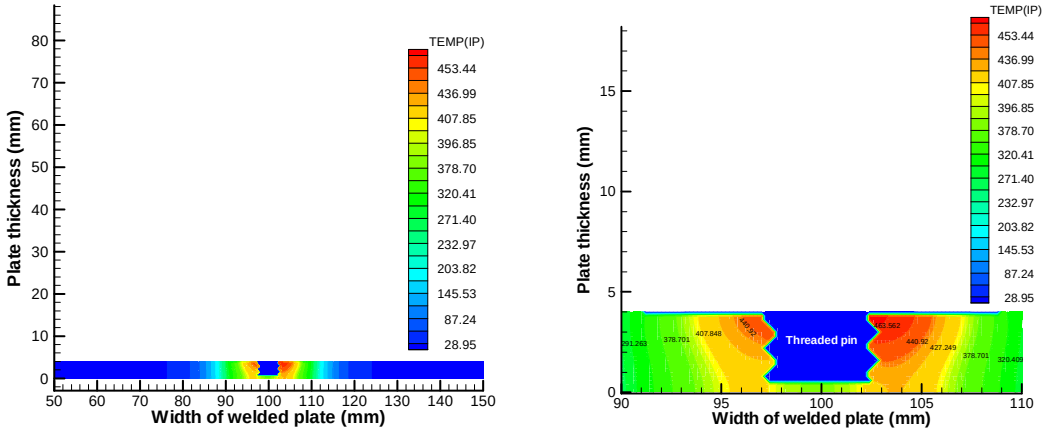

(a) Full scaled contour (b) Magnified contour

Fig. 4.25 Calculated temperature distributions according to the Threaded pin using isothermal contour in FSWelded

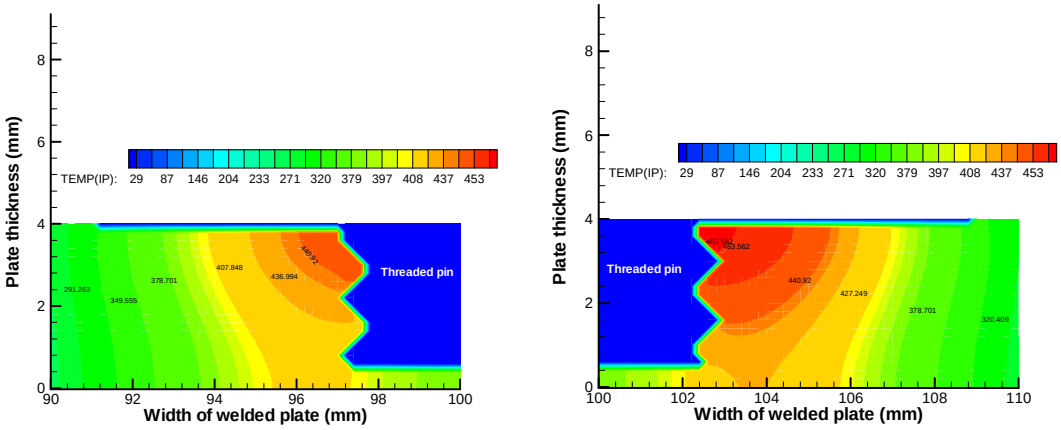

(a) Retreating side (b) Advancing side

Fig. 4.26 Calculated temperature distributions according to the Threaded pin using isothermal contour in FSWelded

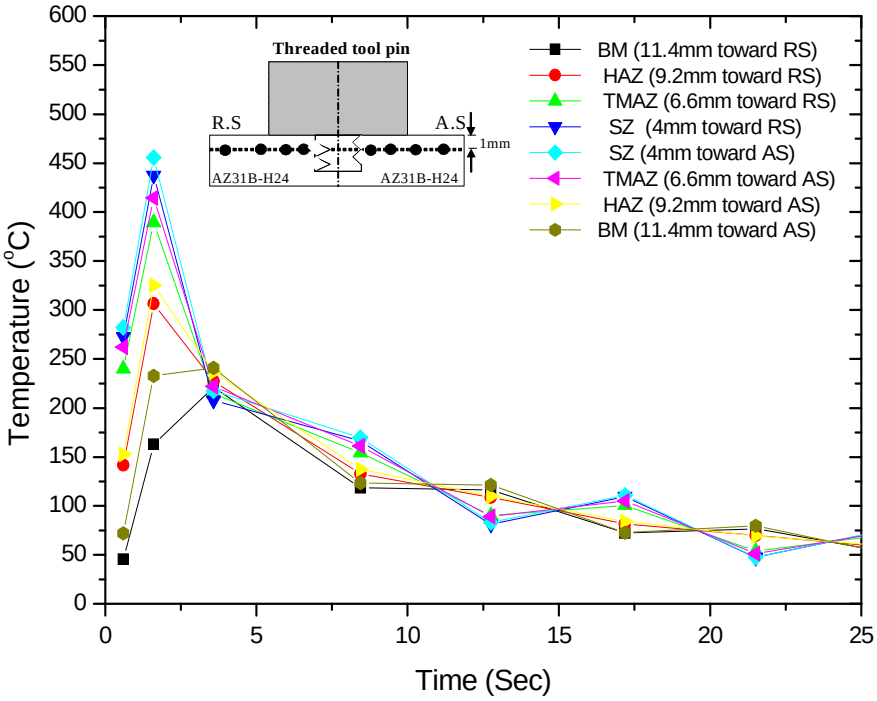

Fig. 4.27 Calculated temperature distributions according to the time variation according to the Threaded pin (AZ31B-H24)

4.4 Welding Residual stress Analysis

4.4.1 Welding Residual stress of Al6061-T6 alloy

The residual stresses are formed in the weld during welding as the expansion of material occurs during the heating of the welded plates, followed by the contraction during the cooling of the welds. Furthermore, the rotational and the transverse movements of the tool will cause additional stress in the weld due to the mechanical constraint of the plates by the fixture. The thermal distribution history from analyzing the conduction of heat is used as input data and the mechanical phenomenon about the result of the analyzing Al 6061-T6 alloys by the thermal-elastic-plastic program is investigated[46]. Fig. 4.28 illustrates the stress (σ_x) in the longitudinal direction and shows that the stress distributes intensively in the SZ, TMAZ and HAZ of welded joint. The maximum tensile stress has been incorporated by pin friction at the central area of the specimen (X= -3, 3mm), the compression stress occurred apart from the welded area. The Fig. 4.29 illustrate the stress (σ_y) perpendicular to the longitudinal axes and the stress (σ_z) along the thickness direction of the specimen and these stresses are tensile around the pin and are compressive apart from the welded area. The residual stresses have a differential value around pin. The component of residual stress in weld line direction is bigger than that in width direction. The magnitude of residual stress is $\sigma_x > \sigma_y > \sigma_z$.

The mechanical property of the Al6061-T6 alloy used for the residual stress analysis is shown in Table 4.18.

Table 4.18 Mechanical properties of Al6061-T6 alloy

Temperature (K)	311	339	366	394	422	450	477	533	589	644
Yield Stress (MPa)	241	238	232	223	189	138	92	34	19	12

4.4.1.1 Residual Stresses of Cylindrical pin

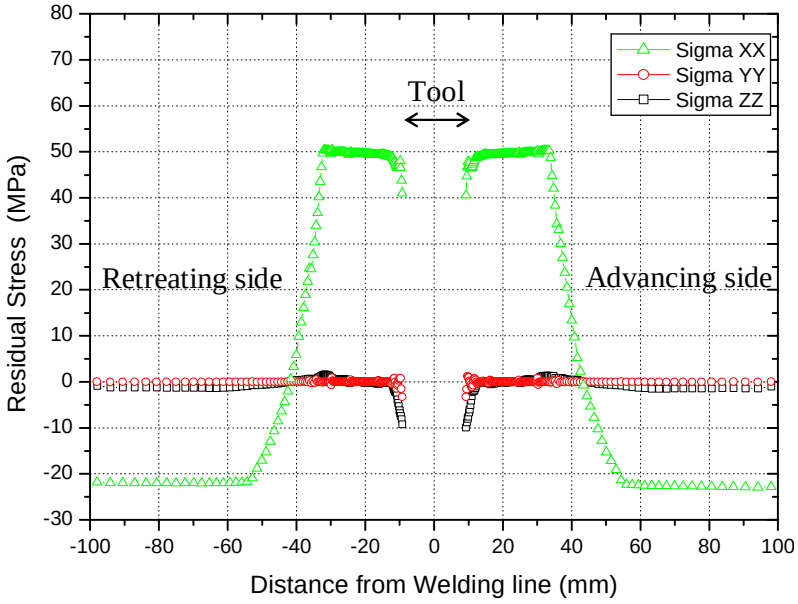

(a) Full scaled graph

Fig. 4.28 Residual stress distributions of Cylindrical pin and magnified

Fig. 4.28 illustrates the stress in the longitudinal direction, perpendicular to the longitudinal axes and along the thickness direction for frustum pin case. The maximum residual stress is about 49.48MPa in advancing side..

4.4.1.2 Residual Stresses of Frustum pin

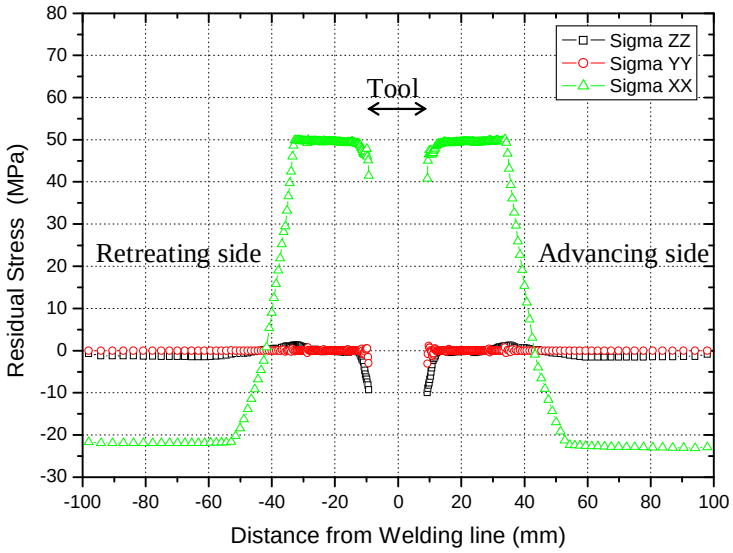

(a) Full scaled graph

Fig. 4.29 Residual stress distributions of Frustum pin

Fig. 4.29 illustrates the stress in the longitudinal direction, perpendicular to the longitudinal axes and along the thickness direction for frustum pin case. The maximum residual stress is about 50.15MPa in advancing side.

.

4.4.1.3 Residual Stresses of Threaded pin

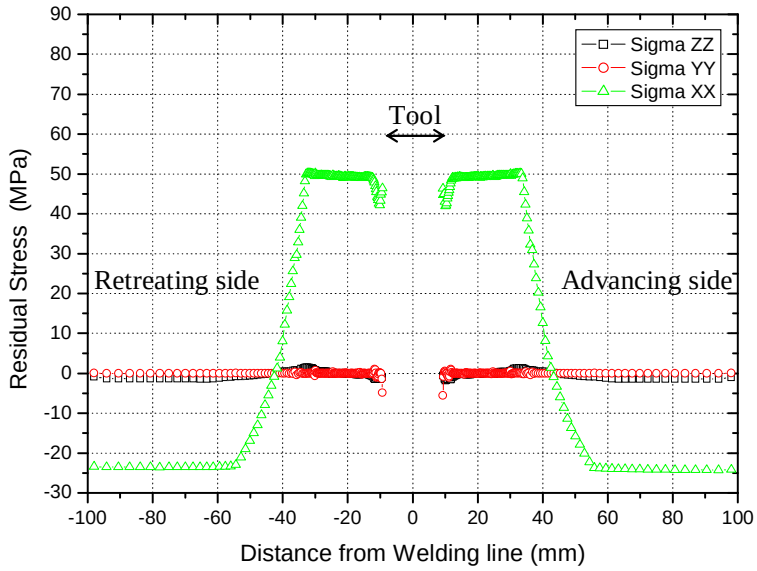

Fig. 4.30 Residual stress distributions of Threaded pin

Fig. 4.30 illustrates the stress in the longitudinal direction, perpendicular to the longitudinal axes and along the thickness direction for threaded pin case. The maximum residual stress is about 49.25MPa.

4.4.1.4. Compared Residual stress, σ_x, distribution along the weld line according to the tool pin shape for (Al6061-T6)

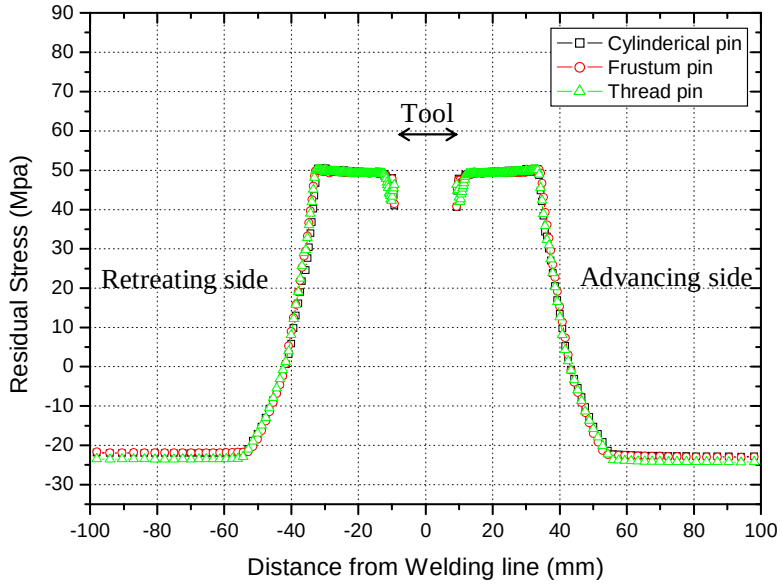

Fig. 4.31 Residual stress, σ_x, distributions in weld line according to the tool pin shape from the crown 1mm and magnified (Al6061-T6)

Using the thermal distribution history from analyzing the heat conduction has been used as input data and the mechanical phenomenon (Residual stress) has been determined. The maximum value of the residual stress for Al6061-T6 alloys for various pin configurations are obtained as shown in the Table 4.19.

Table 4.19 Calculated maximum Residual stress for different pin shapes in Al6061-T6

(Unit: MPa)

Alloy type		Max Residual stress for different Pin configuration		
		Cylindrical pin	Frustum pin	Threaded pin
Al6061 -T6	Advancing side	49.48	50.15	49.25
	Retreating side	49.40	49.49	49.29

4.4.2 Welding Residual stress of AZ31B-H24 Mg alloy

4.4.2.1 Residual Stresses of Cylindrical pin

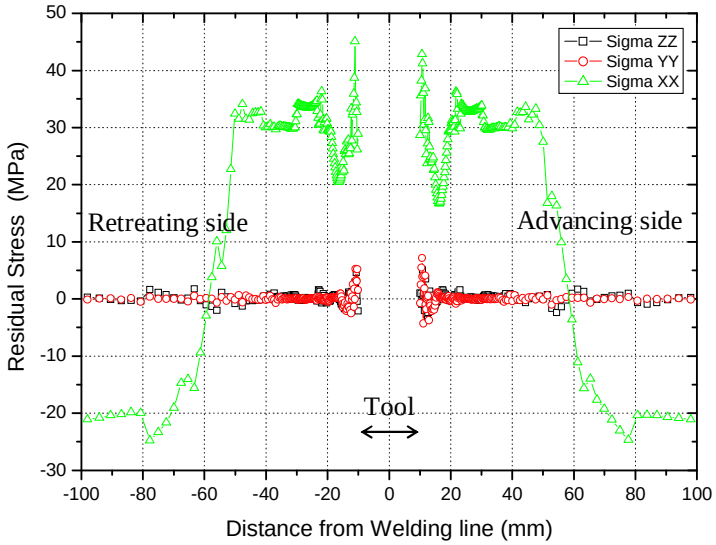

(a) Full scaled graph

Fig. 4.32 illustrates the stress in the longitudinal direction, perpendicular to the longitudinal axes and along the thickness direction for cylindrical pin case. The maximum residual stress is about 45.09MPa.

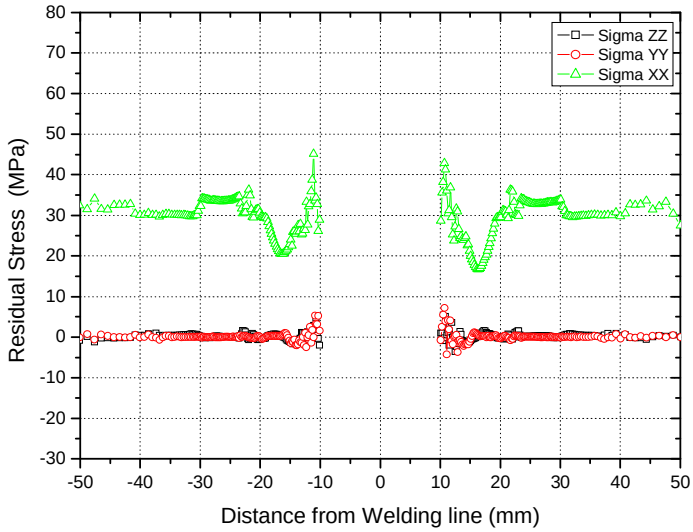

(b) Magnified graph

Fig. 4.32 Residual stress distributions of Cylindrical pin and magnified

4.4.2.2 Residual Stresses of Frustum pin

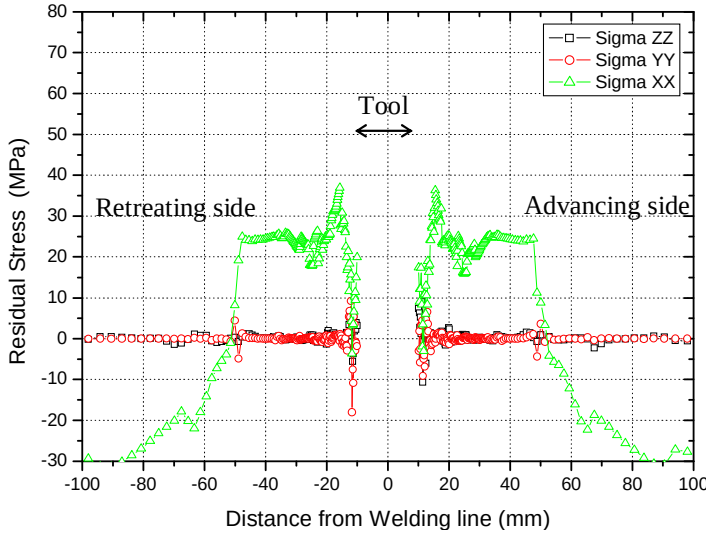

(a) Full scaled graph

Fig. 4.33 illustrates the stress in the longitudinal direction, perpendicular to the longitudinal axes and along the thickness direction for frustum pin case. The maximum residual stress is about 49.48MPa in advancing side.

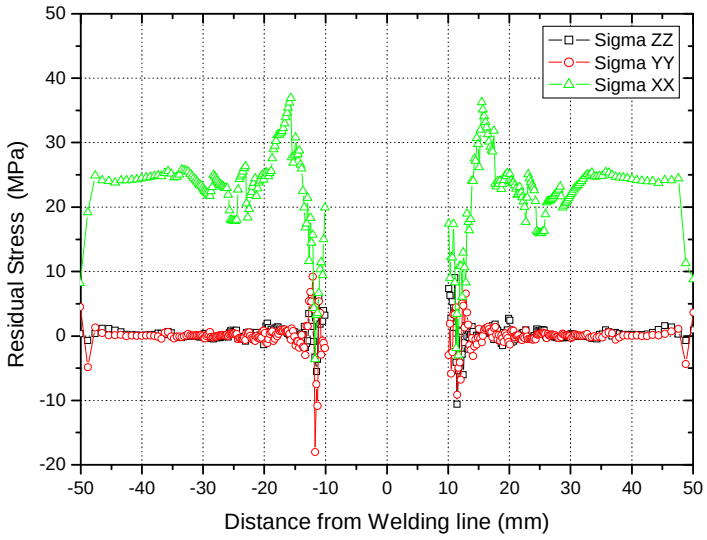

(b) Magnified graph

Fig. 4.33 Residual stress distributions of Frustum pin and magnified

4.4.2.3 Residual Stresses of Threaded pin

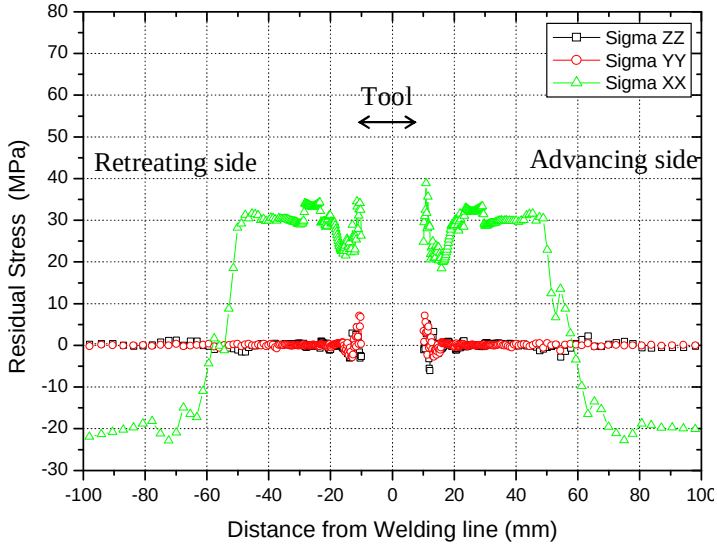

(a) Full scaled graph

Fig. 4.34 illustrates the stress in the longitudinal direction, perpendicular to the longitudinal axes and along the thickness direction for frustum pin case. The maximum residual stress is about 38.89 MPa.

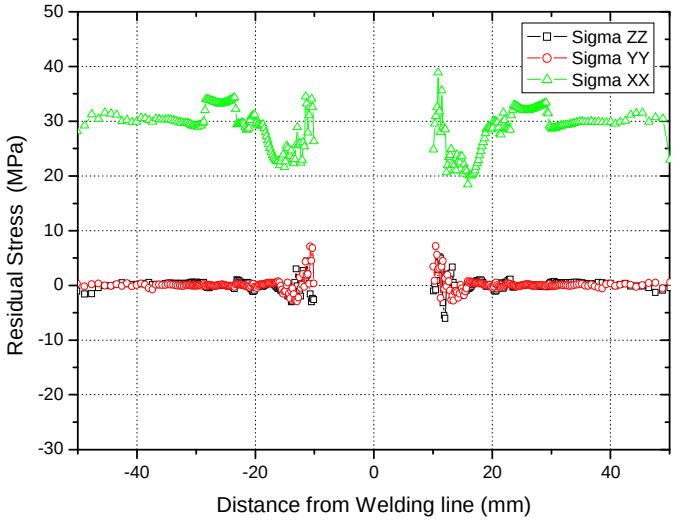

(b) Magnified graph

Fig. 4.34 Residual stress distributions of Threaded pin and magnified

4.4.2.4 Compared Residual stress, σ_x, distribution in weld line according to the tool pin shape (AZ31B-H24)

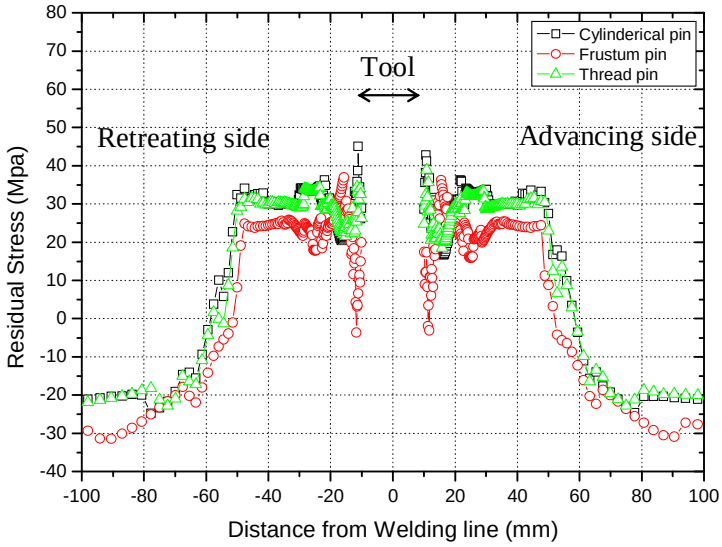

(a) Full scaled graph

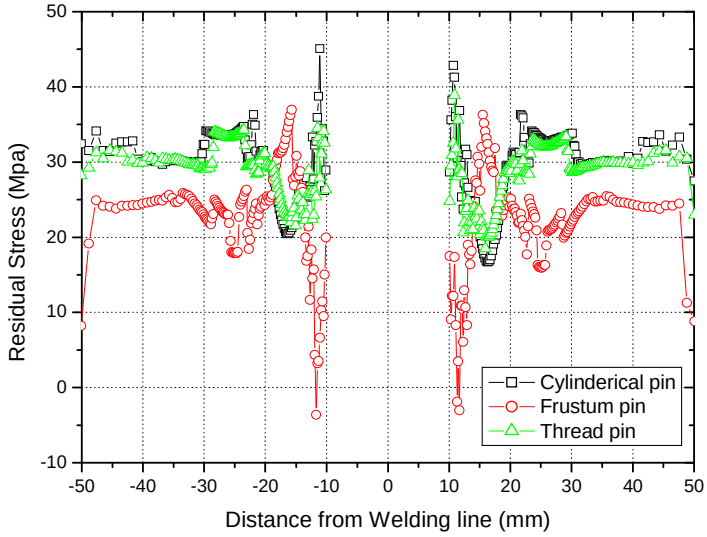

(b) Magnified graph

Fig. 4.35 Residual stress, σ_x, distribution in weld line according to the tool pin shape from the crown 1mm and magnified (AZ31B-H24)

Using the thermal distribution history from analyzing the heat conduction has been used as input data and the mechanical phenomenon (Residual stress) has been determined. The maximum value of the residual stress for MgAZ31B-H24 alloys for various pin configurations are obtained as shown in the Table 4.20.

Table 4.20 Calculated maximum Residual stress for different pin shapes in AZ31B-H24 alloy

(Unit: MPa)

Alloy type		Max Residual stress for different Pin configuration		
		Cylindrical pin	Frustum pin	Threaded pin
AZ31B -H24	Advancing side	45.09	49.48	34.51
	Retreating side	42.84	49.00	38.89

4.5 Discussion on Numerical Analysis results

The numerical simulation of the temperature and residual stress distribution in similar and dissimilar welded Al6061-T6 and AZ31B-H24 Alloys using finite element heat source model developed on the basis of experiment results and characteristics of temperature and residual stress distribution in dissimilar welds are understood from the simulation result. The maximum temperature was formed at the base metal surface contacting with tool shoulder of advancing side, which indicates the frictional heat generated between tool shoulder and base metal surface was the most significant heat source in the process. The welding formed at about 440~480℃ with the aid of plastic flow for the various pin shapes, that is lower than melting temperature (660℃) of aluminum alloy. In the case of the Al6061-T6 and MgAZ31B-H24 alloys maximum temperature in the advancing and retreating side for various pin configurations are obtained as shown in the Table 4.21.

Table 4.21 Calculated maximum temperature values for different pin shapes

(unit: ℃)

Alloy type		Max Temp. for different Pin configuration		
		Cylindrical pin	Frustum pin	Threaded pin
Al6061 -T6	Advancing side	442.76	448.47	441.02
	Retreating side	414.27	398.92	417.50
AZ31B -H24	Advancing side	478.43	474.27	463.56
	Retreating side	440.00	442.57	440.92

Using the thermal distribution history from analyzing the heat conduction has been used as input data and the mechanical phenomenon (Residual stress) has been determined. The maximum value of the residual stress for Al6061-T6 and MgAZ31B-H24 alloys for various pin configurations are obtained as shown in the Table 4.22.

Table 4.22 Calculated maximum Residual stress for different pin shapes

(Unit: MPa)

Alloy type		Max Residual stress for different Pin configuration		
		Cylindrical pin	Frustum pin	Threaded pin
Al6061 -T6	Advancing side	49.48	50.15	49.25
	Retreating side	49.40	49.49	49.29
AZ31B -H24	Advancing side	45.09	49.48	34.51
	Retreating side	42.84	49.00	38.89

Chapter 5

Measurement of Temperature distributions and Residual stresses

5.1 Measurement of Temperature history

As the temperature distribution in the weld zone influence the microstructure and resultant mechanical characteristics of the welds, it is important to obtain the information about the temperature distribution in the weldment of the FSW. In this study transient temperatures were recorded at six locations during the FSW process using *K* type thermocouples. The layout of the locations of the thermocouples is shown in Fig. 5.1. Three rows of the thermocouples are placed 2mm from the top surface and roughly in the center of the plate along the welding direction. Each row has three thermocouples located at 5 mm, 9 mm and 18 mm from the centerline of the weld. First thermocouple corresponds to the measure of temperature in the Stir zone, the second for measuring the temperature in the HAZ and the third for base metal temperature measuring. Holes were pre-drilled from the side surface of the plate. The thermocouples were beaded at the tip and embedded at the measuring points. The transient temperatures from the thermocouples were recorded using Labview software on a PC at 100 HZ.

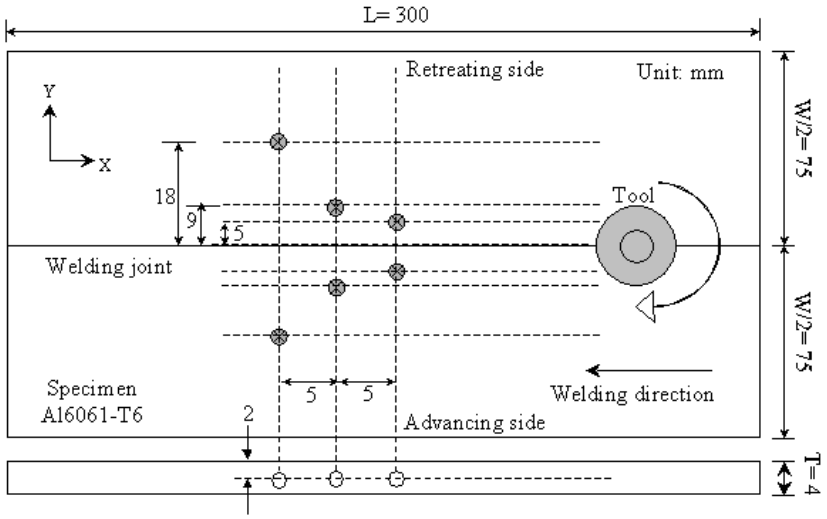

Fig. 5.1 Workpiece dimensions and location of Thermocouples

The K Type thermocouples were used in all experiments on plates. Six thermocouples were positioned perpendicular to the welding direction. The first gauge was positioned as close to stir zone as possible at a distance of 5 mm from the center of the weld. The rest of the thermocouples were positioned at 9 and 18 mm from the center of the weld. A PC based data acquisition system was used for sampling of the T/C signals, and the measurements were presented on-line on the PC

monitor and measurement data was written to disk. The complete measurement system (including T/C wire) was calibrated over the whole measurement range. The T/C used in the test had a wire diameter of 1 mm and surrounded by ceramic cement and Inconel protection for lead out.

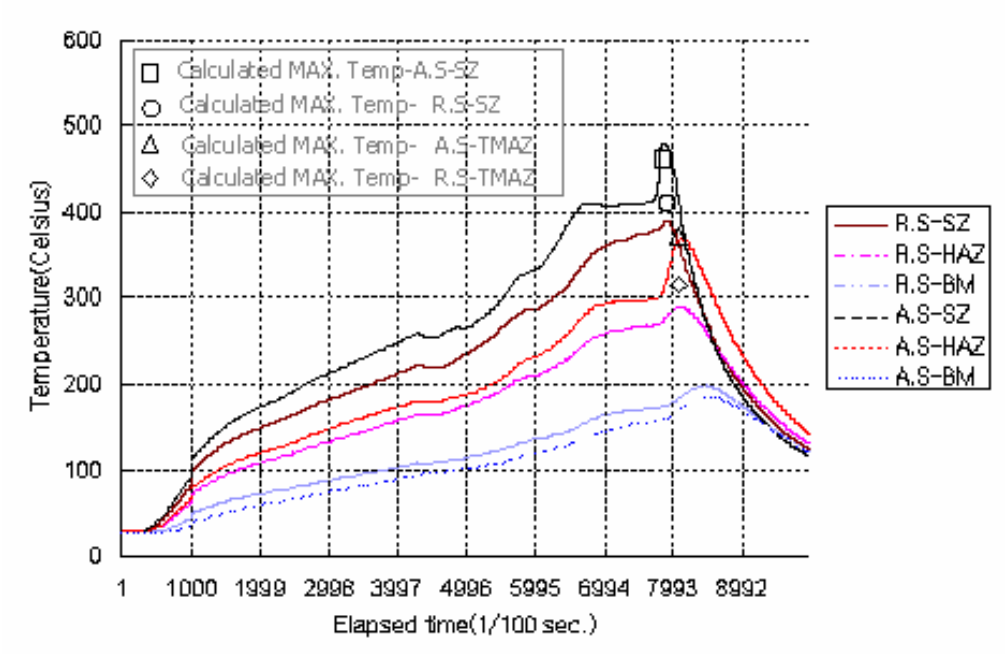

Fig. 5.2 Measured and Calculated temperature distribution of FSWelded joints

Al6061 -T6 alloy

Figure 5.2 shows the measured and calculated temperature history in Al6061-T6 friction stir welded joints. In detail understanding of mechanical characteristics, hardness distribution of weldment should be known along each section. The maximum temperature at Stir zone measured was about 470℃, in the AS of 5mm from weld line and maximum temperature in the RS is about 380℃, which is lower than Mg alloy. The temperature history of the dissimilar welding of Al6061(RS) and MgAz31B (AS) was measured using the thermocouple (1Ø, K-Type) inserted into 3mm and 6mm section from center of weldment as shown in Fig. 5.3.

Figure 5.4 is the graph that is showing the characteristic of heat distribution of FSWelded by measurements took between Advancing side (AS) and Retreating side (RS) in dissimilar welding. The maximum temperature of about 310℃ (580K), in AS of 3mm distance from center along Mg alloys and 250℃ (520K) in RS of 3mm distance from center along Al alloys were measured. The results indicate the asymmetry in the temperature distribution along the advancing side and retreating side of the dissimilar FSW joint. The difference in the temperature in the advancing side and the retreating side is due to the difference in the friction force term. In the advancing side, both

the tangential component of the rotational velocity and the travel velocity component are in same direction and in the retreating side both are in opposite direction. Also the results of EPMA and characteristics of hardness test are alike.

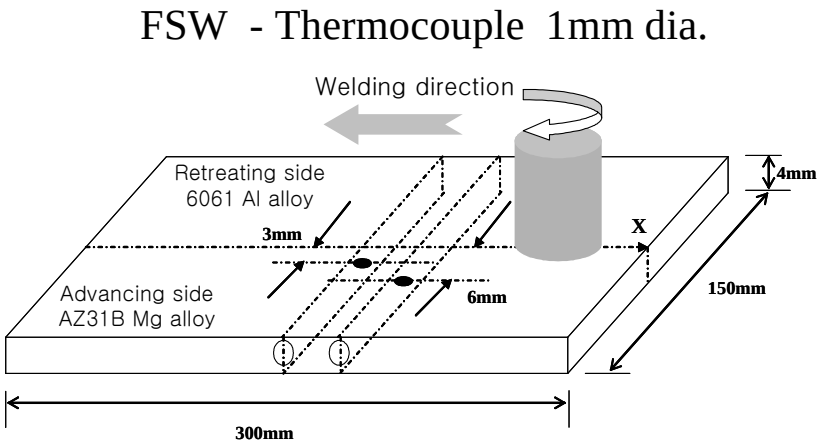

Fig. 5.3 Measurement of temperature of FSWelded joints dissimilar Al6061/AZ31B alloy

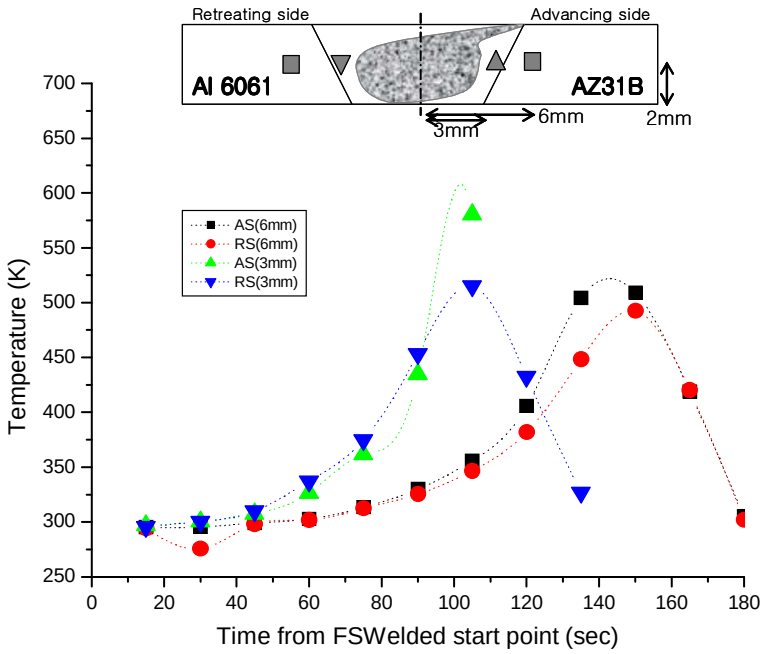

Fig. 5.4 Temperature distribution of FSWelded dissimilar joint of AZ31B/A6061 alloy

5.2 Measurement of Residual stresses

The stress-relaxation technique is employed for measuring the residual stress in friction stir weld. Two-dimensional residual stress of an Al6061-T6 alloy specimen, butt joint welded by the friction stir technique, was performed by the electrical-resistance strain gauges.

As shown in Photo 5.1, the electrical-resistance strain gauges are mounted securely on the surface of welded specimen and that the initial stresses in weldments are measured by TC-31K Data Loger.

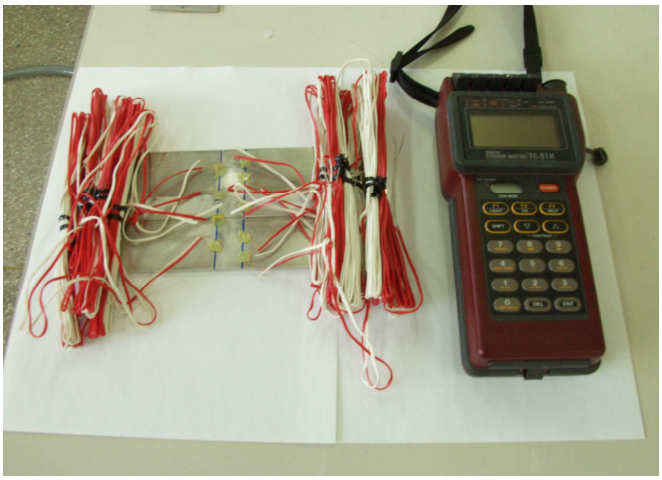

Photo 5.1 Measuring the residual stress in sectioned area with TC-31K

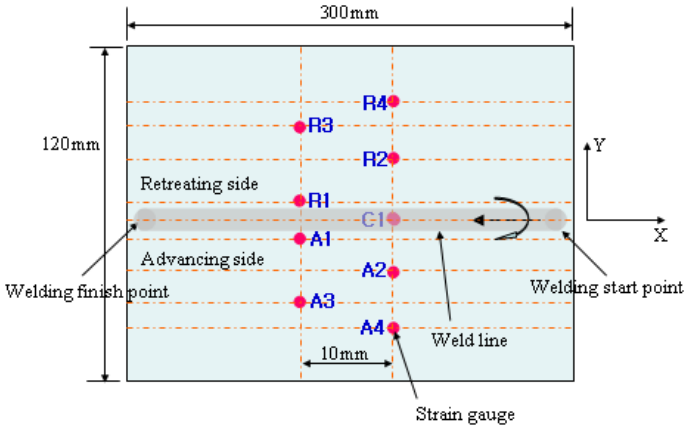

Distance from specimen center line (mm)								
R4	R3	R2	R1	C1	A1	A2	A3	A4
-50	-40	-35	-15	0	15	35	40	50

Fig. 5.5 Schematics of specimen used for the experiment.

The stain gauges are fixed at the location as shown in the Fig 5.5 for determining the residual stress by employing the stress-relaxation technique.

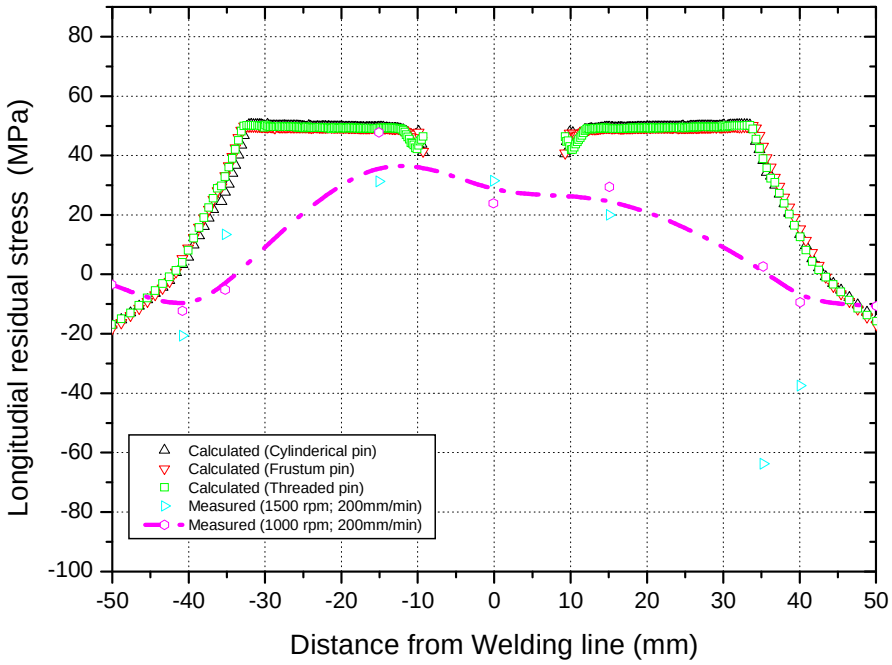

Fig. 5.6 Comparison the residual stress distributions from simulation and experimental results in Al 6061-T6 alloy FSW joint

Figure 5.6 shows a comparative graphical plot of welding residual stresses obtained from experiments and numerical simulations. The residual stresses obtained from experiments are measured on the surface of the FSW joint. Whereas in case of numerical simulation, the stress are calculated along a line 1mm from the crown in the thickness direction and some error are founded in experiment data, but it is found out that the simulation data is reliable to predict the welding residual stress in FSW joints.

Chapter 6

Experiment of Mechanical and Metallurgical Characteristics

6.1 Friction Stir Welding of Al6061-T6, AZ31B-H24 and Al6061/AZ31B alloy

6.1.1 Experiment of Al6061-T6 by FSW

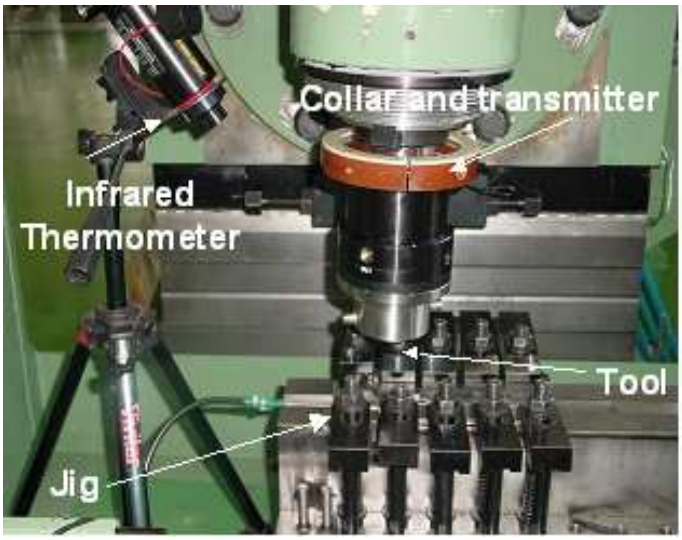

Photo 6. 1 Experimental set-up for FS Welding and details.

Experimental set-up for FS Welding has been arranged as shown in Photo 6.1. Details on the positioning of Tool and Jig are given in Photo 6.1.The specimen used for this study was the Al6061-T6 alloy with 300 mm in length, 200 mm in width and 4 mm in thickness. Its chemical composition is shown in Table 6.1. The heat input, rotating speed, traveling speed, tilting angle, tool pin shapes, etc were considered as main process variables in the experiments.

Same specimen size has been used with square butt joining by FS Welding. The surface of specimen was cleaned using wiping with methyl alcohol. Steel backing plate was used during FS Welding. After welding experiments, bead surface condition and cross section of welds were observed.

Table 6.1.Experiment conditions of Al6061-T6 alloy FSW butt joint

Parameters	Conditions
Tool rotation speed	1000~2000rpm
Travel speed	100~500mm/min
Tool angle	3°

The details of the FSW condition are shown Table 6.1. Friction stir welds was carried out, beginning with a low travel speed, to establish the sound welds, and welds were made in the square groove butt joints. The surface appearances of these friction stir welds were judged. The butt joint plates were clamped on a steel backing plates. The principal process parameters were rotational speed of the tool, travel speed and the downward force, etc. Fig. 6.1 shows top and bottom surface of Al6061-T6 alloy FSW butt joint.

(A) Upper surface

(B) Rear surface

Fig. 6.1 Top and bottom surface of Al6061-T6 alloy FSW butt joint.
(1000rpm, 200mm/min)

Fig. 6.2 shows the various combinations of the Travel speed and rotation speed used for the FS welding. The shaded area in the graph shows the good weldability range for the specimen of Al 6061-T6 with 4mm thick ness.

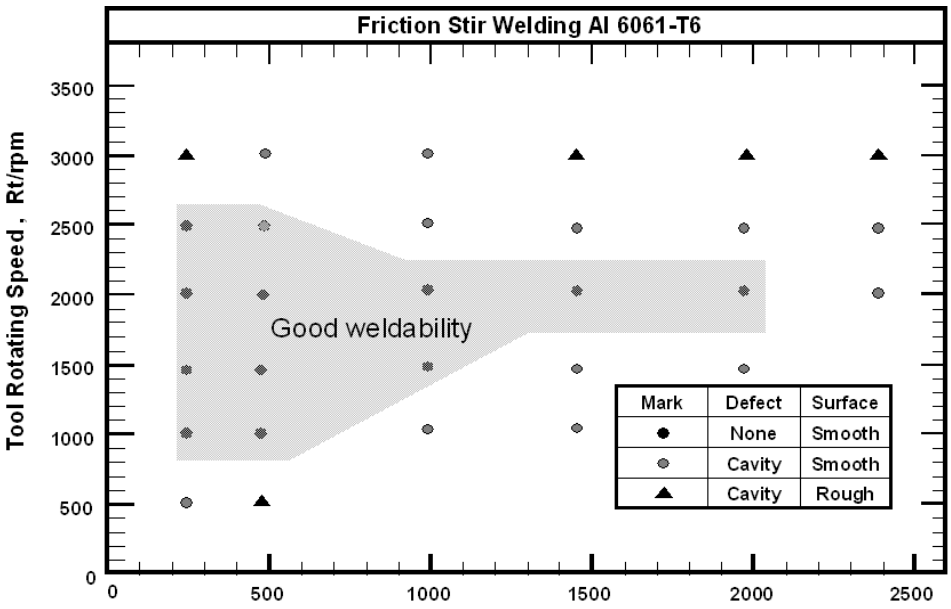

Fig. 6.2 Weldability of Al6061-T6 alloy FSWelded

6.1.2 Experiment of AZ31B-H24 by FSW

The magnesium alloy used for this experiment is a wrought alloy with good strength and ductility. The AZ31B-H24 alloy with the thickness of 4mm, treated for work hardening and partial annealing, is one of the most frequently used Mg alloys[47],[48],[49]. In this experiment, FSW joint was performed under the conditions of the tool RPM, joining speed and advancing angle, described in the Table 6.2.

After the FSW joint, the cross-section of joint has been observed with an optical microscope for section inspection. The hardness distribution at the joint has been tested with a Micro Vickers tester under the condition of 500g weights and 10sec of time. A sub-size standard specimen under the experimental condition of 5 Ton weights has been used to measure yield strength, tensile strength and elongation.

Table 6.2 Experiment conditions of AZ31B-H24 alloy FSW butt joint

Parameters	Conditions
Tool rotation speed	1000~2000rpm
Travel speed	100mm/min
Tool angle	3°

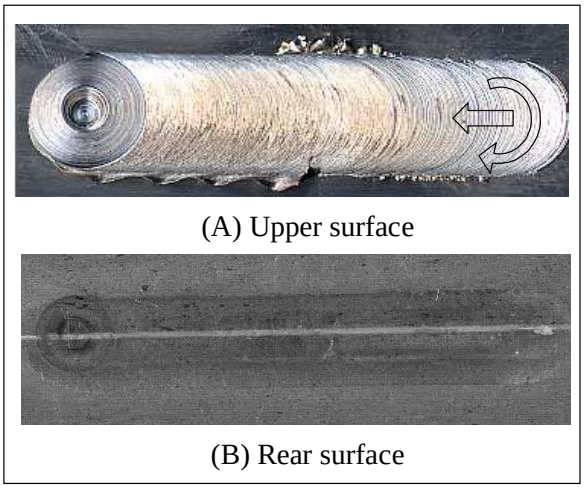

(A) Upper surface

(B) Rear surface

Fig. 6.3 Top and bottom surface of AZ31B-H24 alloy FSW butt joint. (2000rpm, 100mm/min)

Fig. 6.3 shows surface appearance of the top and the bottom surface, joined under the condition of rotation speed of 2000rpm and with a welding speed of 100mm/min. It showed relatively good shapes of joint and no defect on the surface except a few burrs. Very good stirring conditions were observed for this case.

6.1.3 Experiment of Dissimilar Al6061/AZ31B by FSW

In order to demonstrate the friction stir welding of the dissimilar material, AZ31B/Al6061 alloy with the thickness of 4mm, optimum parameters such as tool rotation speed, travel speed, tilt angle, etc. were determined. Fig 6.4 shows a good FSWelded A6061/AZ31B alloy obtained for the rotation speed of 450rpm, travel speed of 15mm/min. It is demonstrated that defects free and a sound bead has been obtained for low rotation speed and travel speed. The experimental conditions are shown in Table 6.3.

The microstructure properties of the heat affected and thermomechanically-affected zones of the FSW joint were studied using optical and scanning electron microscopes. Hardness of the stir zone was remarkably increased due to very fine recrystallized grain structure. The maximum ultimate strength of the joints was equivalent to 40% strength of the base metal. The results indicate that β intermetallic compounds affect tensile properties and fracture locations of the joints[50].

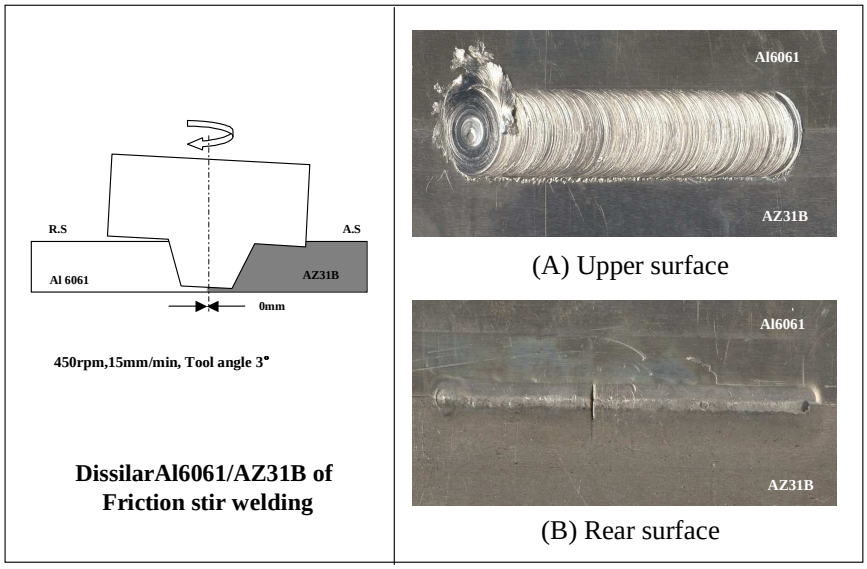

Fig. 6.4 Appearance of dissimilar Al6061/AZ31B alloy FSWelded

Table 6.3 Experiment conditions of dissimilar Al6061/AZ31B alloy FSWeled

Parameter	Conditions
Tool rotating speed	450rpm
Travel speed	15mm/min
Tool tilting angle	2 ~ 3°

The macro surface pictures of similar and dissimilar metals Al6061 and AZ31B alloy are shown in Fig.6.1, Fig.6.3 and Fig.6.4. In the cross section view in SZ zone, it shows an onion ring shape due to the heat by friction and plastic flow. Figure 6.5 shows the good weldabilitiy range of similar (Al6061, AZ31B) and dissimilar (Al6061/AZ31B) FS welding for the various combinations of rotation speed and travel speed. It is obviously observed from the graph that similar material welding can be welded in a wider range than dissimilar material welding. Due to the differences in the properties and crystal structure in dissimilar case, the weldability becomes inappropriate.

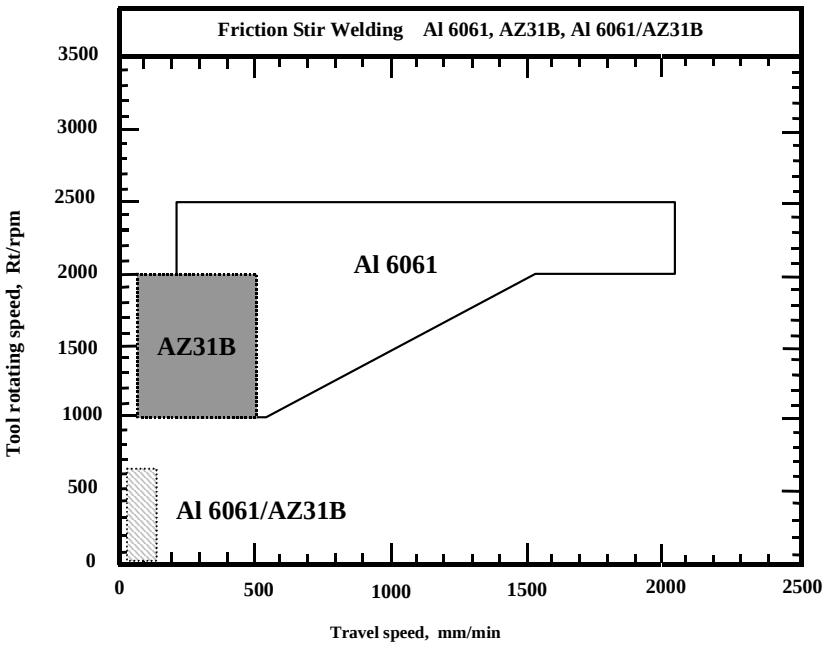

Fig. 6.5 Weldability of A6061, AZ31B and A6061/AZ31B alloy FSWelded

6.2 Hardness Profiles of Friction Stir Welding Joints

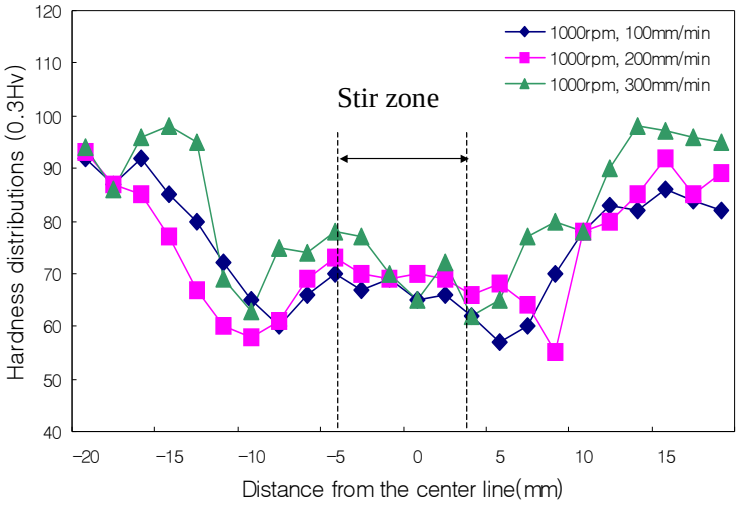

Fig. 6.6 Hardness profiles near weld zone Al6061-T6 FSWelded with various welding speed

Fig. 6.6 shows the relation between cross-sectional hardness profiles near the weld zone with Travel speed of FSW. There were considerable softening region near the weld zone in spite of fine and equiaxed grain structure in the weld zone. The age hardenable 6061Al alloys generally included the strengthening effect by second precipitates such as Mg_2Si.

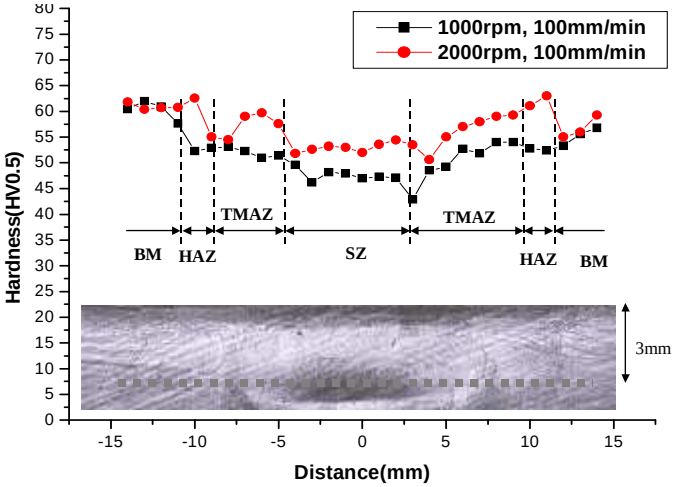

Fig. 6.7 Hardness profiles near weld zone AZ31B-H24 alloy FSWelded with various welding conditions

Fig.6.7 shows the hardness distribution of the joint under conditions of 1,000rpm with 100mm/min and 2,000rpm with 100mm/min. Though both cases indicate similar hardness distribution, a notable feature is the existence of softened SZ. The softening ratio is about 80% of the base metal. It is because the base metal has fine microstructure due to the annealing treatment for inhibition of grain growth, while the microstructure of SZ became coarsened during the processes of recovery, recrystallization and grain growth. Though the microstructure has become larger in TMAZ, it has relatively high hardness as it has many features of work-hardening such as twin deformation and has no recrystallization. Furthermore, applying higher revolutionary speed, higher hardness profiles were obtained, which indicates the work hardening potential increased with increase of rpm. Therefore, the hardness of welded joint was dominantly dependent on the mechanical deformation rather than grain growth.

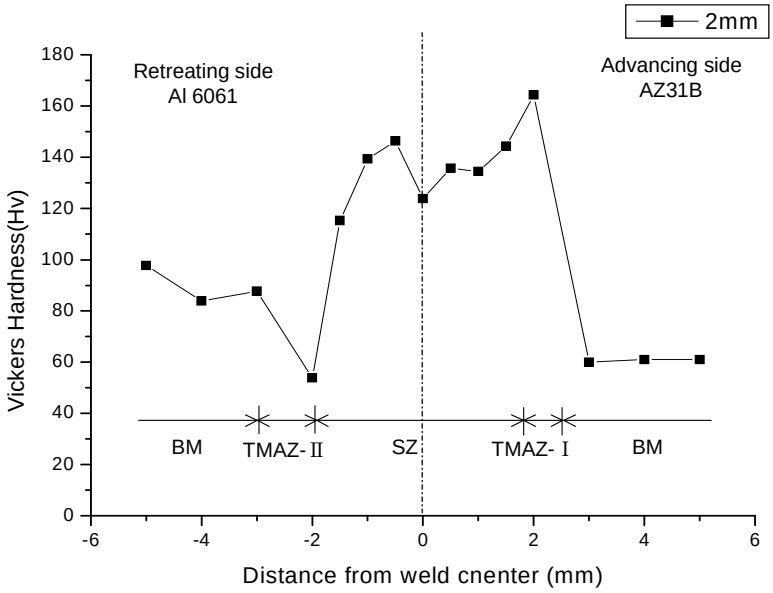

Fig. 6.8 Hardness profiles near weld zone of dissimilar Al6061/AZ31 alloy FSWelded

Fig. 6.8 shows the Hardness profiles near weld zone of dissimilar FSWelded Al6061/AZ31 alloy. From the base metal to TMAZ, SZ zone, the hardness value is increasing and the maximum value is 200Hv is obtained in the TMAZ. So the value of SZ zone is higher than the base metal, because a grain is made and extracted where the fine grain and β-phase intermetallic compounds are created. And the reason that TMAZ of Advancing side (AS zone) shows the highest value of hardness is Al quantity is increased and solid solution hardened by friction of tool in weldment, also the mechanical friction of AS zone is larger than RS zone [51].

6.3 Tensile test of Friction Stir Welding Joints

Fig. 6.9 shows results for tensile test of dissimilar FSWelded and Al/Al alloy, Mg/Mg alloy. The weldment has more tensile strength 40% than base metal. There is little data about mechanical characteristics of FSW. The main problem to be solved is reducing intermetallic compounds, which results in fracture.

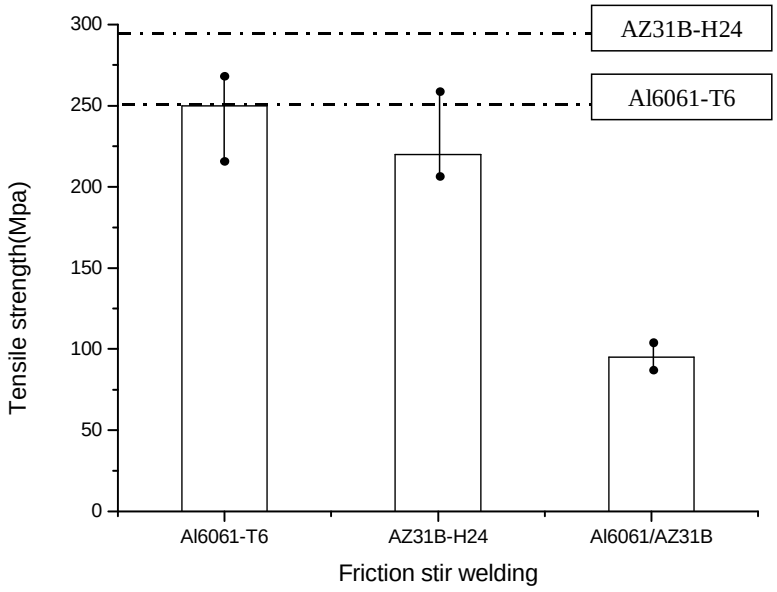

Fig. 6.9 Tensile properties of FSW joints

6.4 Metallurgical Characteristics in Friction Stir Welding Joint

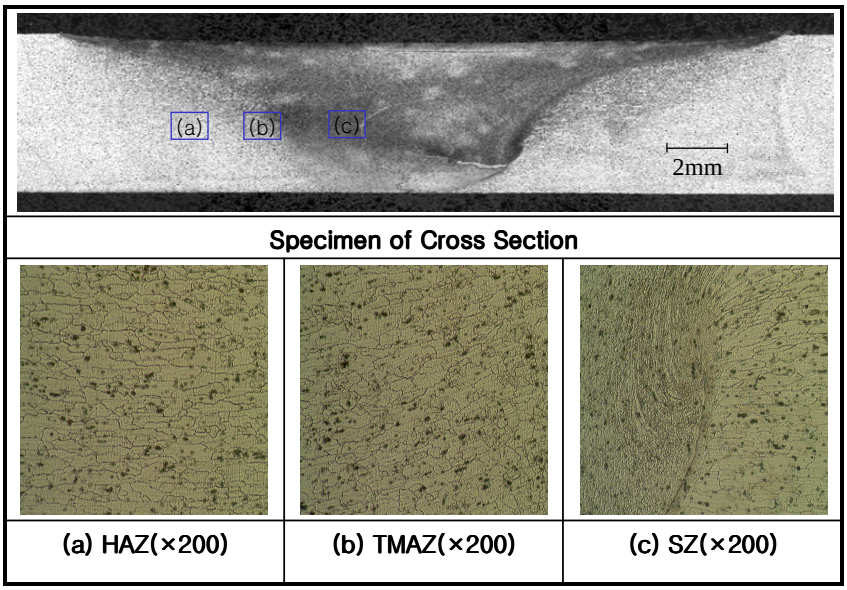

Fig. 6.10 Microstructures of Al6061-T6 alloy FSWelded. (1000rpm -200mm/min)
(A) HAZ, (B) TMAZ, (C) SZ

In general, distinguishable four zones in the transverse section of friction stir welds are: Base Material (BM), Heat Affected Zone (HAZ), Thermo-Mechanically Affected Zone (TMAZ), Stir Zone (SZ). The Stir Zone located in the center of the weld; is subjected to high temperatures and mechanical deformations. The material in this zone is recrystallised. A second zone, next to the nugget, is the TMAZ. The temperatures of the TMAZ are lower than that of the weld nugget, and the mechanical deformation is also less than the extreme case of SZ. The material in this zone shows deformed base material and is not recrystallised. The thermal field only affects the HAZ, and the welding process has not affected the base material in this part of the material. Fig. 6.10 shows the microstructure of FSWelded in Al6061-T6 alloy under the condition of 1,000rpm and 200mm/min, where ‘A’ is BM, ‘B’ is HAZ, ‘C’ is TMAZ and ‘D’ is SZ.

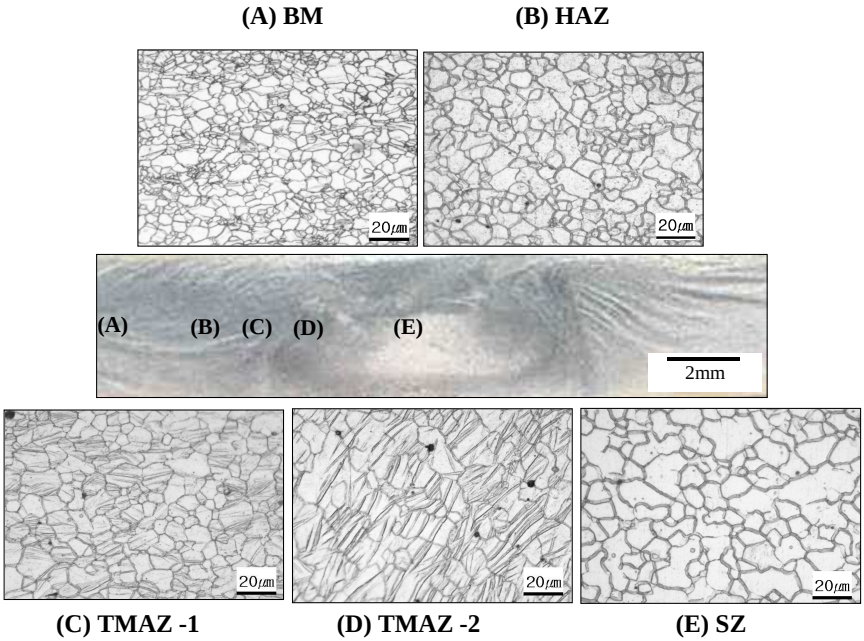

Fig. 6.11 Microstructures of AZ31B-H24 Mg alloy FSWelded. (2000rpm -100mm/min)
(A) BM (B) HAZ (C) TMAZ-1 (D) TMAZ-2 (E) SZ

AZ31B-H24 is a recrystallized alloy of which grain growth is inhibited due to work-hardening after hot rolling process and partial annealing treatment. As shown the Fig.6.11, in A, therefore, the microstructure of base metal has a fine status. B, the HAZ is an area affected by heat only, not by a mechanical element due to the FSW butt joint. It can be observed that the grain size has become larger than that of the base metal while there is no evidence of elongation and no existence of twin deformation due to rolling. In C, the TMAZ, a lot of forms of twin deformation are observed in the microstructure, and this deformation has specific directional property due to mechanical force. The reason, why this kind of mechanical twin deformation is observed mostly in TMAZ, is because the direct plastic deformation occurs due to combined rotational & translational motion of tool. In D the SZ, having processes of recovery, recrystallization and grain growth, a lot of the twin deformation shown in TMAZ appeared as coaxial structures after recovery and recrystallization.

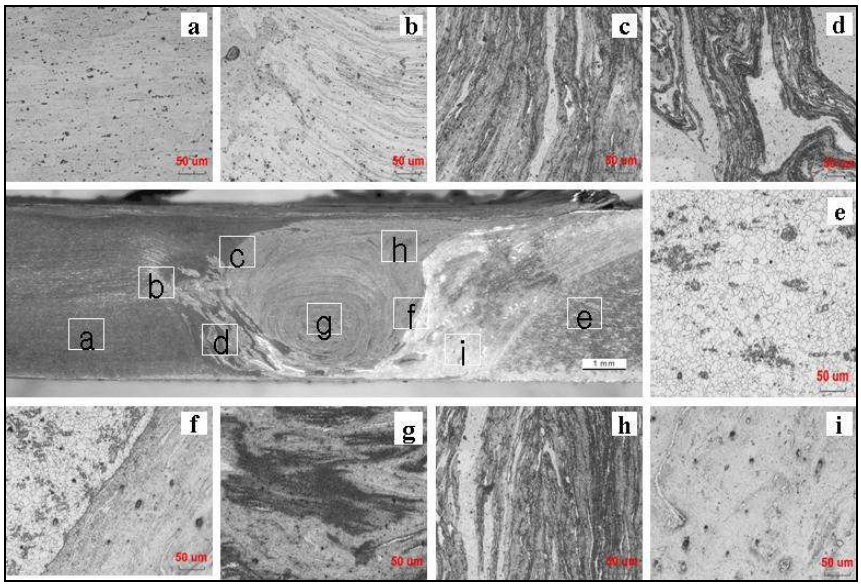

Fig. 6.12 Macro and microstructure feature of dissimilar Al6061/AZ31B alloy FSWeled (450rpm, 15mm/min)

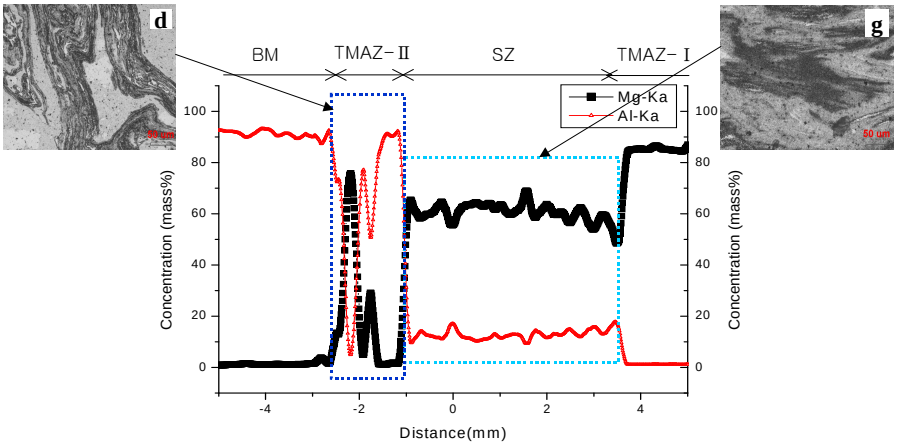

Fig. 6.13 Concentration profiles of Mg and Al atoms across dissimilar Al6061/AZ31B alloy FSWelded

Fig.6.13 is a graph that represents EPMA of SZ. In the SZ zone, fine mixed phases are generated, and in the TMAZ zone, mixed phases of imperfect lamellar structures are also observed, partially. SEM-EPMA is carried out to know how the SZ zone is distributed in the FSW weldment of dissimilar welding. Figure 6.12 show that, Al alloys and Mg alloys are fully mixed and they are generating a new crystal grain. TMAZ-II is shows a lamellar, where the Al alloys and Mg alloys are mixed, because it promoted the plasticization of Mg alloys and stirs the Al alloys and Mg alloys as

the direction of rotation and a direction of movement of the tool are same. On the other hand, in the TMAZ-I zone, direction of rotation is reversed to a direction of movement of the tool, the mixed phase same as TMAZ-II zone cannot be generated because the plasticized Al cannot be made in TMAZ-I. Fig. 6.14 has been shown to understand the distribution of intermetallic compounds using XRD. Intermetallic compounds are found out in SZ zone.

Figure 6.15 is a SEM showing the section of tensile fracture of weldment in dissimilar welding. The brittle and ductile fractures are observed in the section. The EDS analysis reveals, intermetallic compounds (β - $Mg_{17}Al_{12}$2), having brittle characteristic distributed along the fracture section, and it is the main factor of fracture. The conditions for generation of β-phase intermetallic compounds is 310~460℃ and composed 55%Mg-45%Al. It is extracted and hardened along grain boundary and increased the hardness but it is the main factor reducing the toughness and making brittle.

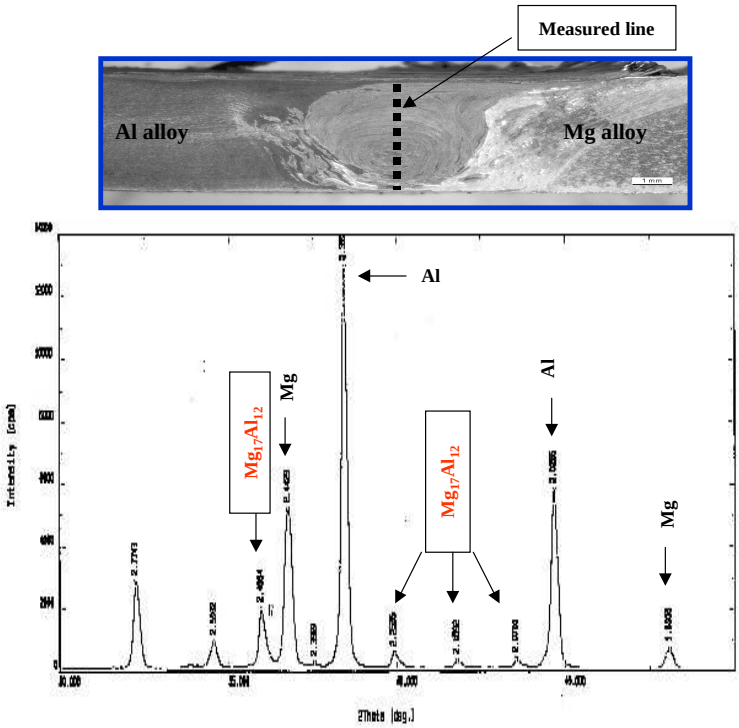

Fig. 6.14 X-ray diffraction pattern of stir zone

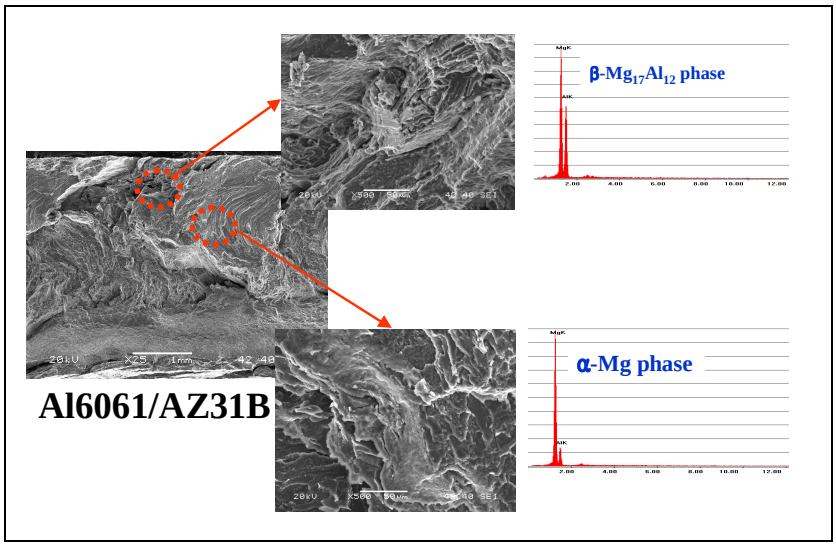

Fig. 6.15 Tensile fracture surface of dissimilar Al6061/AZ31B alloy FSWelded by SEM

6.5 Discussion on Mechanical and Metallurgical Characteristics

The joint of friction stir welded 6061Al alloys showed a good surface quality with less distortion and void. The hardness of weld zone was slightly lower than that of the base metal. This softening could be explained by the dissolution of precipitates and does not depend on the grain size distribution. The tensile strength of friction stir welded 6061 Al alloys nearly approached to the level of base metal. Fracture did not occur at the weld zone but along the HAZ.

The FSW butt joint of Mg/Al alloys on macroscopic observation showed an onion ring in SZ zone having combined Al and Mg alloys with out the presence of the defect. The detail observation showed the presence of extracted intermetallic compounds, β-$Mg_{17}Al_{12}$. Fracture happened in SZ zone and tensile strength is 40 times more than base metal due to intermetallic compound, β-$Mg_{17}Al_{12}$. Reducing the β −phase, sound weldments with high tensile strength could be obtained. In order to reduce this intermetallic compound layer further studies are required. The temperature of Advancing side (AS) zone is higher than Retreating side (RS) zone. Also the hardness values of AS zone are high due to high friction.

Chapter 7

CONCLUSION

In this study, Friction stir welding process was developed for lightweight application using Al-Mg alloys. Fundamental welding phenomena of Friction stir process using FSW machine (RIST WRC) has been investigated by the experiments. In order to calculate temperature and residual stress distribution in friction stir welds, finite element heat source model was developed on the basis of experiment results and characteristics of temperature and residual stress distribution in friction stir welds were understood from the result of simulation. Mechanical and metallurgical characteristics of hybrid welds were also analyzed and compared with other results in order to supply the fundamental information for the criteria of welding design and construction.

For determining the temperature at the interface of the tool shoulder and workpiece during the friction stir welding process, thermal simulation results were used. The active stress in workpiece during the process leads to prediction of residual stress after the workpiece cools down and the clamps are removed. The dominant part of active stress is the thermal stress and its determination is based on the thermal model. The present paper develops a thermomechanical model to predict the thermal history and active stress with adaptive contact conductance at the interface of the workpiece. The stress developed at the interface was determined considering uniform contact conductance and used to define the values and contours of the contact conductance. Comparison of the temperature profile developed using uniform contact conductance with the experimental results showed the possibility of more accurate determination using the present model. The temperature at the probe/matrix interface near the shoulder was found to reach near the solidous temperature.

A two-dimensional thermomechanical model is developed for the FSW of an Al-alloy and Mg-alloy, in order to build qualitative framework to understand the thermomechanical process in FSW. Modeling and measurement of the temperature and stress evolution in the FSW of Al6061-T6 alloy, AZ31B-H24 alloy, and Al6061-T6/AZ31B-H24 alloy are conducted, and the experimental values validate the efficiency of the proposed model.

Numerical modeling and optimization of transient temperature and residual stresses in friction stir welding of Al6061/Al6061, AZ31/AZ31 and Al6061/AZ31 alloy are studied in this thesis. FS welding process is analyzed using nonlinear finite element analysis code in thermal-mechanical scheme where thermal field is analyzed as transient heat conduction and mechanical field as thermal-elasto-plastic. And, Three tool pin cases with optimized tool rotational speeds and travel speeds are considered. From the result, we can summarize the results as follows:

(1) Based on the experimental data of transient temperature history at several specific locations during the FSW for Al6061/Al6061, AZ31/AZ31 and Al6061/AZ31 alloy, an inverse analysis method for thermal simulation is developed. Results show that due to unknown heat energy input from the process, this inverse analysis method is unique and

effective for the calculation of temperature field in the FSW.

(2) For the FS welding cases of Al6061/Al6061, AZ31/AZ31 and Al6061/AZ31 alloy, the numerically determined temperature fields match similar with the experimental data. The maximum temperature during the FSW is at the weld line and within the tool shoulder. The maximum temperature determined from the simulation is between 440 and 500 ◦C, which is significantly less than the melting temperature of Al alloy at 660◦C.

(3) Using the numerically calculated temperature field, the residual stress in the friction stir welded plate is then determined in a subsequent 2-dimensional elastic–plastic mechanical simulation. The numerically calculated residual stresses are consistent with the experimental data.

(4) The residual stress in the welds after fixture release decreases significantly as compared to those before fixture release. Thus the fixture release in the FSW must be considered in the computer simulation for the determination of residual stresses.

The heights temperature (below the melting temperature) for the various pin configurations appears after 2sec.to 2.5 sec., and it rapidly cooled out. It has been noticed that the temperature gradient is equalized after 12 to 25 sec. and the weld part is rapidly cooled through the heat conduction analysis. From the result of this study, Al6061 FSW Calculated Max. Temperature distribution follows; Frustum pin (448.47) > Cylindrical pin (442.76) > Threaded pin (441.02). And, AZ31B-H24 FSW Calculated Max. temperature distribution follows; Frustum pin(474.27) > Cylindrical pin (469.21) > Threaded pin (463.56) (Unit: ℃). The maximum temperature measured using the thermo couple at Stir zone (AS) of Al6061 alloy is about 470℃, in Stir zone (RS) is about 380℃, which is lower than Mg alloy. And, Al6061/AZ31B dissimilar FSW temperature distribution for Cylindrical pin was about 509℃, Frustum pin 467℃, Threaded pin 464℃.

The maximum temperature measured using the thermo couple at Stir zone (AS) of Al6061 alloy is about 470℃, in Stir zone (RS) is about 380℃, which is lower than Mg alloy. The difference in the temperature in the advancing side and the retreating side is due to the difference in the friction force term. In the advancing side, both the tangential component of the rotational velocity and the travel velocity component are in same direction and in the retreating side both are in opposite direction. Also the hardness values of advancing side are higher than that of the retreating side as the friction force is correspondingly high.

Al6061-T6 FSW Calculated Max. Residual stress distribution follows; Frustum pin (50.15) > Cylindrical pin (49.48) > Threaded pin (49.25). And, AZ31B-H24 FSW Calculated Max. Residual stress distribution follows; Frustum pin (49.48) > Cylindrical pin (45.09) > Threaded pin (34.51). (Unit: Mpa).

So from the simulation and experimental results, the Threaded pin case is advantages from the point of view of weld efficiency and process stability. Also maximum temperature and residual values are less compare to other pins.

The difference in the temperature in the advancing side and the retreating side is due to the difference in the friction force term. In the advancing side, both the tangential component of the rotational velocity and the travel velocity component are in same direction and in the retreating side both are in opposite direction. Also the hardness values of advancing side are higher than that of the retreating side as the friction force is correspondingly high.

The joint of friction stir welded Al 6061 alloys showed a good surface quality and no distortion and void. The hardness of weld zone was slightly lower than that of the base metal. This softening could be explained by the dissolution of precipitates. The tensile strength of friction stir welded Al 6061 alloys nearly approached to the level of base metal. The joint of friction stir welded AZ31B-H24 alloys showed a good surface quality under the condition of rotation speed of 2000rpm and welding speed of 100mm/min.

A butt joint of dissimilar Al/ Mg alloys in FSW can be observed an onion ring in SZ zone combined Al and Mg alloys in center of weldment with no defects. The intermetallic compounds, β-$Mg_{17}Al_{12}$ initiate the fracture in SZ zone and tensile strength is 40% more than base metal due to intermetallic compound, β-$Mg_{17}Al_{12}$. By reducing the formation of this β phase, sound weldments with high tensile strength could be developed. So for reducing the formation of this β phase more studies are required.

Reference

[1]. W. M. Thomas, E.D. Nicholas, J.C. Needham, M.G. Murch, P. Temple-Smith, and C. J. Dawes. Friction stir butt welding, 1991. GB Patent 9125978.

[2]. W. M. Thomas, E.D. Nicholas, J.C. Needham, M.G. Murch, P. Temple-Smith, and C. J. Dawes. Improvements relating to friction welding, 1991. European Patent Specification 0 615 480 B1.

[3]. T.J. Lienert, Friction stir welding of DH-36 steel, Proceedings from Materials Solutions 2003 on Joining of Advanced and Specialty Materials 2004; 28–34.

[4]. O.T.Midling, J.S.Kvale and O.Dahl: “Industrialisation of the friction stir welding technology in panels production for the maritime sector”, 1st Int. symp. on FSW, Thousand Oaks, California, USA, 14-16 June 1999.

[5]. T.Kawasaki, T.Makino, S.Todori, H.Takai, M.Ezumi and Y.Ina: “Application of friction stir welding to the manufacturing of the next generation “A-train” type rolling stock”, 2nd Int. symp. on FSW, Gothenburg, Sweden, 26-28 June 2000.

[6]. M.R.Johnsen: “Friction stir welding takes off at Boeing”, Welding Journal February (1999), 35-39.

[7]. C.G.Andersson and R.E.Andrews: “Fabrication of containment canisters for nuclear waste by friction stir welding”, 1st Int. symp. on FSW, Thousand Oaks, California, USA, 14-16 June 1999. 4th International Symposium on Friction Stir Welding, Park City, Utah, USA, 14-16 May 2003

[8]. C.G.Andersson, R.E.Andrews, B.G.I.Dance, M.J.Russell, E.J.Olden and R.M.Sanderson: “A comparison of copper canister fabrication by the electron beam and friction stir process”, 2nd Int. symp. on FSW, Gothenburg, Sweden, 26-28 June 2000.

[9]. W. Tang, X. Guo, J.C. McClure, L.E. Murr, J. Mater. Process. Manufact. Sci. 7 (1998) 163.

[10]. P. A. Colegrove, 3 Dimensional Flow and Thermal Modelling of the Friction Stir Welding Process, 2th International Symposium on Friction Stir Welding, Gothenburg, Sweden, 2000.

[11]. McClure, J. C., Tang, T., Murr, L. E., Guo, X., and Feng, Z., 1998, ‘‘A Thermal Model of Friction Stir Welding,’’ Trends in Welding Research, J. M. Vitek, et al.,

eds., Proceedings of the 5th International Conference, Pine Mountain, GA, June 1–5, pp. 590–595.

[12]. M.W. Mahoney, C.G. Rhodes, J.G. Flintoff, R.A. Spurling, W.H. Bingel, Metall. Mater. Trans. A 29 (1998) 1955.

[13]. P. A. Colegrove, 3 Dimensional Flow and Thermal Modelling of the Friction Stir Welding Process, 2th International Symposium on Friction Stir Welding, Gothenburg, Sweden, 2000.

[14]. Russel, M. J., and Shercliff, H. R., 1999, ‘‘Analytical Modeling of Microstructure Development in Friction Stir Welding,’’ Proceedings of the First International Symposium on Friction Stir Welding, June 14–16, Rockwell Science Center, Thousand Oaks, California

[15]. Ø. Frigaard, Ø. Grong, O. T. Midling, Metall. Mater. Trans. A 32 1189-200, 2001

[16]. Gould, J., and Feng, Z., 1998, ‘‘Heat Flow Model for Friction Stir Welding of Aluminum Alloys,’’ Journal of Materials Processing & Manufacturing Science, 7~21, pp. 185–194.

[17]. Chao, Y. J., and Qi, X., 1998, ‘‘Thermal and Thermo-Mechanical Modeling of Friction Stir Welding of Aluminum Alloy 6061-T6,’’ Journal of Materials Processing & Manufacturing Science, 7, pp. 215–233.

[18]. Chao, Y. J., and Qi, X., 1999, ‘‘Heat Transfer and Thermo-Mechanical Analysis of Friction Stir Joining of AA6061-T6 Plates,’’ Proceedings of the First International Symposium on Friction Stir Welding, June 14–16, Rockwell Science Center, Thousand Oaks, California.

[19]. Y. J. Chao, X. Qi, Heat Transfer and Thermo-Mechanical Analysis of Friction Stir Joining of AA6061- T6 Plates, 1st International Symposium on Friction Stir Welding, Thousand Oaks, California, 14-16 June, 1999.

[20]. J. Xu, S. P. Vaze, R. J. Ritter, K. J. Colligan, J. R. Pickens, Experimental and numerical study of thermal process in friction stir welding, Joining of Advanced and Specialty Materials VI - Proceedings from Materials Solutions 2003 on Joining of Advanced and Specialty Materials, Pittsburgh, PA, United States, Oct 2003.

[21]. Chao, Y. J., and Qi, X., 1998, ‘‘Thermal and Thermo-Mechanical Modeling of Friction Stir Welding of Aluminum Alloy 6061-T6,’’ Journal of Materials

Processing & Manufacturing Science, 7, pp. 215–233

[22]. Gould, J., and Feng, Z., 1998, ‘‘Heat Flow Model for Friction Stir Welding of Aluminum Alloys,’’ Journal of Materials Processing & Manufacturing Science, 7~21, pp. 185–194.

[23]. J. Xu, S. P. Vaze, R. J. Ritter, K. J. Colligan, J. R. Pickens, Experimental and numerical study of thermal process in friction stir welding, Joining of Advanced and Specialty Materials VI - Proceedings from Materials Solutions 2003 on Joining of Advanced and Specialty Materials, Pittsburgh, PA, United States, Oct 2003.

[24]. X. K. Zhu, Y. J. Chao, Numerical simulation of transient temperature and residual stresses in friction stir welding of 304L stainless steel, Journal of Materials Processing Technology, v 146, n 2, p 263-272, Feb, 2004.

[25]. Ø. Frigaard, Ø. Grong, O. T. Midling, Metall. Mater. Trans. A 32 1189-200, 2001

[26]. Chao, Y. J.,and Qi, X., 1999, ‘‘Heat Transfer and Thermo-Mechanical Analysis of Friction Stir Joining of AA6061-T6 Plates,’’ Proceedings of the First International Symposium on Friction Stir Welding, June 14–16, Rockwell Science Center, Thousand Oaks, California.

[27]. C. Chen, R. Kovacevic, Thermomechanical modelling and force analysis of friction stir welding by the finite element method, Proceedings of the Institution of Mechanical Engineers, Part C: Journal of Mechanical Engineering Science, v 218, n 5, p 509-520, May, 2004.

[28]. M. Song, R. Kovacevic, Heat transfer modelling for both workpiece and tool in the friction stir welding process: A coupled model, Proceedings of the Institution of Mechanical Engineers, Part B: Journal of Engineering Manufacture, v 218, n 1, p 17-33, 2004.

[29]. Song, M., and Kovacevic, R., 2002, ‘‘A New Heat Transfer Model for Friction Stir Welding,’’ Transactions of North America Manufacturing and Research Institute, Society of Manufacturing Engineering, Vol. XXX, pp. 565–572

[30]. D. Lawrjaniec, A. Abisror, C. Decker, M. Kocak, J. Dos Santos, Numerical simulation of friction stir welding, Materials Science Forum, v 426-432, n 4, p 2993-2998, 2003.

[31]. Z. Khandkar, J. A. Khan, P. A. Reynolds, A thermal model of the friction stir

welding process, American Society of Mechanical Engineers, Heat Transfer Division, v 372, n 5, p 115-124, 2002.

[32]. L. Fourment, S. Guerdoux, M. Miles, T. Nelson, Numerical Simulation of friction stir welding process using both Lagrangian and Arbitrary Lagrangian Eulerian Formulations, 5th International Friction Stir Welding Symposium (5IFSWS) Metz, France, 14-16 September, 2004.

[33]. H. Schmidt, J. Hattel, Modelling thermomechanical conditions at the tool/matrix interface in friction stir welding, 5th International Friction Stir Welding Symposium (5IFSWS) Metz, France, 14-16 September, 2004.

[34]. Ch. Desrayaud, P. Heurtier, D. Alléhaux, F. Montheillet, Thermomechanical and microstructural modelling of the friction stir welding processs, 5th International Friction Stir Welding Symposium (5IFSWS) Metz, France, 14-16 September, 2004. 38

[35]. K. Colligan, Weld. J. 78 (1999) 229S–237S.

[36]. Y.J. Chao, X. Qi, J. Mater. Process. Manufact. 7 (1998) 215.

[37]. M.Z.H. Khandkar, J.A. Khan, J. Mater. Process. Manufact. 10 (2001) 91.

[38]. W.J. Arbegast, P.J. Hartley, in: Proceedings of the Fifth International Conference on Trends in Welding Research, Pine Mountain, GA, USA, June 1–5, 1998, p. 541.

[39]. O. Frigaard, O. Grong and O. T. Midling: Proceeding of INALCO98, (1998), 197

[40]. Thermal stress, creep and heat conduction analysis by finite element method, Science, pp.1~99, pp.115~120, pp.135~158, 1985. (in Japanese)

[41]. KOICHI MASUBUCHI, Analysis of Welded Structure, PERGAMON PRESS, pp.1~234, 1980

[42]. Yukio UEDA and Taketo YAMAKAWA. “Analysis of Thermal Elastic-Plastic Stress and Strain during Welding by Finite Element Method.” Transaction of the Japan Welding Society Vol. 2, No. 2, pp.90~100, September 1971.

[43]. H.S. Bang. “Study on The Mechanical Behaviour of Welded part in thick Plate - Three-dimensional Thermal Elasto-Plastic Analysis Base on Finite Element Method.” Journal of the Korean Welding Society, Vol.10, No.4, pp.37~43, December 1992.

[44]. D. R. J. OWEN and E. HINTON, FINITE ELEMENTS IN PLASTICITY: Theory and Practice, Pineridge Press Limited, pp.13~31, pp.215~269, 1980

[45]. JOHN GOLDAK, ADITYA CHAKRAVARTI, and MALCOLM BIBBY. “A New Finite Element Model for Welding Heat Sources.” METALLURGICAL TRANSACTION B, VOLUME 15B, pp.299~305, JUNE 1984.

[46]. Y. Ueda, Y. C. Kim, K. Garatani, T. Yamakita and H. S. Bang: Mechanical Characteristics of Repair Welds in Thick Plate (Report I) – Distribution of Three-dimensional Welding Residual Stresses and Plastic Strains and Their Production Mechanisms -, Trans, of JWRI, Vol.15, No.2, 1987.

[47]. Hwa-Soon Park, Woo-Yeol Kim, Chung - Yun Kang: Welding and Bonding of Dissmilar Metal Steel/Nonferrous Metal, Journal of KWS, 14-6 (1996), 1-7 (in Korean)

[48]. Soon Chan Park, Kwang Seon Shin : Mg Alloys for Weight Reduction of Automobiles, Bulletin of the Korean Inst. of Met & Mat., 9-2 (1996), 160~171

[49]. Eun-Soo Park, Jae-Woo Kim, Do-Hyang Kim : Recent Development of High Strength, High Toughness Magnesium Alloys, Journal of the Korean Foundrymen's Society, 18-2 (1998),118-123 (in Korean)

[50]. A. Munitz: Mechanical properties and microstructure of gas tungsten arc welded magnesium AZ91D plates, Materials Science and Engineering : A302 (2001), P71

[51]. T. Kitahara, K.Katoh and H.Tokisue: PREPRINT OF THE NATIONAL MEETING OF JWS,68(2001),132~134

ACKNOWLEDGEMENTS

I would like to express my sincere gratitude to Prof. Han-Sur Bang for having provided me an opportunity to work under him. I thank him for his valuable guidance and suggestions during the course of this work..

I would also like to thanks my other committee members, Dr. Young-Gak Kweon and Dr. Woong-Seong Chang for being in my committee.

This gives me a great opportunity to express my gratitude, to my parents Mr. Chul-Ho Kim and Mrs. Young-Hui Park for being a constant source of strength and support. Special thanks go to my wife Soo -Yeon Lim and my son Chan Kim.

I would like to extend my appreciation to Ph.D student Rajesh.S.R for his help that he has provided me. Also thanks to all my co-workers and friends for their help and support.